Study of Combined Function Superconducting Accelerator Magnets Containing Higher Harmonics

Tetsuhiro Obana

DOCTOR OF PHILOSOPHY

Department of Accelerator Science

School of High Energy Accelerator Science

The Graduate University for Advanced Studies

2005

Abstract

A study of superconducting combined function magnets with higher order harmonics has been performed, aiming at an application for the Fixed Field Alternating Gradient (FFAG) accelerator. The FFAG accelerator magnet is required to have a nonlinear magnetic field that increases with k-th power of the orbit radius, where k is the field index in the accelerator. The required nonlinear magnetic field has been investigated with combined function coils, which consist of a large elliptical aperture, designed by using a computer code that was specifically developed for this purpose. It has been understood from tracking that the integrated magnetic field along the beam path is the important parameter to be optimized. The field quality was evaluated with a particle trajectory simulation in which a particle could circulate well with stable tune. A prototype coil has been successfully developed by using a 6-axis CNC winding machine. The magnetic field and cryogenic characteristics of the prototype have been verified in warm and cold measurements. As a consequence, a superconducting combined function coil design has been made for future application in the FFAG accelerator, and its technical feasibility has been verified with the prototype magnet development and the performance test.

Contents

1 Introduction

1.1 Background and Motivation

The Fixed Field Alternating Gradient (FFAG) accelerator offers the expectation of rapid acceleration of high intensity beams with charged particles. The FFAG accelerator concept was proposed by Ohkawa in 1953 [1]. During a period in the latter half of the 1950s to 1960s, model machines of the FFAG accelerator for electrons were developed for the MURA project [2]. However, the FFAG accelerator had been shelved for a long time since that project was completed because of technical problems such as 3D magnetic design [3]. The technical problems have now been settled thanks to advances in technology. As a result, the Proof of Principle (PoP) FFAG, which is the world's first proton FFAG, was developed at KEK in 1999 [4]. With the success of the PoP FFAG, the FFAG accelerator has recently received much attention for several applications such as high energy physics experiments, electric power and medical facilities [5]. Especially for medical applications, the FFAG could have great potential as a cancer therapy machine because of possibly easier operation and lower construction cost as compared with a synchrotron [6,7].

In order to be widely used, however, compactness of the FFAG is important. The static magnetic field required for the FFAG provides an ideal application for superconducting magnet technology, because problems associated with time varying magnetic field, such as AC loss, can be neglected [8]. The superconducting magnet makes possible high magnetic field, so that the accelerator can reach a higher beam energy for a given accelerator size, or the accelerator can be smaller for a given beam energy. In addition, the superconducting magnet enables electric power consumption in the accelerator to be lower. The performance of the FFAG accelerator is therefore considerably improved by using superconducting magnets [9].

Superconducting magnets are either superferric in which the field is determined by the pole shape, or magnets in which the field is determined by the coil geometry [10]. The field in superferric magnets is limited by saturation effects in the iron. Higher fields are possible in superconducting magnets where the field is given by coil configurations.

As the first step toward development of a high field superconducting FFAG magnet, it is necessary to verify that a suitable field can be generated for the FFAG accelerator by using coil configurations.

1.2 FFAG accelerator magnets

Magnets utilized in the FFAG accelerator are required to generate the nonlinear magnetic field containing higher order harmonics as follows:

$$B(r) = B_0 \left(\frac{r}{r_0} \right)^k \tag{1}$$

Up to now normal conducting magnets have been used in FFAG accelerator such as the PoP FFAG and the 150 MeV FFAG developed at KEK. The normal magnets realize the magnetic field by shaping of the iron poles [3]. It is difficult to generate very high magnetic field with such conventional magnets because of the saturation of iron. High magnetic field can be realized more easily with superconducting magnets. Futhermore, superconducting magnets can be made to generate the nonlinear magnetic field by careful configuration of the coil.

Two types of superconducting FFAG magnet have been proposed. The first type is a multilayer nested coil design which was proposed in NIRS [11], in which each multipole is produced by a dedicated coil. This type of superconducting magnet has some problems in that a large quantity of superconducting wire is needed to make the coils, and it is difficult to support complicated magnetic forces between them. In addition, the operation of the magnet is complex because a different power supply is required for each superconducting coil.

The second type is a single unit coil type, which was adopted in this study, based on the concept of conventional superconducting accelerator magnets. The coil design is performed with $\cos(n\theta)$ current distribution in this type, and support for the magnetic force between coils is relatively straightforward. Additionally, only one power supply per magnet is required, so that the magnet can be operated easily. This type of the superconducting magnet is therefore considered to be an interesting candidate for the FFAG accelerator magnet.

1.3 Combined function superconducting magnets

The FFAG accelerator requires a combined magnetic field of dipole with higher order harmonics in a single magnet which is called a "combined function magnet". We discuss here the magnetic design of superconducting combined function magnets in which the field is dominated with the current distribution in the coil rather than being built up from layers dedicated to distinct multipoles. It is first assumed that line currents are infinitely long and parallel to the direction of the particle trajectory.

In the case that line currents of $I_m \cos(m\theta)$ are arranged on a circle, the normal component of the magnetic field generated by the currents is given by

$$B_n = \sum_q -\frac{\mu_0 I_m \cos(m\theta_q)}{2\pi r_0} \left(\frac{r_0}{a}\right)^n \cos(-n\theta_q) \tag{2}$$

Equation 2 can be rewritten as follows:

$$\begin{pmatrix} B_1 \\ B_2 \\ B_3 \\ \cdot \\ \cdot \\ B_n \end{pmatrix} = \boldsymbol{A} \cdot \begin{pmatrix} I_1 \\ I_2 \\ I_3 \\ \cdot \\ \cdot \\ I_m \end{pmatrix} \tag{3}$$

where

$$\boldsymbol{A} = \begin{pmatrix} a_{11} & a_{12} & a_{13} & \cdot & \cdot & a_{1m} \\ a_{21} & a_{22} & \cdot & \cdot & \cdot & \cdot \\ a_{31} & \cdot & \cdot & \cdot & \cdot & \cdot \\ \cdot & \cdot & \cdot & \cdot & \cdot & \cdot \\ \cdot & \cdot & \cdot & \cdot & \cdot & \cdot \\ a_{n1} & \cdot & \cdot & \cdot & \cdot & a_{nm} \end{pmatrix} \tag{4}$$

and

$$a_{n,m} = \sum_k -\frac{\mu_0 \cos(m\theta_k)}{2\pi r_0} \left(\frac{r_0}{a}\right)^n \cos(-n\theta_k) \tag{5}$$

Equation 3 can be changed into the following equation:

$$\begin{pmatrix} I_1 \\ I_2 \\ I_3 \\ \cdot \\ \cdot \\ I_m \end{pmatrix} = \boldsymbol{A}^{-1} \cdot \begin{pmatrix} B_1 \\ B_2 \\ B_3 \\ \cdot \\ \cdot \\ B_n \end{pmatrix} \tag{6}$$

The current distribution for the normal component of each multipole magnetic field, which is required from the combined magnetic field, can be obtained by using Eq. 6. Consequently, the current distribution for the combined magnetic field can be realized with the following equation

$$I = \sum_m I_m \cos(m\theta) \tag{7}$$

1.4 Objective and Composition

In the FFAG accelerators which have been developed so far, the required magnetic field with higher order harmonics is generated by shaping the iron. When superconducting magnets are used, the magnetic field has to be realized with high accuracy by careful design of the coil configuration. The objective of the study is to explore the feasibility of such a superconducting magnet, which consists of a coil based on the $\cos(n\theta)$ current distribution and generates a magnetic field containing higher order harmonics to be utilized for the FFAG accelerator.

The first aim of the study was to establish the design of a combined function magnetic field based on the conventional concept of superconducting accelerator magnets and yet fulfilling the stringent asymmetric and space constraints involved with the FFAG. This study required the development of a new optimization process. The second aspect of the study was to realize the coil winding technology that can generate the magnetic field required for the FFAG in terms of the production and test of a prototype coil, and to clarify the coil characteristics which are essential to develop the demonstration coil. In addition, the scope of this study includes the design of such a magnet taking the effect of an iron yoke into account.

The composition of the thesis is as follows: Chapter 2 describes the design of a coil configuration for the superconducting FFAG magnet. Chapter 3 and Chapter 4 present the development and the experimental study of the prototype superconducting coil, respectively. Discussion is held in Chapter 5, and Chapter 6 draws a conclusion.

2 Magnetic field design of superconducting coils for FFAG accelerator magnet

2.1 Design parameters

The FFAG accelerator has been proposed as a machine for cancer therapy using a proton beam. The design parameters of the FFAG accelerator are listed in Table 1, and the layout of the FFAG is illustrated in Fig. 1. Focusing magnets and defocusing magnets are placed alternately, and there are spaces between magnets for the installation of equipment such as RF cavities etc. Based on the parameters of the FFAG summarized in Table 1, the design parameters of the focusing and the defocusing magnets were chosen as listed in Table 2. The field index k is defined in Appendix A.

It can be noted in Table 2 that the vertical magnetic field (Dipole) at the mid-plane center is a fairly modest 1 T. This is because the FFAG layout for which the magnet is designed in the present work has been studied for the application of a conventional magnet. This could have been rendered superconducting by simply replacing the normal conducting coil with cryostable superconducting coils and leaving the determination of the field pattern to the geometry of the iron poles of the magnet. Such a design would always be limited by the saturation of the iron yoke. The purpose of this study is to explore the possibility of making a superconducting magnet in which the field is determined by positioning of the conductor, as it is in the case of high field accelerator magnets. Such magnets can produce field far in excess of the saturation limit of iron: the limits are set by the characteristics of the conductor and the containment of magnetic forces. The field required for the FFAG is more complicated than that of a synchrotron, and it was decided that it would be more reasonable at this juncture to investigate the possibility of a version of this type of magnet with a modest central field, yet one which satisfies the constraints of a practical FFAG machine. This is thus the first step of the design of a future compact high field FFAG.

Table 1: Parameters for the FFAG accelerator

Injection energy	~ 40 MeV
Extraction energy	~ 230 MeV
Number of sectors	12
Type of the magnet	Radial sector
Structure	FODO
Major axis of the beam tube	0.8 m
Minor axis of the beam tube	0.6 m
Field index, k	10
F/D	2.3
Beam excursion	0.4 m

Table 2: Design paramenters for the FFAG superconducting focusing and defocusing coils

	Focusing	Defocusing
Major axis of the beam tube	0.8 m	0.8 m
Minor axis of the beam tube	0.6 m	0.6 m
Longitudinal length	1.09 m	0.55 m
Vertical magnetic field at the magnet center	1.0 T	0.43 T
Field index, k	10	10
Distance between the accelerator center and the magnet center	5.0 m	4.9 m

2.2 Realization of FFAG magnetic field

The magnetic field required for the FFAG magnet is given as follows:

$$B\left(x\right)=B_0\left(\frac{R_0+x}{R_0}\right)^k \tag{8}$$

where x is the distance from the center of the FFAG magnet, R_0 is the distance between the accelerator center and the magnet center, B_0 is the reference field at $x=0$, and k is the geometrical field index. The schematic view of the FFAG magnet in the vertical section is illustrated in Fig. 2. The magnetic field given by Eq. 8 is expanded into the multipole field combination

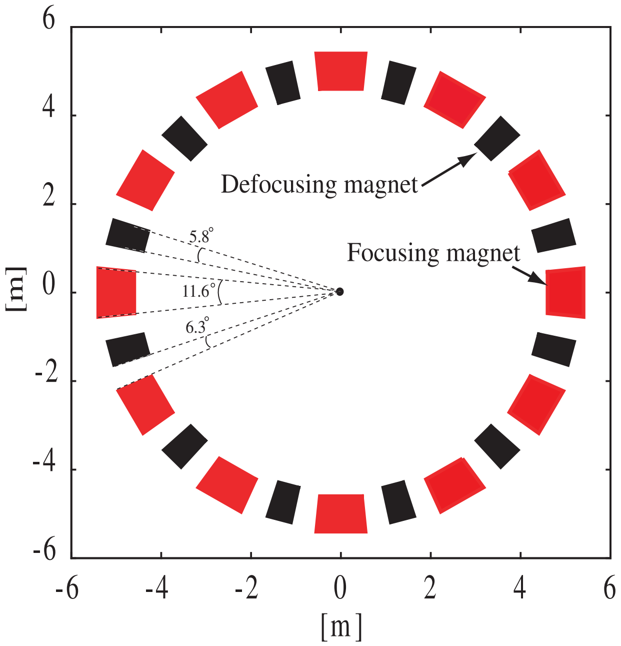

Figure 1: Layout of FFAG accelerator

as follows:

$$B\left(x\right)=B_0\left(1+r_0\frac{k}{R_0}\frac{x}{r_0}+r_0^2\frac{k(k-1)}{2!R_0^2}\left(\frac{x}{r_0}\right)^2+\cdots\right) \tag{9}$$

where r_0 is the reference radius in the magnet. The normal multipole field combination is usually expressed as

$$B\left(x\right)=B_0\left(b_1+b_2\frac{x}{r_0}+b_3\left(\frac{x}{r_0}\right)^2+\cdots\right) \tag{10}$$

Using Eq. 9 and Eq. 10, the normal multipole field components are given by

$$b_1=1\ ,\ b_2=r_0\frac{k}{R_0}\ ,\ b_3=r_0^2\frac{k(k-1)}{2!R_0^2}\ ,\ b_4=\cdots \tag{11}$$

A pure multipole field can be produced with a superconducting coil using the $\cos(n\theta)$ current distribution given by

$$I\left(\theta\right)=I_0\cos(n\theta) \tag{12}$$

where θ is the azimuthal angle, I_0 is the current at the mid-plane, and n is the order of the multipole. Figure 3 shows a schematic view of the $\cos(n\theta)$

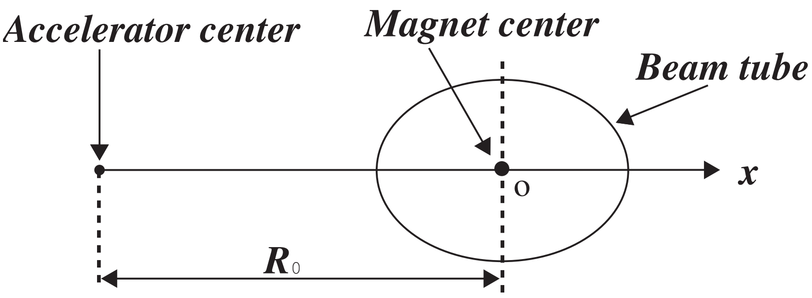

Figure 2: Schematic view of the vertical section of the FFAG accelerator

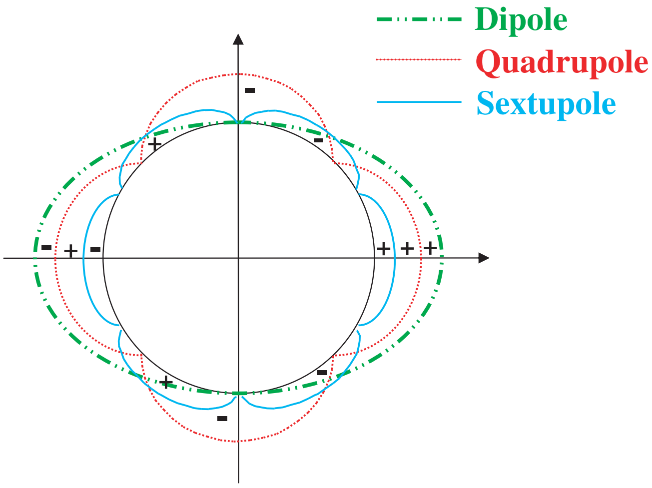

Figure 3: Ideal current distributions for the normal multipole field component

current distributions to generate the magnetic field given by Eq. 8. The current distributions can be realized with a multilayer coil each layer of which produces a pure multipole field. However, the magnetic forces on the coil are complex and difficult to support. It is therefore convenient to combine the coils to give the current distribution shown in Fig. 4 (a) which is a left-right asymmetric distribution. Additionally, the current distribution can be arranged on an ellipse so as to have a large horizontal aperture with a compact coil design. Figure 4 (b) shows the combined current distribution on the ellipse.

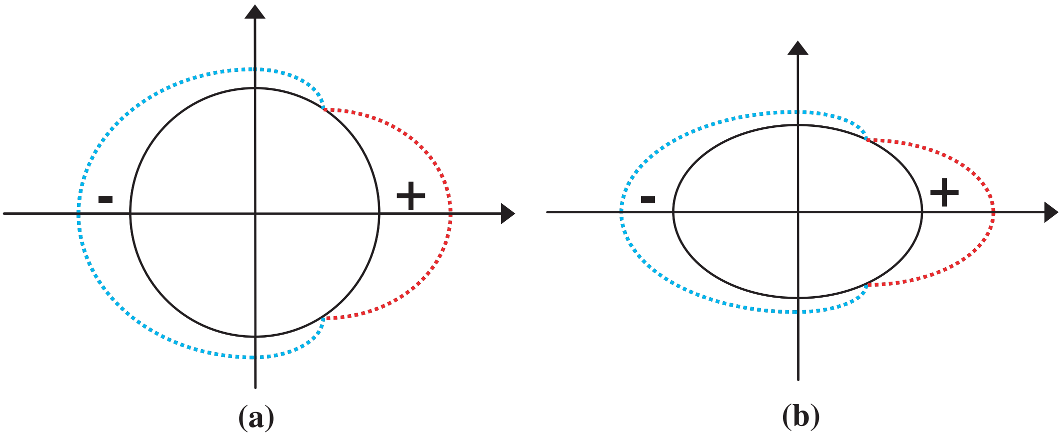

Figure 4: Current distribution to realize combined multipole fields with (a) circular coil aperture and (b) elliptical coil aperture

2.3 Design of 2D coil cross-section

In order to design the coil cross-section that can generate the FFAG magnetic field as described in Eq. 8, a specific computer code was developed. The concept of the code is described in Appendix E. The code can produce the coil cross-section of the single layer that generates the combined magnetic field, which includes many normal multipole components, with high accuracy. The design of the coil cross-section was carried out by using the developed code to have the parameters listed in Table 2. Figure 5 illustrates the 2D cross-section of the coil. The line currents with the same current are arranged on the ellipse. The distance between the line currents are adjusted to give the current distribution shown in Fig. 4 (b). It is convenient to introduce the parameter *local* k, i.e. the local field index, which can be expressed as follows [3]:

$$\textit{local}\, k = \frac{dB}{dx}\frac{R_0 + x}{B} \tag{13}$$

Figure 6 shows the *local* k which was calculated with the cross-section shown in Fig. 5. The results of the calculation satisfy the design requirement for the magnetic field in the range of the beam excursion.

In Appendix F, the relation between the multipole coefficient b_n and the field index k is described.

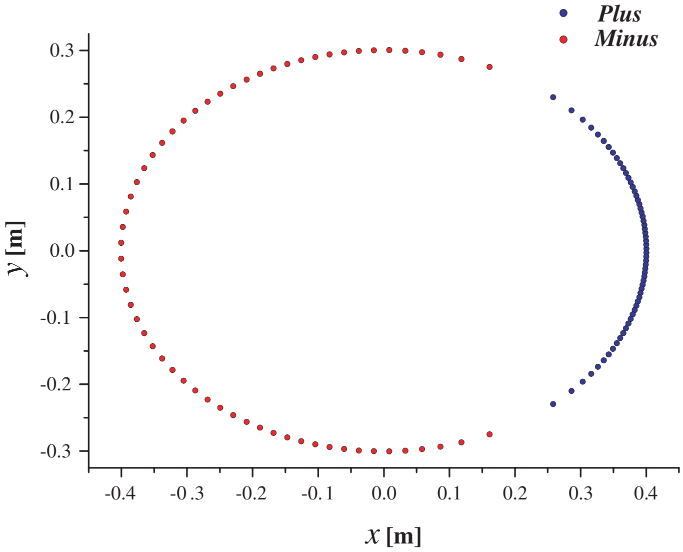

Figure 5: 2D cross-section of a single layer coil wound on an elliptic cylinder

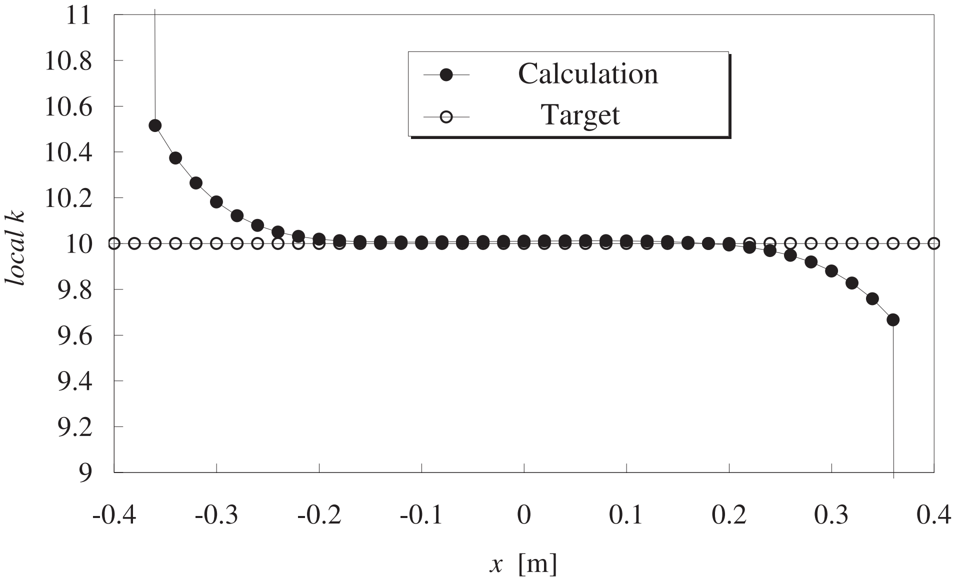

Figure 6: *local* k with the designed cross-section

2.4 Design of 3D coil configurations

2.4.1 Design concept for 3D coils

In the FFAG combined function magnet design, the ratio of the physical length of the coil end to that of the straight section is large, as is also the ratio of the coil aperture to the coil length. Hence, the end section of the coil configuration has a great influence on the magnetic field quality. The 3D coil configuration was designed with the design concept that the integrated magnetic field strength fulfills the design requirement. The integrated magnetic field strength BL is given by Eq. 14, which is the vertical magnetic field B integrated along an arc orbit at each radius, and is written:

$$BL = \int B ds \tag{14}$$

In addition, the integrated magnetic field was evaluated in detail with the $\mathit{local}\, k+1$ which is obtained for the BL. The $\mathit{local}\, k+1$ is given as follows [12]:

$$\mathit{local}\, k+1 = \frac{d\,(BL)}{dx}\frac{R_0 + x}{BL} \tag{15}$$

Thus, owing to the difference in magnetic length corresponding to different particle orbits, k should be replaced by $k+1$ in the design requirement.

2.4.2 Coil design method

The design of the 3D coil configuration was performed with the flow diagram as shown in Fig. 7. The process of designing the coil configuration consists, first of all, in defining a 2D cross-section of the coil. After that, the 3D coil configuration based on the cross-section is designed, and the integrated magnetic field is calculated. To evaluate the results of the calculation, the $\mathit{local}\, k+1$ is obtained from the calculation of the integrated magnetic field. In the case that the $\mathit{local}\, k+1$ fulfills the design requirement, the design of the coil configuration is completed. In the case that $\mathit{local}\, k+1$ does not meet the design requirement, on the other hand, the coil configuration is redesigned with a renewed target.

2.4.3 Optimization for integrated magnetic field

A logic of optimization for the coil configuration was developed to meet the design requirement for the integrated magnetic field [13]. The diagram of the logic is shown in Fig. 8. First of all, the coil configuration is designed by using an initial target, and $\mathit{local}\, k+1$ is calculated with the designed coil

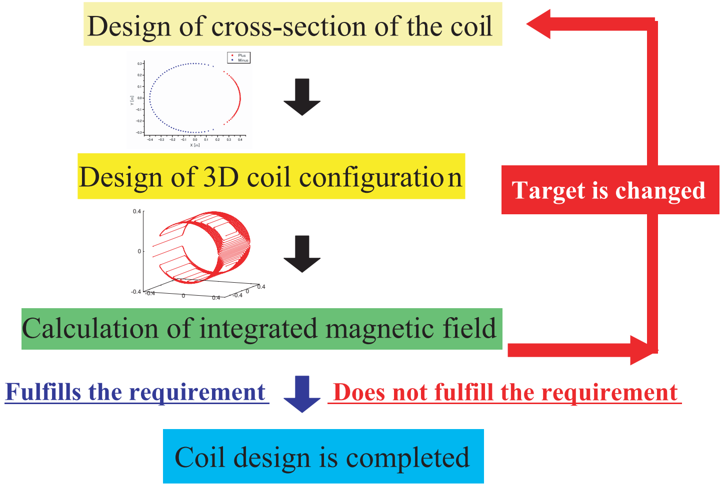

Figure 7: Flow diagram of designing coil

configuration. When the $local\, k+1$ does not fulfill the design requirement, components of integrated magnetic field for the target and the calculation results are obtained respectively. The component of integrated magnetic field means a coefficient of the integrated magnetic field which is expanded into a power series as follows:

$$BL = (BL)_0 \left\{ c_1 + c_2 \frac{x}{r_0} + c_3 \left(\frac{x}{r_0} \right)^2 + \cdots \right\} \tag{16}$$

The coil configuration is redesigned with the new target that takes the difference between the coefficient of target and that of calculation into account as follows:

$$b_{n\, new} = b_{n\, old} + (c_{n\, calculation} - c_{n\, target}) \tag{17}$$

The coil configuration was designed using this optimization process.

2.5 Type of coil configurations

In designing the 3D coil layout, two types of configuration were investigated. One is a ”saddle shaped coil” with a left-right asymmetric cross-section as shown in Fig. 9 [14]. The saddle shaped coil has a triangular zone at the coil end as shown in Fig. 11 (a), because the straight lengths are different for each turn. The cross-section of the straight section is lost at the coil end. As a consequence, the coil end has a strong influence on the magnetic field. In order to meet the design requirement for the integrated magnetic field, it

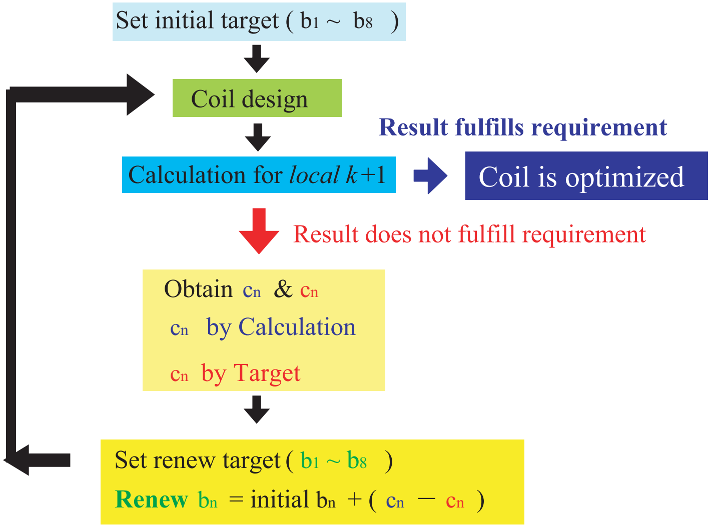

Figure 8: Logic of optimization for coil design

is essential to design the straight section of the coil so as to cancel the effect of the coil end.

The other is the so-called ”single winding coil” as shown in Fig. 10 [9]. Figure 10 (a) illustrates the coil layer that is wound from the upper pole to the bottom pole, one coil layer consists of one coil configuration. The next coil layer is wound from the bottom pole to the upper pole as shown in Fig. 10 (b). The schematic view of the coil end for each layer in x-z plane is illustrated in Fig. 11 (b) and (c). The single winding coil has a feature that the difference in the straight length of the coil at the same position in each layer can be minimized when the number of the coil layers is even. Figure 12 illustrates the difference in the straight length of the each coil with two layers at the same position in each layer when the coil end is rectangular. The straight lengths of the saddle shaped coil are very different, whereas those of the single winding coil can be uniform. Moreover, in the single winding coil, it is not necessary to design the straight section of the coil so as to cancel the effect of the coil end, because the effect of the coil end on the integrated magnetic field can be reduced when the number of the coil layers is even. The single winding coil configuration is, however, less efficient and up-and-down asymmetric, which introduces unwanted skew components of the field. This will be discussed later.

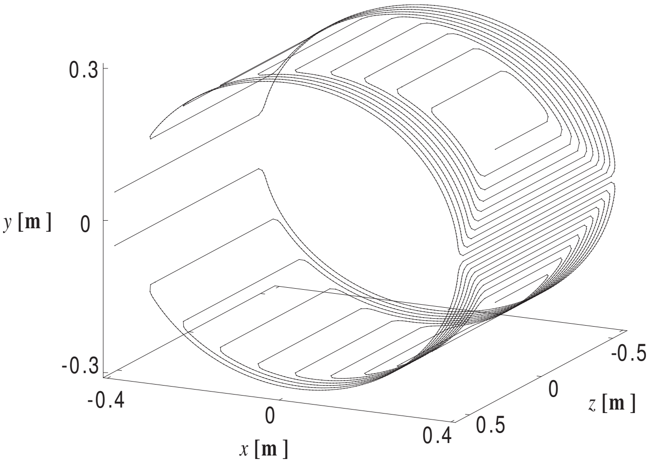

Figure 9: Saddle shaped coil with left-right asymmetric cross-section

2.6 Calculation

The coil design based on each coil configuration was performed with the design method so as to fulfill the design parameters listed in Table 2. The specifications of each coil configuration are listed in Table 3 and Table 4, and Fig. 13 illustrates each coil configuration in x-z plane. The integrated magnetic field was calculated by using the designed coil.

2.6.1 Region of magnetic field calculation

After the coil configuration was designed, the magnetic field generated by the coil was calculated by means of the Biot-Savart law with line currents in the coil. Figures 14 illustrates schematic views of the region of magnetic field calculated for the focusing and defocusing coils. The integrated magnetic field was obtained by integrating vertical magnetic field along the arc orbit in a half cell where the angle is between 0 °and 15 °as shown in Fig. 14.

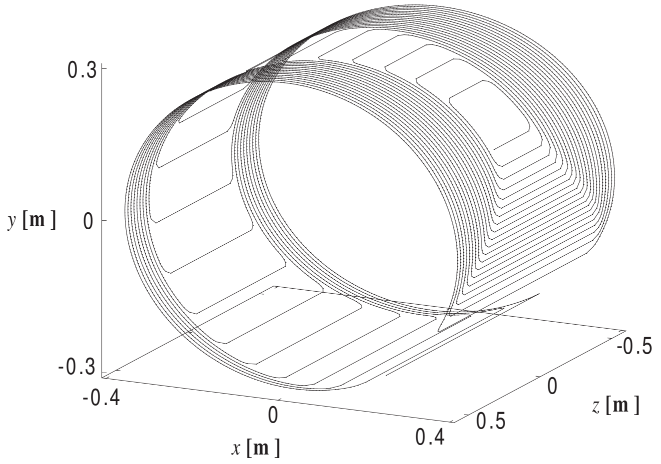

(a) Odd layer

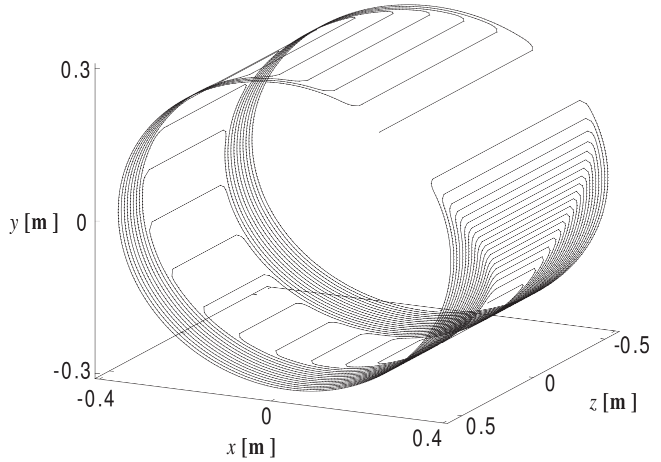

(b) Even layer

Figure 10: Single winding coil with left-right asymmetric cross-section

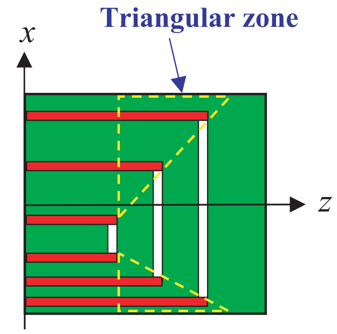

(a) Coil end of saddle shaped coil

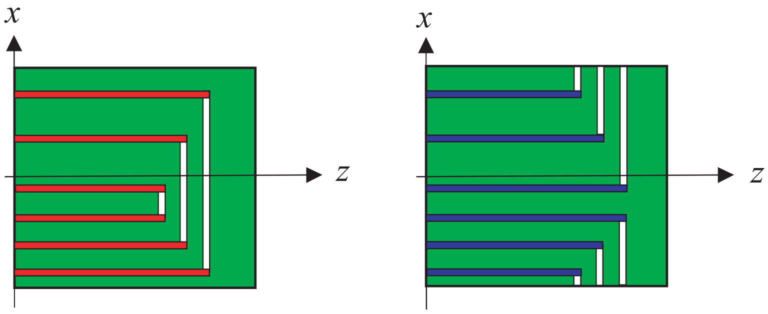

(b) Odd layer coil end
of single winding coil

(c) Even layer coil end
of single winding coil

Figure 11: Schematic view of each coil end in the case of rectangular coil end

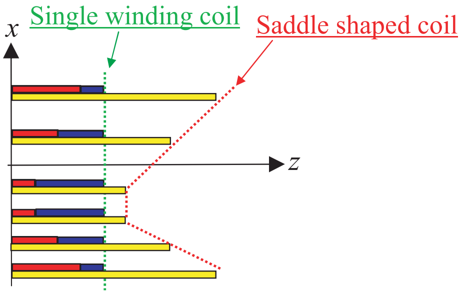

Figure 12: Schematic view of straight length for each coil in the case of two layers which consist of rectangular coil end

Table 3: Design parameters for the saddle shaped coil

	Focusing	Defocusing
Number of layers	1	1
Angle of the sector	11.6 degree	5.8 degree
Number of turn for 1 layer	180	64

Table 4: Design parameters for the single winding coil

	Focusing	Defocusing
Number of layers	2	2
Angle of the sector	11.6 degree	5.8 degree
Number of turn for 1 layer	180	64

2.6.2 Results of calculation

The $local\, k + 1$ was obtained from the BL calculated with the designed coil configuration. In the coil design, the field quality is required in region of $local\, k + 1 \pm 0.2$, as determined empirically from the particle tracking simulation. Figure 15 shows the first calculation results without the logic shown in Fig. 8. In the first calculation, the $local\, k + 1$ of the single winding coil is better than that of the saddle shaped coil.

The coil configurations were redesigned several times in terms of the iterative calculation in order to achieve the target. As a result, the calculation results came close the target and also fulfilled the design requirement as shown in Fig. 16. The results of the calculation are summarized in Table 5.

In addition, canceling the effect of the coil end was examined. Multipole coefficients b_n for both coil types in the straight section on the mid-plane are listed in Table 6. The multipole coefficients b_n of both coil types differ from the target, in which the field index k is 10, used in design of 2D coil cross-section.

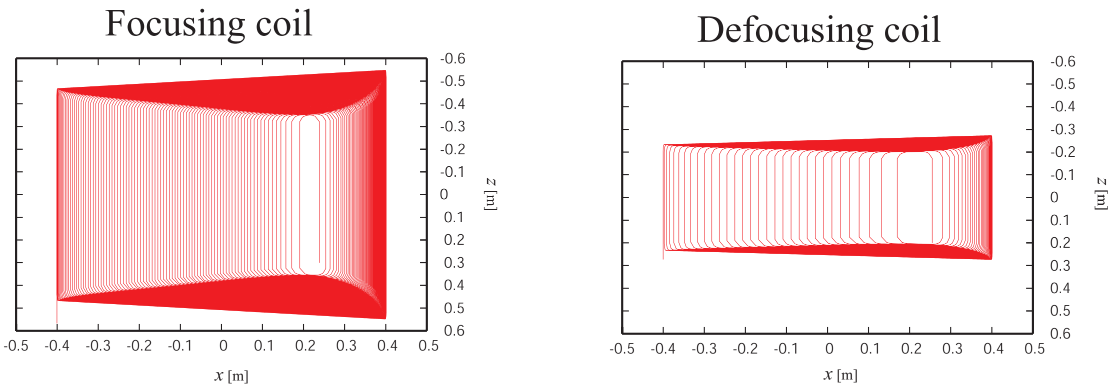

(a) Saddle shaped coil

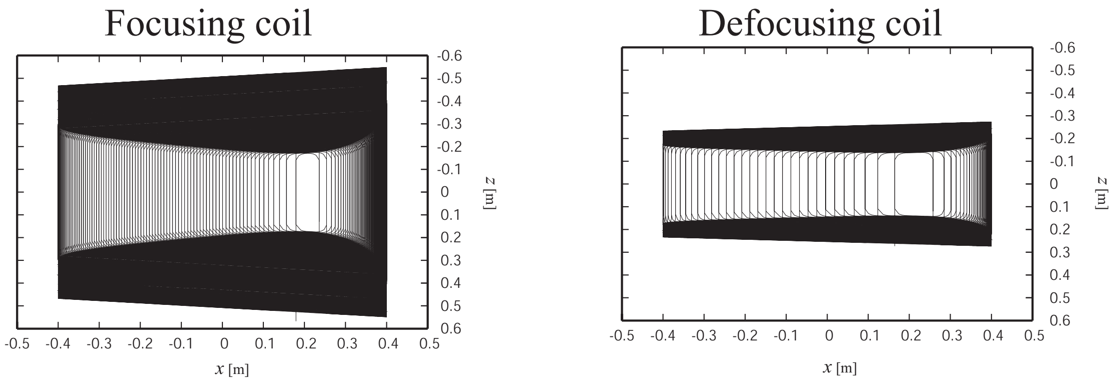

(b) Single winding coil

Figure 13: Saddle shaped coil and single winding coil in x-z plane

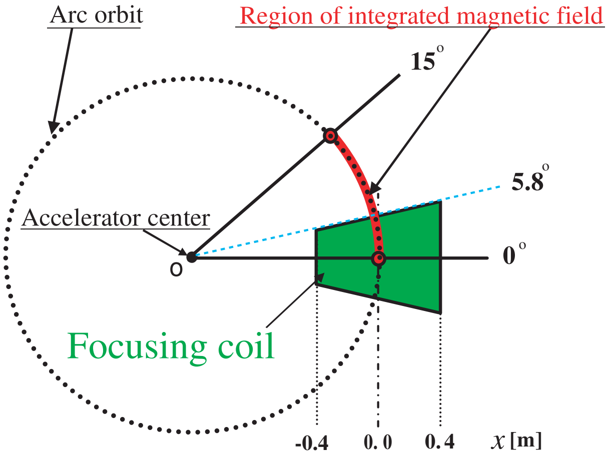

(a) Region of magnetic field calculated in the focusing coil

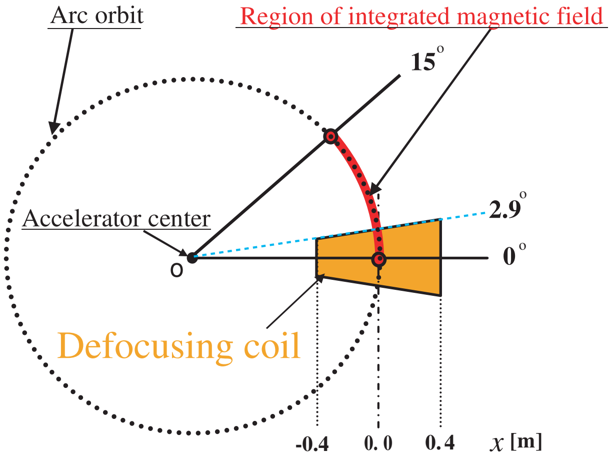

(b) Region of magnetic field calculated in the defocusing coil

Figure 14: Region of calculated magnetic field for each coil

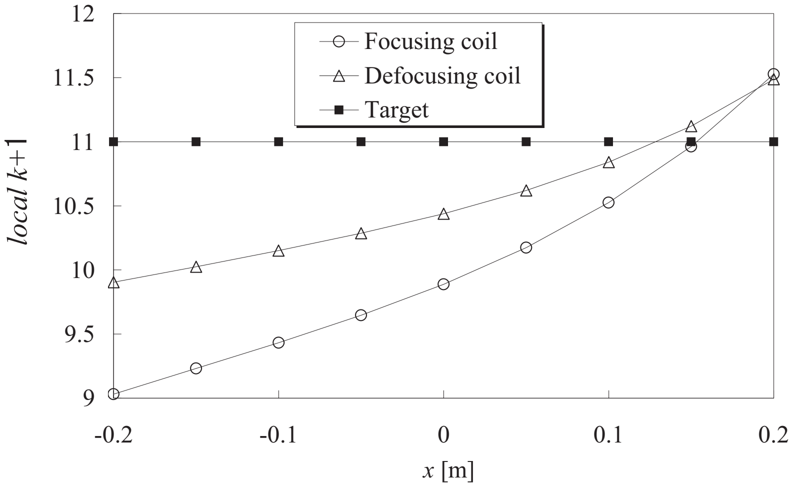

(a) Saddle shaped coil

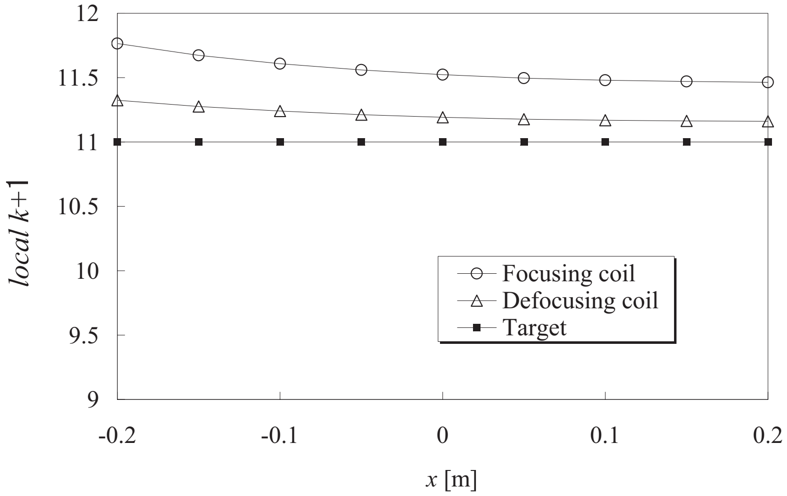

(b) Single winding coil

Figure 15: $local\, k + 1$ in initial design of the focusing and defocusing coils

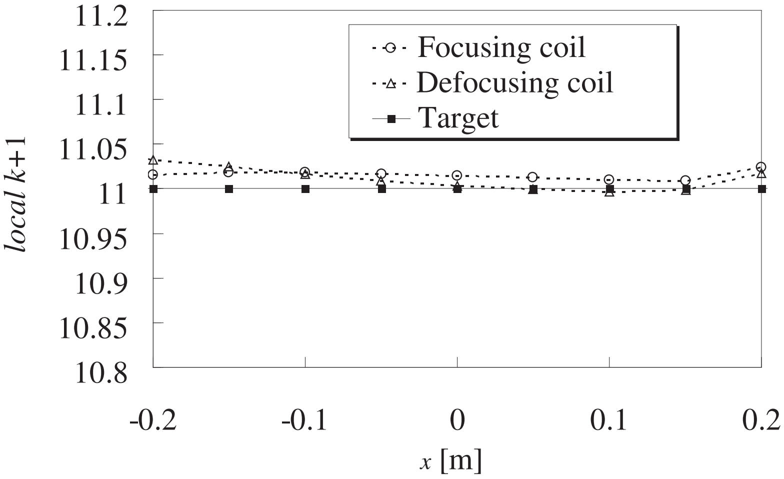

(a) Saddle shaped coil

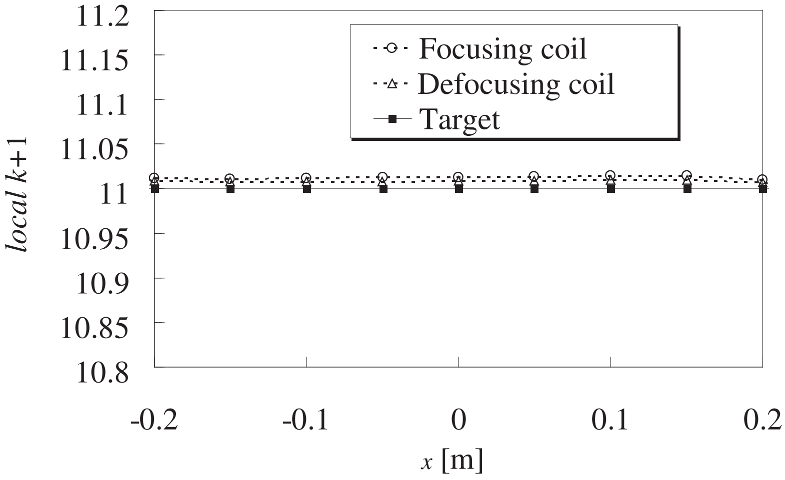

(b) Single winding coil

Figure 16: *local* $k+1$ in optimized design of the focusing and defocusing coils

Table 5: Result of calculations of the magnetic field for the saddle shaped coil and the single winding coil

Coil type	*local* $k + 1$
Focusing coil (Saddle shape)	11.01 ∼ 11.02
Defocusing coil (Saddle shape)	11.00 ∼ 11.03
Focusing coil (Single winding)	11.01
Defocusing coil (Single winding)	11.01

Table 6: Multipole coefficient b_n for each coil type at $z = 0$ m, reference radius = 0.2 m.

	Saddle shaped coil	Single winding coil	Field index $k = 10$
b_1	10000.0	10000.0	10000.0
b_2	4054.5	3457.9	4000.0
b_3	704.3	923.5	720.0
b_4	-12.2	125.6	76.8
b_5	-57.3	-5.1	5.4
b_6	-17.4	-9.6	0.3
b_7	-2.3	-6.6	0.0

2.7 Particle tracking simulation

2.7.1 Closed orbit and beam energy

The simulation of tracking a particle in the FFAG ring was performed with the magnetic field generated by the designed coils in order to confirm that the coil configuration could be utilized as the FFAG magnet. The particle trajectory was obtained in the simulation by solving continuously 3-dimensional equations of motion for a charged particle in the magnetic field, which is taken to be the 3-dimensional magnetic field map generated by the designed coils, using the 4th order Runge-Kutta method [15]. The magnetic field at the particle's position was given by linear interpolation of lattice points in the field map. Parameters for the FFAG accelerator listed in Table 1 were used in the simulation. The layout of the FFAG accelerator composed of 24 magnets is illustrated in Fig. 1. The sector angles of the focusing magnet and the defocusing magnet are 11.6 °and 5.8 °, respectively. Each magnet is

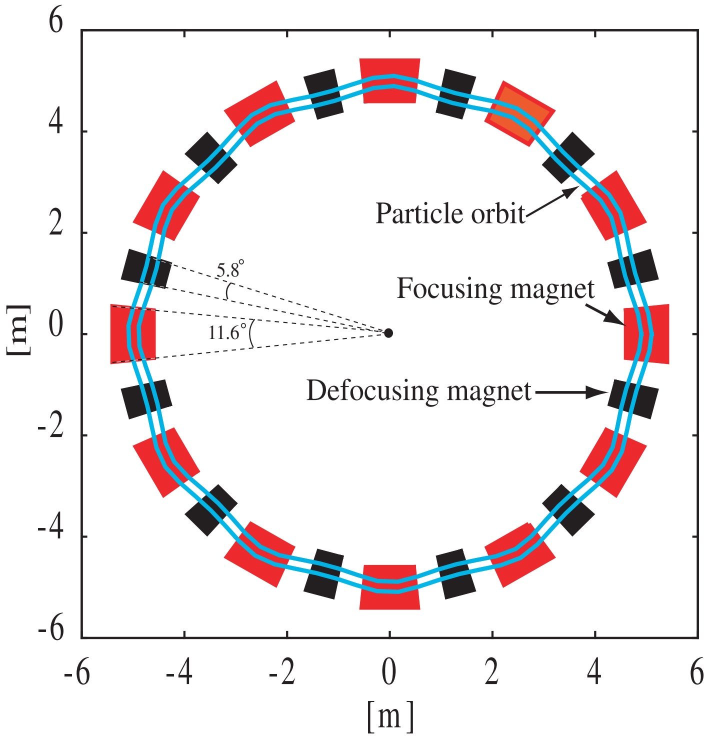

Figure 17: Layout of the FFAG accelerator with closed orbits

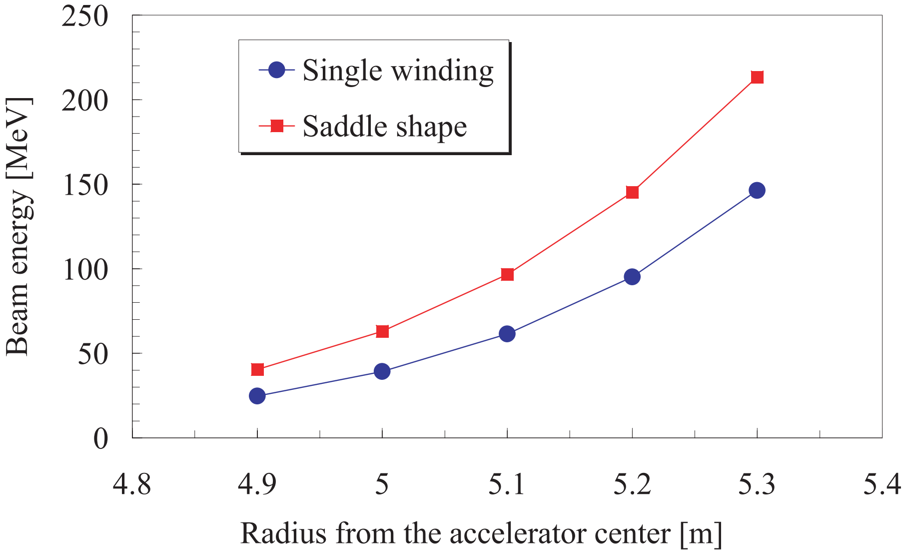

Figure 18: Beam energies for saddle shaped coils and single winding coils

located alternately with a space, the angle of which is 6.3 °. The wavy lines show closed orbits obtained with the simulation as shown in Fig. 17. Beam energies for the saddle shaped coil and the single winding coil are shown in Fig. 18. The beam energy for the saddle shaped coil is larger than that of the single winding coil, and the difference between the beam energies increases as the orbit radius becomes large.

2.7.2 Tune

Vertical and horizontal tunes were calculated in terms of the tracking simulation in order to verify that a particle can be accelerated with the designed coils. The tunes of the single winding coil and the saddle shaped coil are shown in Fig. 19, respectively. In Fig. 19(a), the tunes of the saddle coil stay between resonance lines without crossing the lines in a tune diagram. On the other hand, the tunes of the single winding coil move, crossing resonance lines at various beam energies in Fig. 19(b). The result of the particle tracking is summarized in Table 7.

The relation between the tunes and field index k is given in Appendix F, and horizontal and vertical emittances of each coil type calculated by the tracking are described in Appendix G.

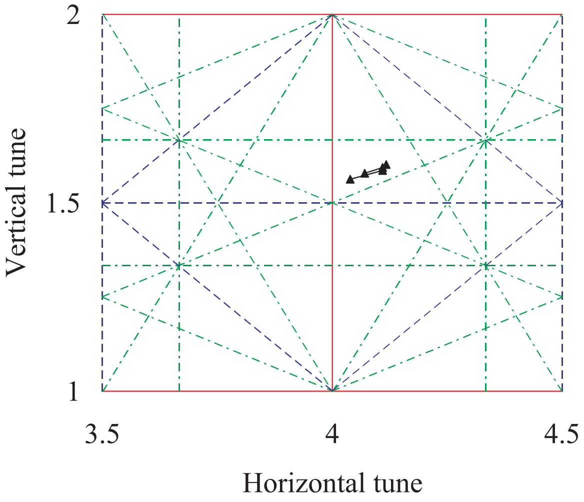

(a) Saddle shaped coil

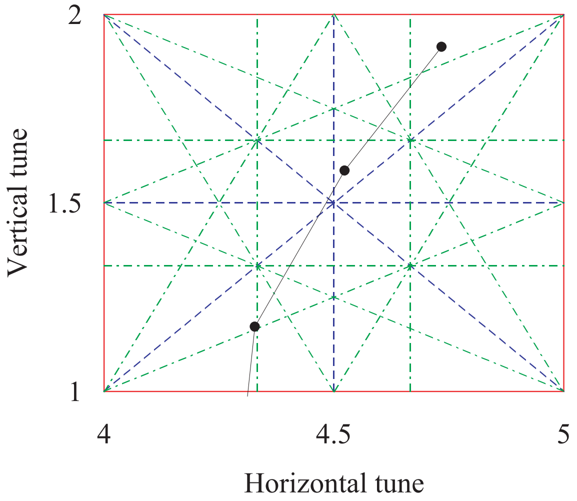

(b) Single winding coil

Figure 19: Turn diagram for each coil type

Table 7: Particle tracking results with the saddle shaped coil and the single winding coil

	Saddle shaped coil	Single winding coil
Beam energy	40.4 ~ 213.4	24.7 ~ 146.3
Horizontal tune	4.07 ~ 4.12	4.21 ~ 4.73
Vertical tune	1.58 ~ 1.60	0.37 ~ 1.91

2.8 Comparison of the saddle shaped coil with the single winding coil

As shown in Fig. 19, the tunes associated with the saddle shaped coil stay between resonance lines without crossing them in the tune diagram, but tunes associated with the single winding coil cross a number of lines. The difference in tunes is due to the difference of the coil configuration. Figure 20 shows the magnetic field in the x direction on the mid-plane at the coil center for both coil configurations. The single winding coil generates a significant magnetic field in the x direction that gives rise to skew magnetic fields because of the up-down asymmetry of the coil.

In addition, the effective length of the saddle shaped coil is longer than that of the single winding coil, so that the maximum beam energy with the saddle shaped coil is greater than that of the single winding coil, as shown in Fig. 18. Consequently, the saddle shaped coil is more suitable for use in the FFAG magnet.

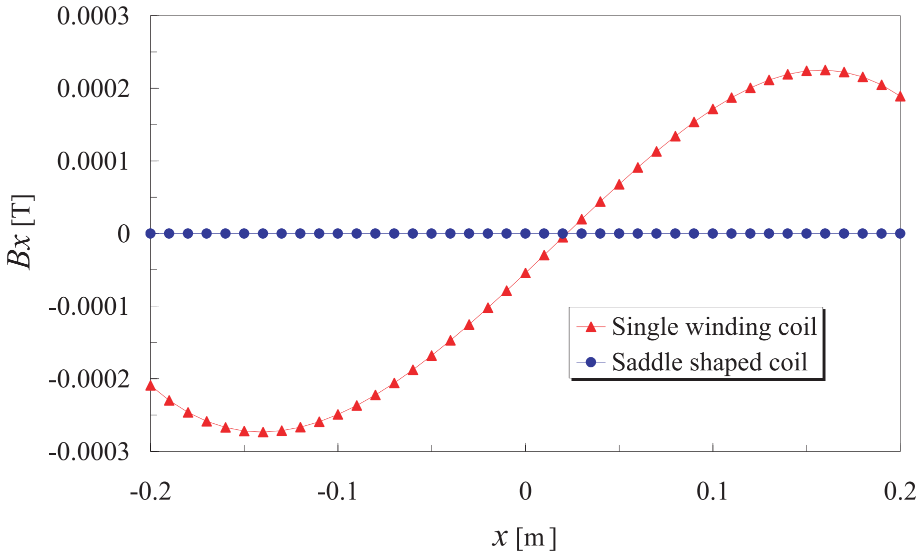

Figure 20: Magnetic field B_x on the mid-plane at coil center

2.9 Basic design of superconducting combined function magnets with iron yoke

As the next task, the basic design of the superconducting FFAG magnet was carried out. The superconducting magnet was designed for use in the FFAG accelerator for medical applications.

2.9.1 Magnetic design

When an iron yoke is placed close to coils, as is often the case for high field accelerator magnets, the iron is partially saturated and the calculation of the field requires the use of finite element (FE) programs such as TOSCA [16] and ROXIE [17]. The present work is essentially devoted to the study of the feasibility of realizing the complicated asymmetric field shape, integrated over the length of the relatively short magnet, required for a practical FFAG.

In this study, the warm iron alternative was first adopted for the iron yoke which surrounds a superconducting coil. The parameters for the focusing version of the superconducting FFAG magnet are listed in Table 8. The magnet consists of multilayer coil with a left-right asymmetric cross-section, surrounded by a warm iron yoke.

For the magnetic design of the superconducting FFAG magnet, the coil was first considered to be surrounded by an iron yoke. The image current

Table 8: Basic design parameters of superconducting FFAG magnet for focusing

Major axis of the beam pipe	0.8 m
Minor axis of the beam pipe	0.6 m
Longitudinal length of the coil	1.09 m
Field index, k	10
Distance between the center of magnet and the center of accelerator	5 m
Vertical magnetic field at the center of magnet	1.0 T
Beam excursion	0.4 m
Number of turn for one coil layer	180
Number of coil layer	30
Iron yoke	
Inside diameter	1.6 m
Outside diameter	2.0 m
Longitudinal length of iron yoke	1.1 m

was used to simulate analytically the effect of the iron yoke in the design, based on the concept described in Appendix H. In the coil configuration surrounded by an iron yoke, huge magnetic forces act on the coil due to magnetic interaction between the coil and the iron yoke. The coil design was therefore performed with the following process. The coil cross-section fulfilling the required *local* k, was designed with displacement of the central axis of the iron yoke from that of the coil in order to minimize the magnetic decentering force. After the cross-section was designed, the magnetic force generated on the coil was calculated. The central axis of the iron yoke that minimizes magnetic force on the coil was obtained by iteration. The 3D coil configuration was designed with evaluation based on integrated magnetic field after the central axis of the yoke was determined. The coil and image currents are illustrated in Fig. 21. Figure 22 shows the *local* $k + 1$ obtained with the coil surrounded by the image currents. The magnetic flux in the magnet is also illustrated in Fig. 23.

In addition, peak magnetic field in the coil was studied. It is essential to figure out peak magnetic field strength generated on a conductor in order to ensure the stable operation of a superconducting magnet. The peak magnetic field on the designed coil with image currents was obtained when the vertical magnetic field strength is 1.0 T at the center of the coil. In order to simplify

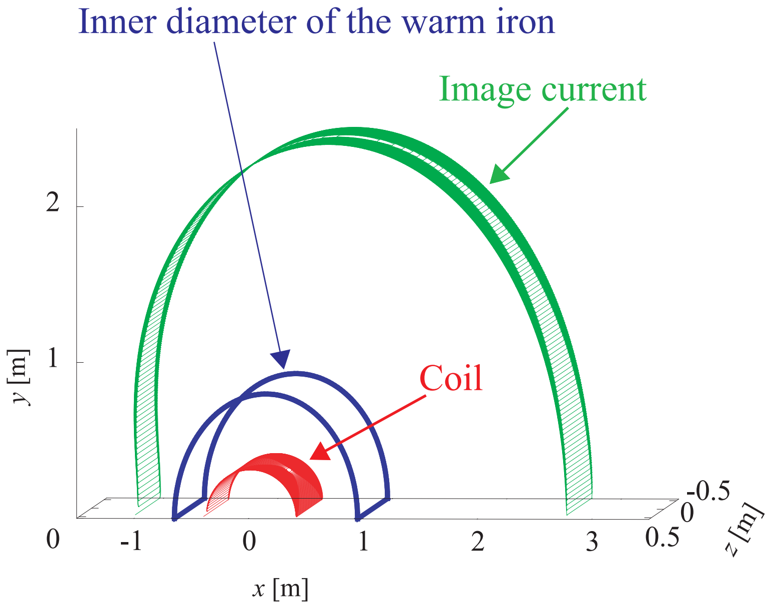

Figure 21: Coil configuration with image current

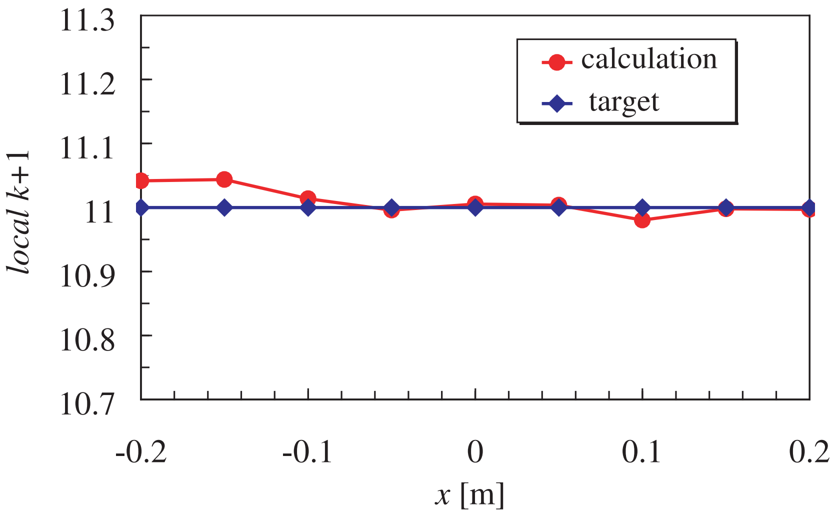

Figure 22: *local* $k+1$ of the superconducting FFAG magnet

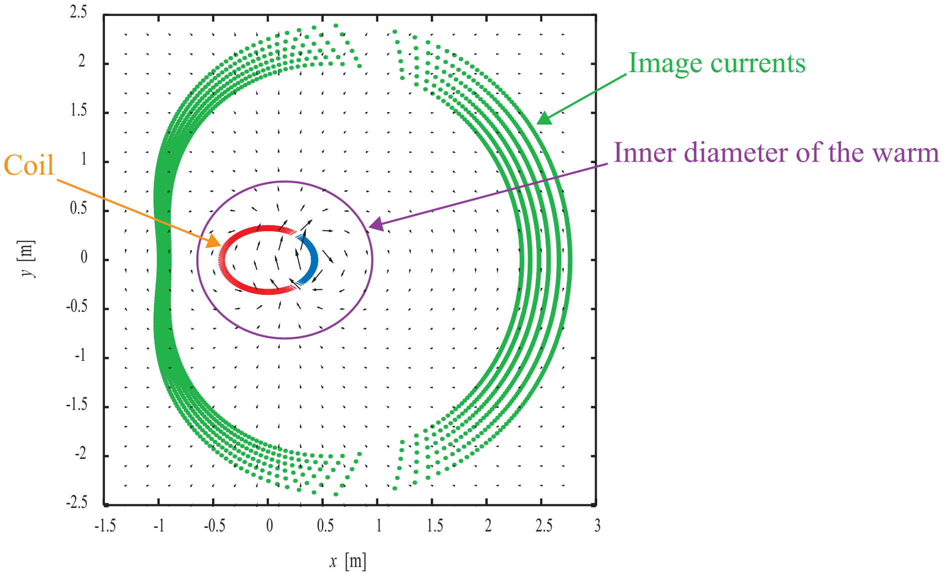

(a) Magnetic flux in the magnet

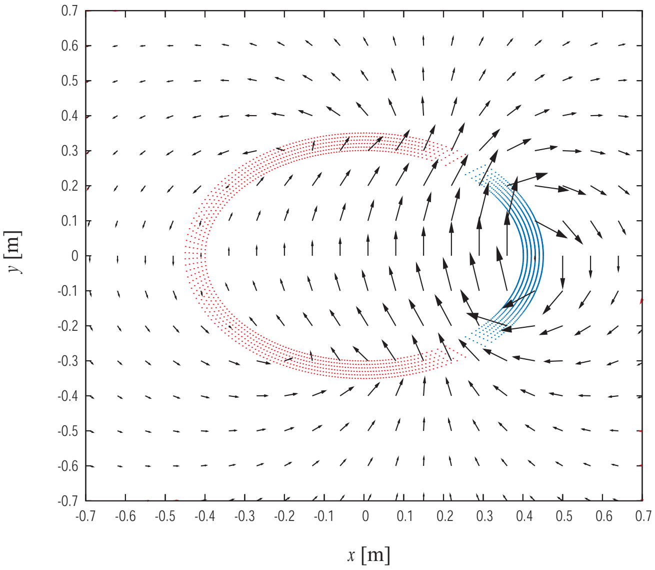

(b) Magnetic flux around the coil in the magnet

Figure 23: Magnetic flux in the magnet

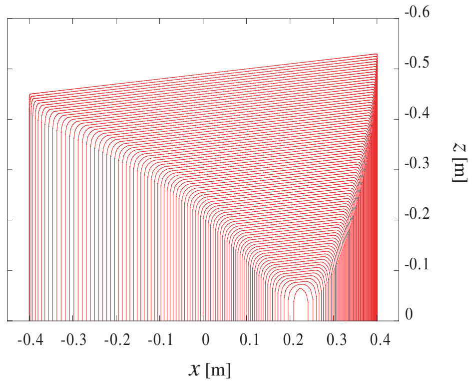

(a) Coil end shape of 1st and 4th layout

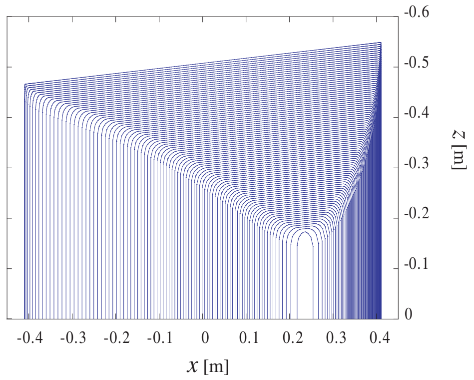

(b) Coil end shape of 2nd and 5th layout

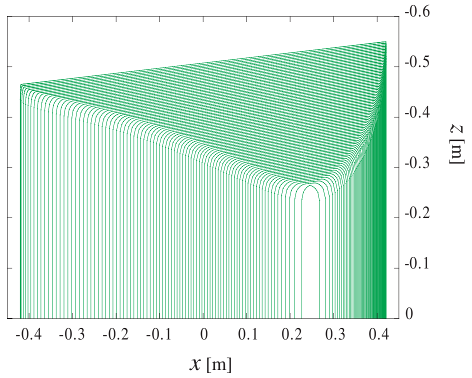

(c) Coil end shape of 3rd and 6th layout

Figure 24: Coil end shape for each layer

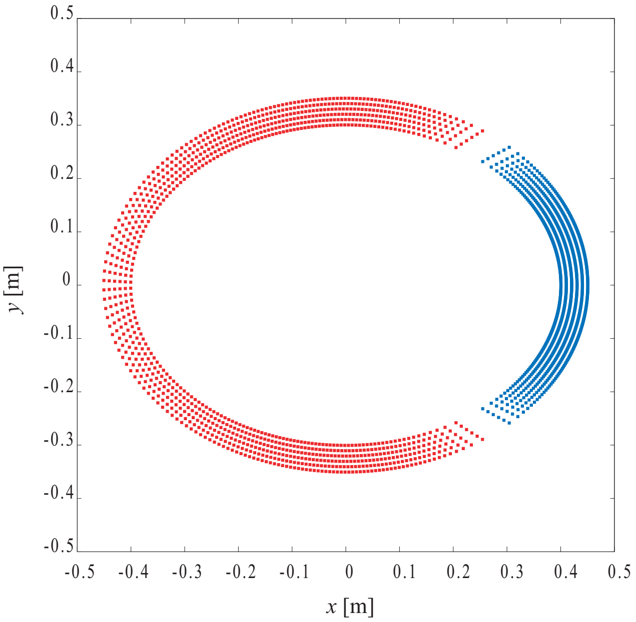

Figure 25: Coil cross-section

the calculations, the number of coil layers was reduced from 30 layers to 6 layers, each of which having a different end shape as illustrated in Fig. 24. Figure 25 illustrates the cross-section of the coil, the aperture of which is given in Table 9. The distance between turns at the coil end for each coil layer is listed in Table 10. Figure 26 shows the load line of the designed coil. When the vertical magnetic field is 1.0 T at the center of the coil, the operating current is 278 A and the peak field is 3.4 T on the coil. In the case that the coil is cooled below 6 K, there is a margin concerning quench as shown in Fig. 26. Based on the above condition, the stored energy per unit length is about 1 MJ, which are given by the 2-dimensional calculation of the coil cross-section [18]. As the result, the coil was found to be 27 H.

The full design study of the superconducting FFAG magnet was performed with FEM(TOSCA), and is described in Appendix I.

Table 9: Aperture of each coil layer

Layer number	Aperture (major axis × minor axis)
1th	0.80 m × 0.60 m
2th	0.82 m × 0.62 m
3th	0.84 m × 0.64 m
4th	0.86 m × 0.66 m
5th	0.88 m × 0.68 m
6th	0.90 m × 0.70 m

Table 10: Distance between turns at the coil end

Layer number	Distance between turns at the coil end
1th	4 mm
2th	3 mm
3th	2 mm
4th	4 mm
5th	3 mm
6th	2 mm

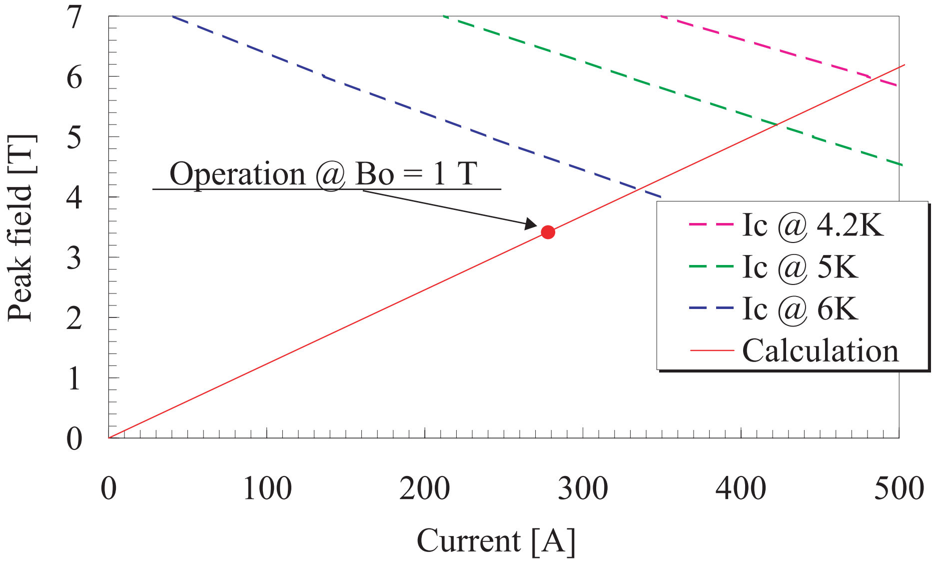

Figure 26: Load line

2.9.2 Structural design

In the structural design of the superconducting FFAG magnet which consists of a multilayer coil with left-right asymmetric cross-section, the studies were carried out in order to determine the magnetic force on the coil when the coil is surrounded with or without an iron yoke, and to evaluate the distortion of the magnet by the magnetic force.

In the coil without the iron yoke, asymmetrical magnetic forces act on the coil as shown in Fig. 27. A relatively large magnetic force is generated in the direction tangential to the cross-section, together with a small perpendicular force generated on the low field side. The cause of the magnetic force is the direction of the magnetic flux on the coil without the iron yoke as illustrated in Fig. 28. Figure 29 shows the magnetic flux on the coil enlarged near the mid-plane. Figure 30 illustrates magnetic forces on the coil surrounded by a warm iron yoke the ID of which is 1.6 m and a cold iron yoke the ID of which is 0.94 m when operated at the same current. Compared to the coil without the iron yoke, there is an increased bursting force on the coil on the low field side with the iron yoke. In the case of the coil surrounded by each iron yoke, magnetic flux is generated on the coil as shown in Fig. 31. Figure 32 illustrates the magnetic flux on the coil surrounded the warm iron yoke, enlarged near the mid-plane.

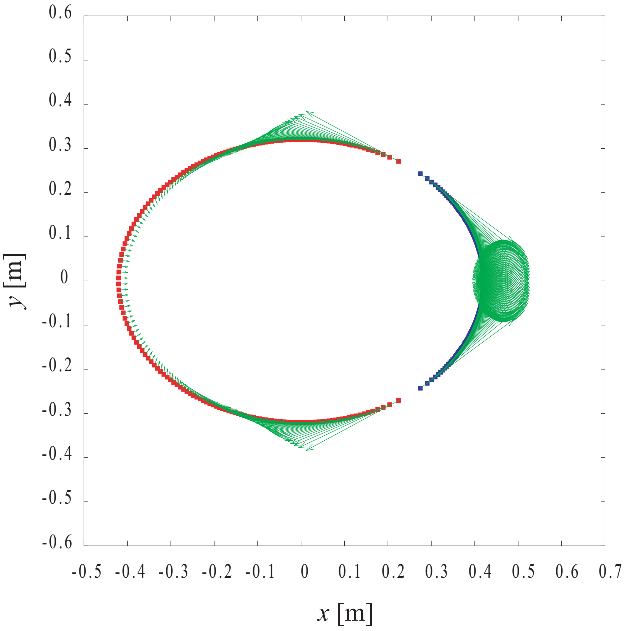

Figure 27: Schematic view of magnetic forces on the coil without iron yoke

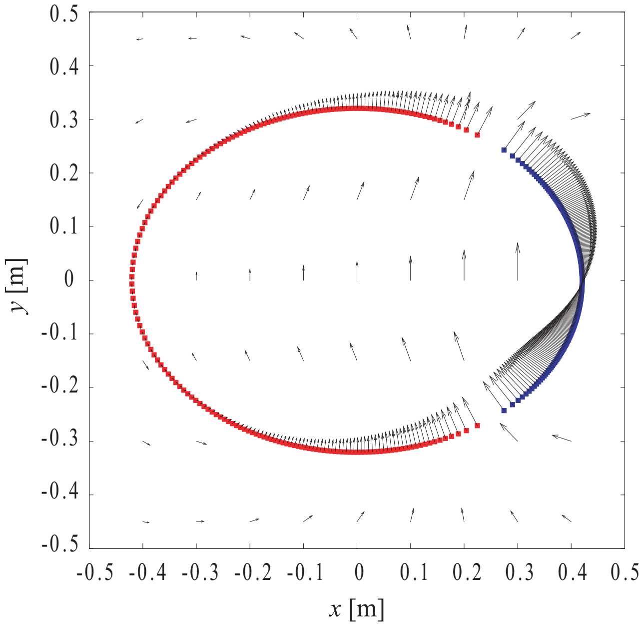

Figure 28: Schematic view of magnetic flux on the coil without iron yoke

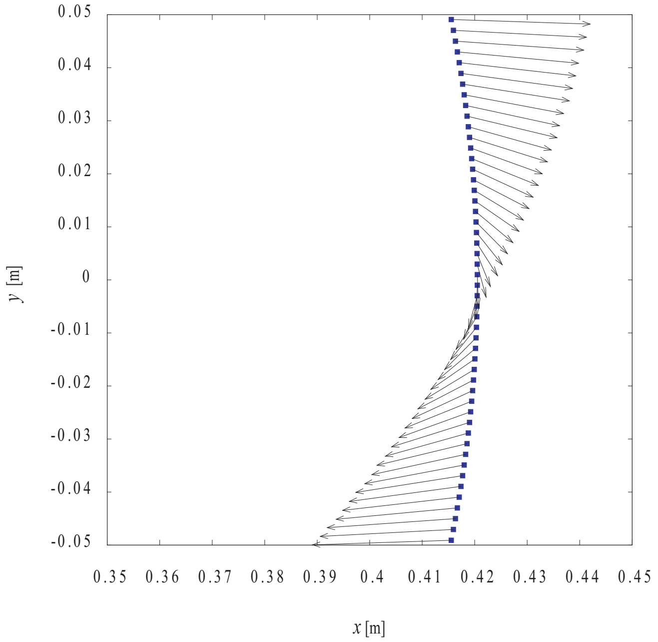

(a) Magnetic flux on the coil without iron yoke on high field side

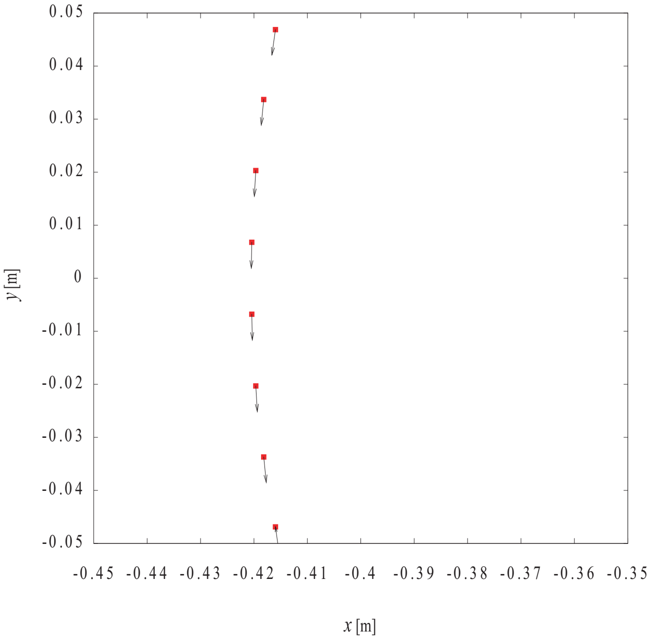

(b) Magnetic flux on the coil without iron yoke on low field side

Figure 29: Schematic view of magnetic flux on the coil without iron yoke near mid-plane

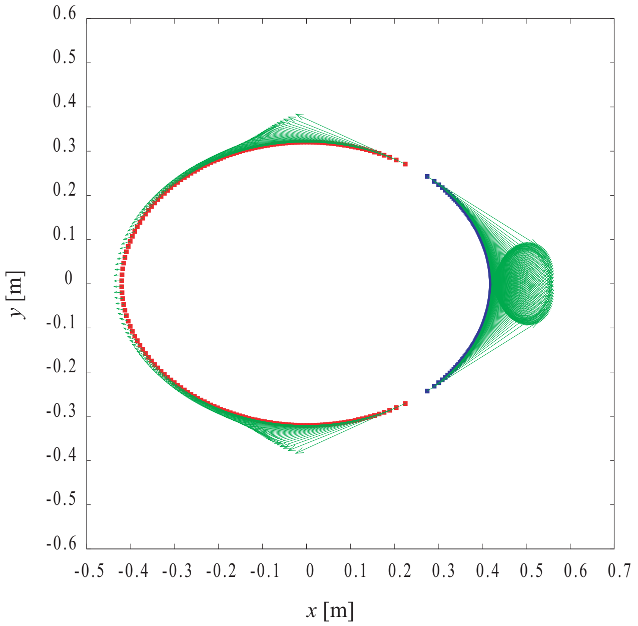

(a) Magnetic force on the coil with warm iron yoke

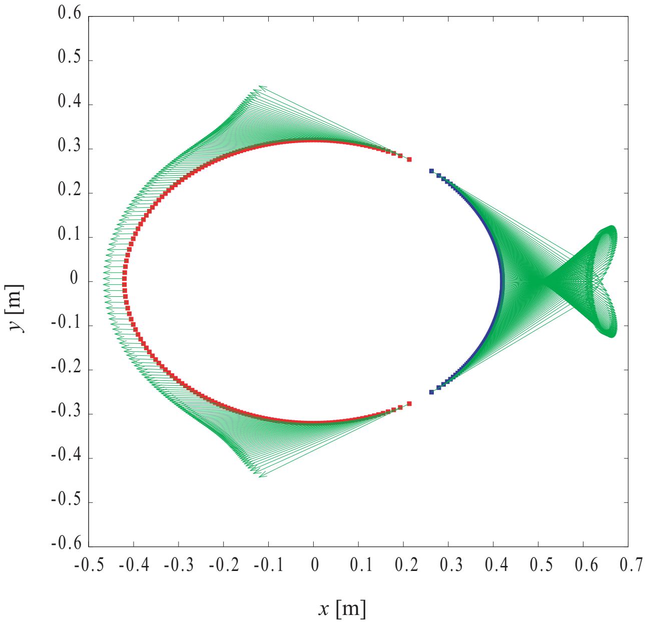

(b) Magnetic force on the coil with cold iron yoke

Figure 30: Schematic view of magnetic forces on the coil with iron yoke

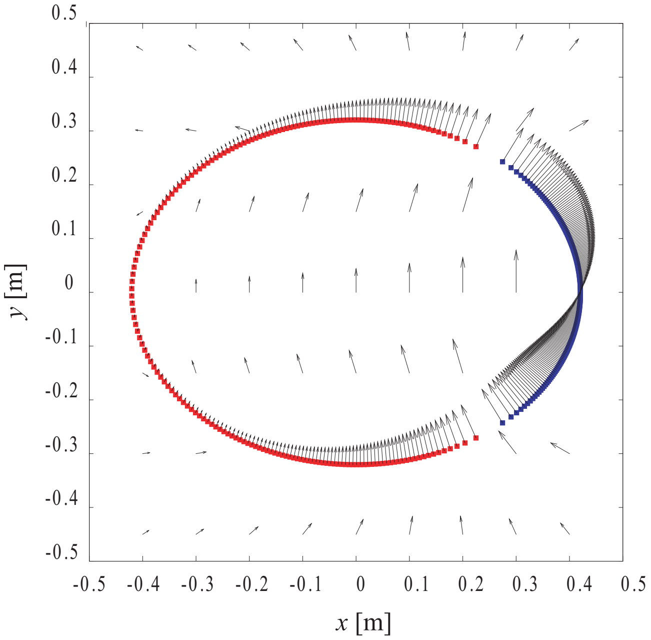

(a) Magnetic flux on the coil with warm iron yoke

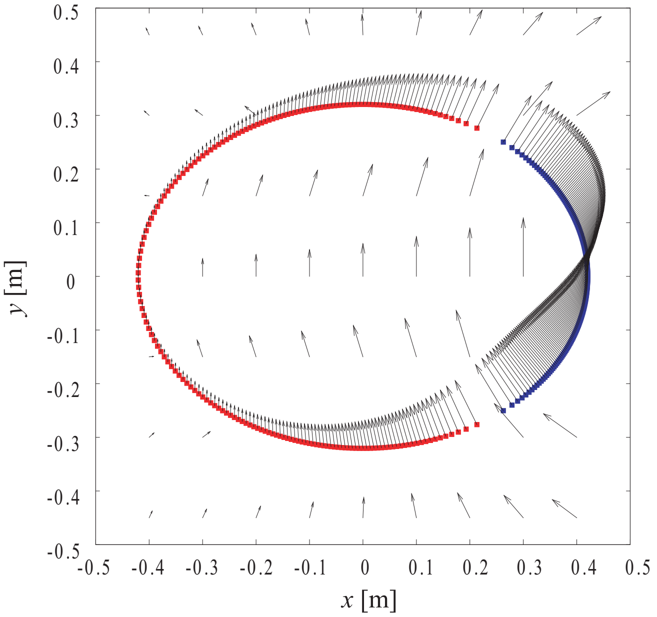

(b) Magnetic flux on the coil with cold iron yoke

Figure 31: Schematic view of magnetic flux on the coil with iron yoke

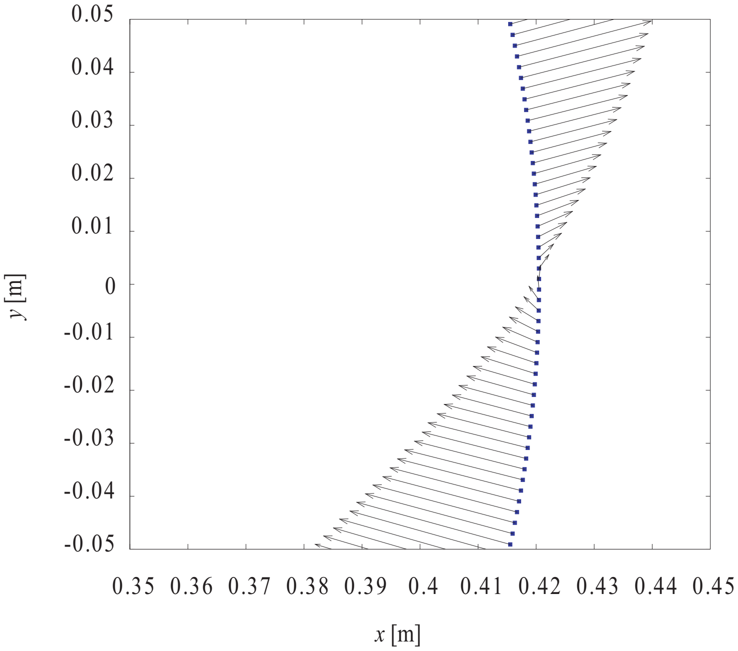

(a) Magnetic flux on the coil with warm iron yoke on high field side

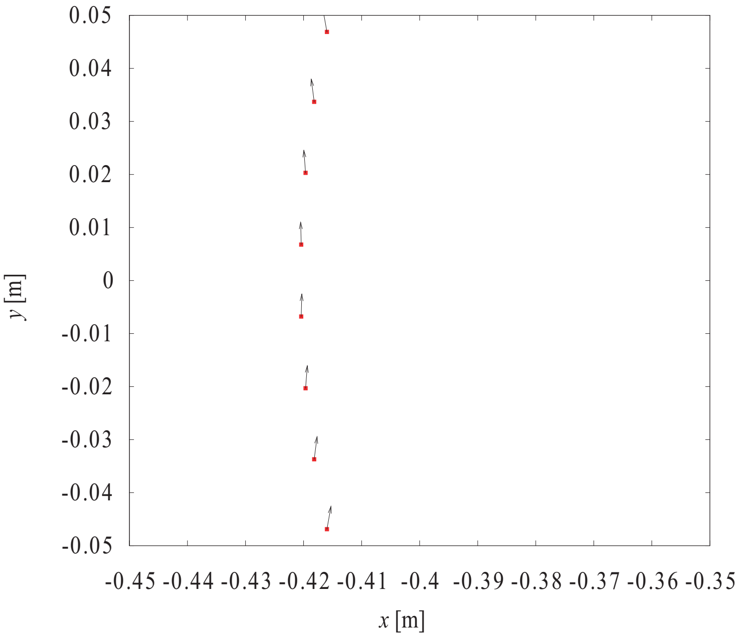

(b) Magnetic flux on the coil with warm iron yoke on low field side

Figure 32: Schematic view of magnetic flux on the coil with warm iron yoke near mid-plane

In the case of a coil surrounded by an iron yoke, a magnetic force tending to move the coil is generated by the interaction between the coil and the iron yoke; its strength is obtained by summing the local magnetic forces on the conductors. The magnetic force on the coil was calculated analytically in 2D by using the coil surrounded by a warm and cold iron yokes the inside diameters of which are 1.6 m and 0.94 m respectively, taking into account the effect of the iron yoke. The cross-sections of each iron yoke are illustrated in Fig. 33. The center axis of the warm iron yoke is displaced from that of the coil to reduce the magnetic force as described previously. The calculated results of magnetic forces on the coil for each iron yoke are given in Fig. 33, in which the strength of the magnetic force for each part of the coil is shown when the magnetic field strength is 1 T at the magnet center. In the horizontal direction, the total net force on the coil with the warm yoke is 694 N/m, on the other hand, that on the coil with the cold yoke is 435390 N/m. The horizontal force on the coil with the warm iron could be eliminated by the further optimization of the coil position. In the vertical direction, there is no decentering force of the coil in both cases, as expected.

In order to examine the distortion of the magnet by the magnetic force, the structural calculation of the magnet with the outer shell, which is made of iron or stainless steel, was made in 2D by mean of ANSYS [19]. Figure 34 illustrates the cross-section of the magnet used in the calculation. The cross-section of the coil was modelled using conductors of size 1 mm × 55 mm, simulating the cross-section as shown in Fig. 25. For a practical magnet design, an elliptic rather than a circular shape was adopted as a bore of the outer shell, to reduce the space between the coil and the shell. SUS 304L was attached inside the coil as an inner structural shell. Before the structural calculation, the magnetic force on the conductor was obtained by a calculation in which the magnetic field strength is about 1 T at the magnet center with the above model. Conditions of constraint were as follows: points on the mid-plane do not move in the vertical direction, one point at which the inner structural shell is attached on the mid-plane on the low magnetic field side and does not move in the horizontal direction as well as in the vertical direction. Osculating elements were used on the boundaries which are between the resin and the inner shell, and between the resin and the outer shell. The characteristics of materials used in the magnet are listed in Table 11. In the case of an iron-free coil in which the SUS304L is utilized as the outer shell, the distortion caused by the magnetic force is illustrated in Fig. 35. The maximum distortion is about 0.3 mm when the magnetic field strength is about 1 T at the magnet center. On the other hand, Fig. 36 (a) shows the distortion in the magnet surrounded with the iron yoke; the maximum distortion is about 0.4 mm under the magnetic field. It is therefore

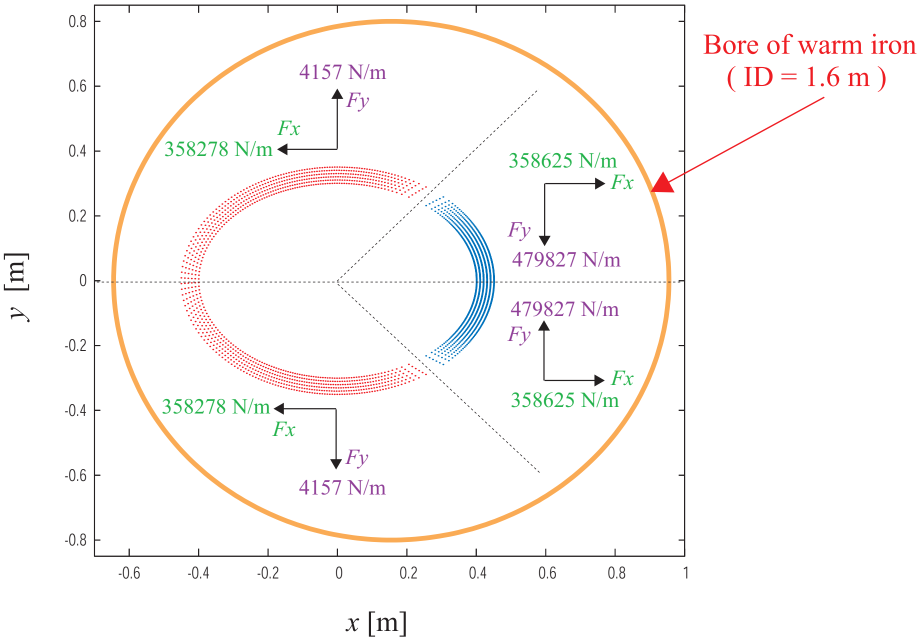

(a) Cross-section of the coil with warm iron yoke

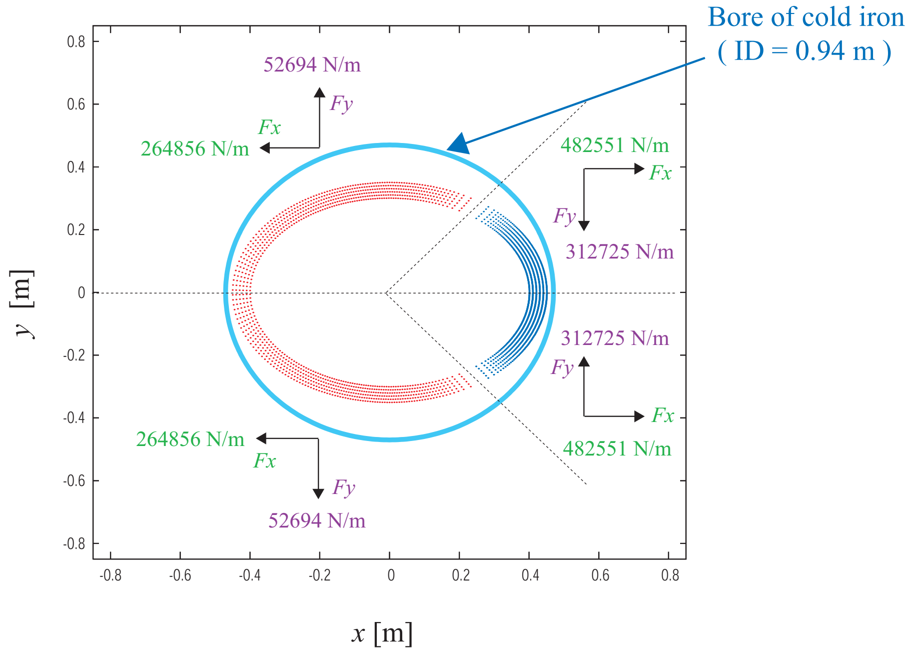

(b) Cross-section of the coil with cold iron yoke

Figure 33: Magnetic force for the magnet surrounded by each iron yoke

Table 11: Characteristics of materials

	Young's modulus [Pa]	Poisson's ratio
Conductor	1.08×10^{11}	0.328
SUS 304L	2.02×10^{11}	0.275
Epoxy resin	6.87×10^{9}	0.3
Iron yoke	2.11×10^{11}	0.293

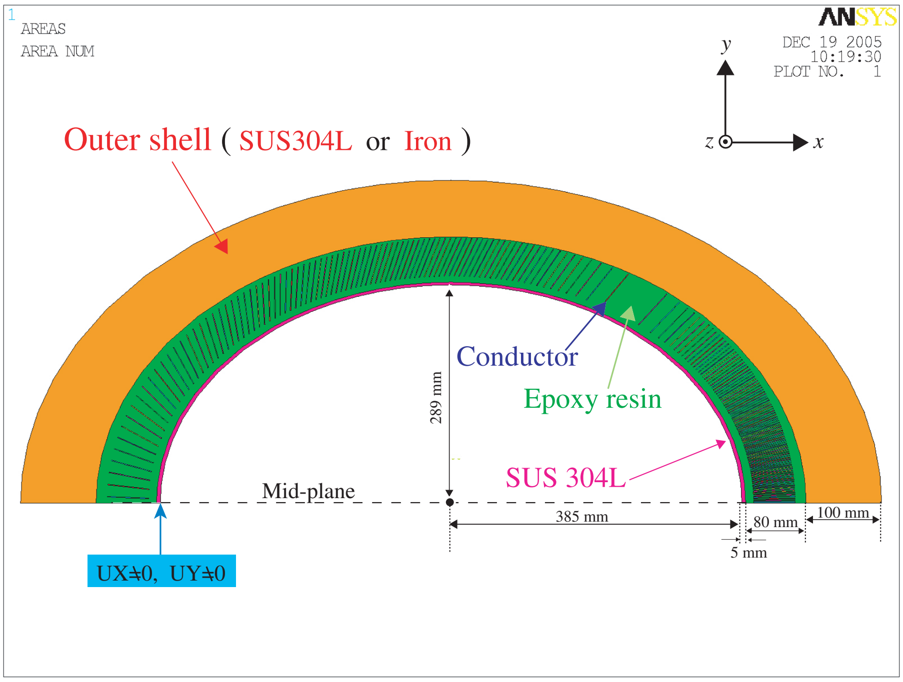

Figure 34: Cross-section of FEM model for the structural calculation

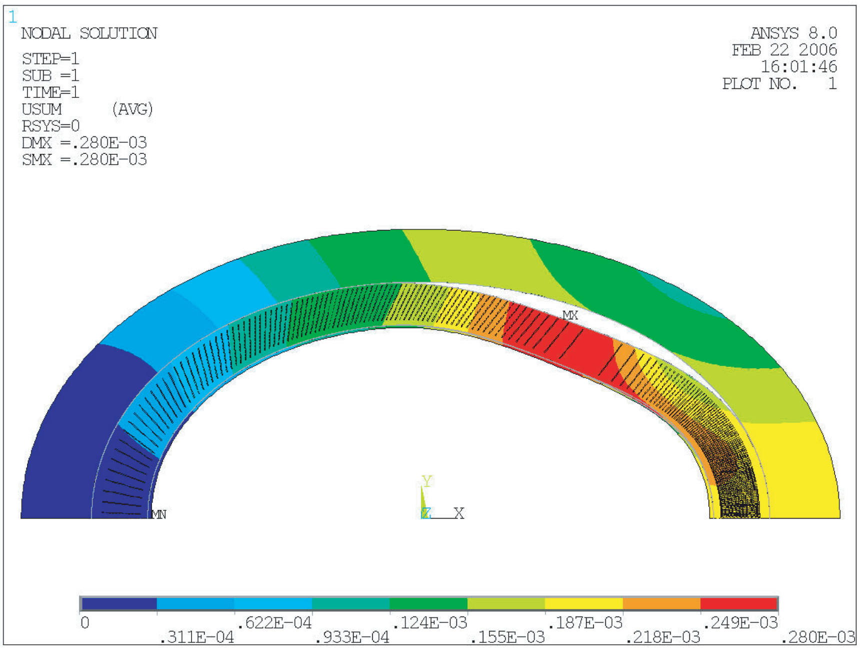

Figure 35: Distortion of the magnet surrounded by SUS304L, caused by magnetic force

confirmed that there is little difference in the maximum distortion between the magnet surrounded with the SUS304L and the magnet surrounded with the iron yoke, in the case that the magnetic field strength is about 1 T at the magnet center.

Furthermore, structural calculations of the magnet without the inner shell was carried out so as to understand its effect on the design. The above model, conditions and characteristics were used without the inner shell in this calculation. Conditions of constraint were therefore changed as follows: points on the mid-plane do not move in the vertical direction, in addition at one point the resin is attached on the mid-plane on the low magnetic field side and does not move in the horizontal direction. The distortion of the magnet without the inner shell is shown in Fig. 36 (b), the maximum distortion being about 0.5 mm. The maximum distortion does not increase unduly compared to that calculated with the inner shell. Consequently, the magnet without the inner shell could be considered as a candidate for the structural design. The maximum distortion could be reduced by adjusting the thickness of the iron yoke or the epoxy resin which impregnates the coil. The relation between the distortion and the field quality is described in Chapter 5.

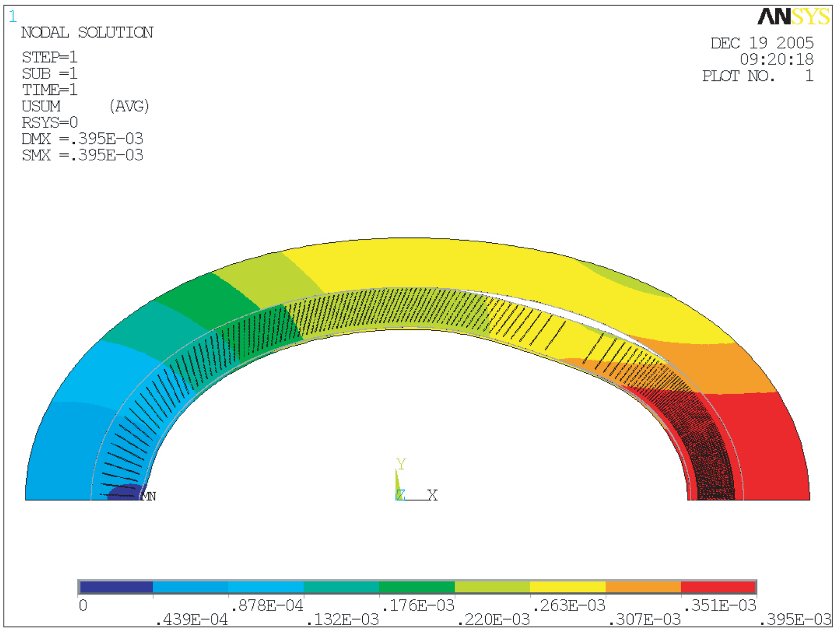

(a) Magnet surrounded by cold iron with inner shell

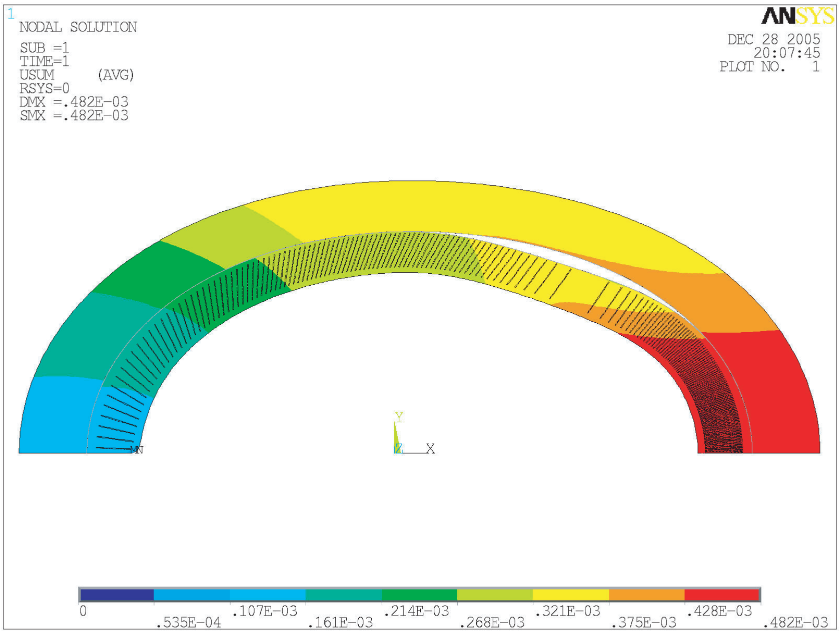

(b) Magnet surrounded by cold iron without inner shell

Figure 36: Distortion of the magnet surrounded by cold iron yoke, caused by the magnetic forces

2.10 Summary of Chapter 2

The study of the coil design for the superconducting FFAG magnet has been reported in this Chapter, in order to verify that the magnetic field required for the FFAG magnet can be realized by using a magnet which consists of a coil based on the $\cos(n\theta)$ current distribution. An original computer code for the design of the coil cross-section, which can generate a combined function magnetic field containing higher order harmonics by using one coil layer, has been developed for this study. A coil configuration with a left-right asymmetric cross-section and a large elliptical aperture has been designed using the developed computer code, such that the design requirement was fulfilled by using the coil to generate the desired integrated magnetic field along an arc orbit . It has been confirmed by particle tracking that particles circulate stably in the FFAG ring with a magnetic field map generated by the above coil configuration. In addition, it has been verified that the designed saddle shaped coil is suitable to be utilized for the FFAG magnet.

As the next step in the plan, the practical design of the superconducting FFAG magnet has been made taking into account the effect of the iron yoke on the magnetic field. The coil configuration surrounded with a yoke has been optimized to meet the design requirement in terms of the integrated magnetic field. The structural characteristics of the magnet have also been examined. As a result, it has been confirmed that the cold iron design is preferable, making the magnet physically more compact and providing better mechanical stability.

3 Development of the prototype superconducting coil

Magnetic design and cooling design of a prototype coil for the superconducting FFAG magnet were carried out. In addition, the prototype coil was fabricated based on the design.

3.1 Magnetic design

As the next step in the development of the superconducting coil of the FFAG magnet, a prototype was designed. A cylindrical configuration was adopted as the winding frame of the prototype, the design parameters of which are listed in Table 12. For practical reasons, a cylindrical geometry of circular cross-section was adopted for this first prototype. The prototype coil consists of a 2-layer double pancake winding. Specific features of the prototype coil are left-right asymmetry of the cross-section, and its large aperture.

The coil configuration was designed to fulfill the design requirement in terms of BL, which is the integrated magnetic field along an arc orbit in the beam excursion region. The calculated result of the *local* $k+1$ obtained from the BL is shown in Fig. 37; this result satisfies the design requirements of beam optics. Figures 38, 39 and 40 show the designed coil configuration.

3.2 Cooling design

A conduction cooling system was adopted for the prototype coil to examine the feasibility of this cooling method for the superconducting FFAG magnet. In order to cool the prototype coil using conduction cooling, twenty-eight cooling plates are glued to the second layer of the prototype coil at regular intervals in the longitudinal direction. The strip shape was adopted for the cooling plate to prevent eddy-current loss at excitation. The parameters of the cooling plates, which are made of pure aluminum strip, are listed in Table 13. The thermal conductivity of the pure-Al is shown in Fig. 41 [20].

One end of the pure-Al strip placed in the longitudinal direction of the coil is cooled in this system. Heat flow is therefore different in each direction as shown in Fig. 42. In the longitudinal direction, heat flows mainly along

Table 12: Design parameters of the prototype coil

Number of layers	2
Number of turn for 1 layer	120
Type of coil configuration	Saddle shaped coil
Field index, k	10
Coil winding	Double pancake
Position of the conductors in 1st layer from the center of coil	448.45 mm
Position of the conductors in 2nd layer from the center of coil	449.60 mm
Diameter of the conductor	0.9 mm
Radius of curvature at coil end	30 mm
Distance between conductors at coil end	2 mm
Length of coil	552.16 mm
Superconducting wire	
Material	NbTi/Cu
Diameter of wire	0.9 mm
Cu/Sc ratio	2.7
Cu RRR	200

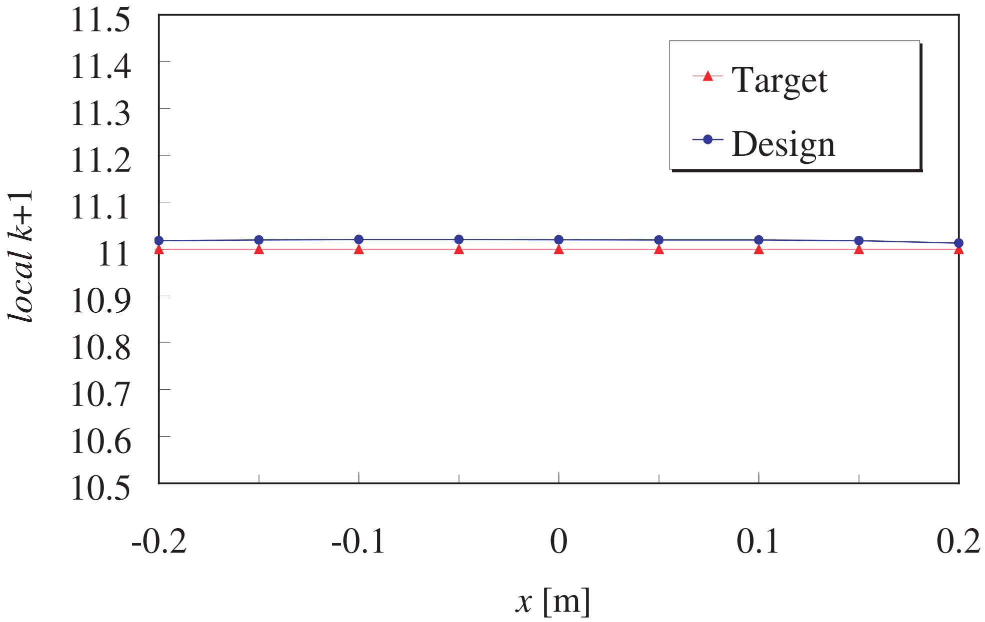

Figure 37: *local* $k+1$ of the designed prototype coil

the pure-Al strip when the temperature of the coil is about 4 K, because the thermal conductivity of the prototype coil, which contains a lot of epoxy, is about 10^5 orders of magnitude less than that of the pure-Al strip [21]. In the circumferential and radial directions, the path of heat is without the pure-Al strip. Consequently, heat generated in the coil is mainly absorbed in the longitudinal direction.

The prototype coil is cooled via the pure-Al strips attached to the pipe in which the refrigerant flows. A temperature difference between coil ends in the longitudinal direction therefore occurs when the heat is generated in the end which is far from the pipe. In order to investigate the temperature difference between coil ends for each heat input, the temperature difference was obtained by means of the Fourier law of heat conduction with the design parameters and the following assumptions:

· Thermal conductivity is constant. (Temperature differences are small.)

· Thermal conductivity of the pure-Al strip is 4000 W/(m·K), and that of the coil without the strip is 0.03 W/(m·K).

· The effective thermal conductivity, λ, of the coil attached to the pure-Al strip, taking into account the cross-sectional area ratio in the straight section,

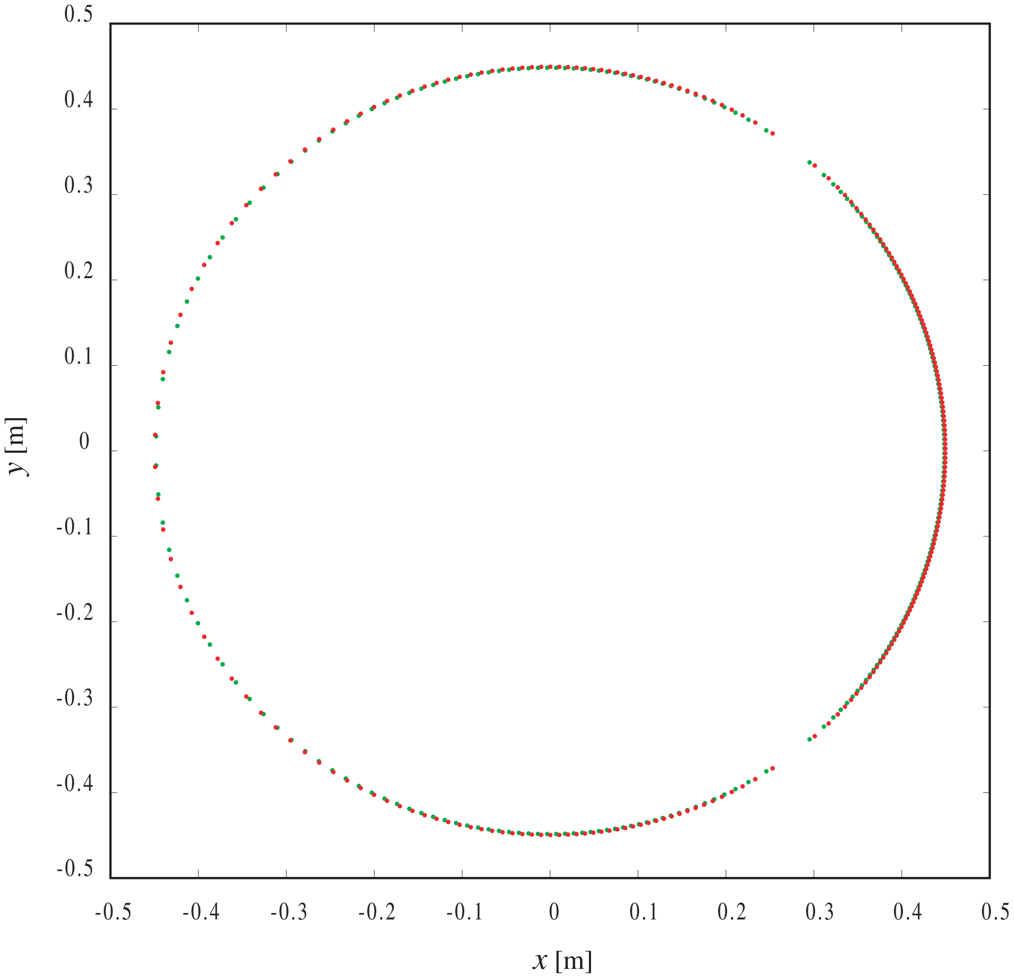

Figure 38: Coil configuration of the prototype in x-y plane: the green points show the conductor position of the 1st layer, the red points show the conductor position of the 2nd layer

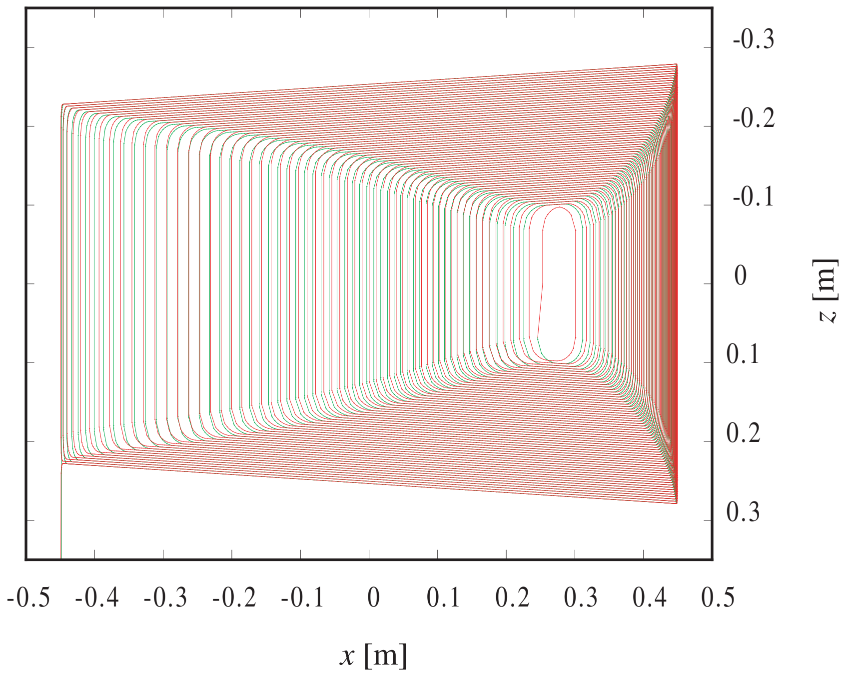

Figure 39: Coil configuration of the prototype in x-z plane

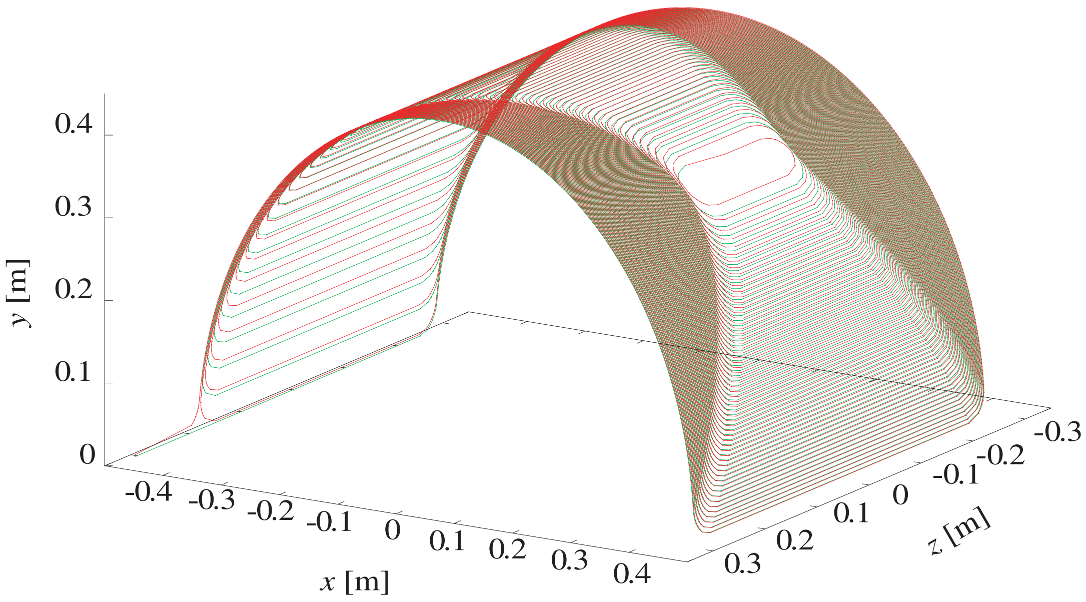

Figure 40: Coil configuration of the prototype in perspective

is defined as

$$\lambda = \lambda_{Al} \times \frac{S_{Al}}{S_{total}} + \lambda_{coil} \times \frac{S_{coil}}{S_{total}} \tag{18}$$

where λ_{Al} is the thermal conductivity of the pure-Al strip, λ_{coil} is that of the coil without the pure-Al strip, S_{total} is the cross-section area of the coil with the strips in longitudinal direction, S_{Al} is that of the strips in the longitudinal direction, and S_{coil} is that of the coil without the strips in the longitudinal direction. The effective thermal conductivity is 232 W/(m·K).

· Heat flows only one direction.

Figure 43 illustrates the equivalent thermal resistance circuits, which include the thermal resistance of the pipe and top board etc. as well as that of the prototype coil with pure-Al strips, in the longitudinal direction between the coil and the liquid helium. In the case that uniform heat input to the coil end which is far from the pipe is 1 W, the temperature difference is about 0.3 K in the coil, based on the thermal resistance circuit shown in Fig. 43 (a). A large difference in temperature between coil ends is unlikely to occur. The area of the pure-Al strips is 6 % of the total cross-section of the coil, and the pure-Al strips have a strong influence on the thermal conductance in the longitudinal direction. In addition, if the pure-Al strips were to be glued not only on the outside the coil but also on the inside, the thermal conductivity would be doubled.

In order to take into account a more likely situation, the case of local heat generation in the coil was studied. It was assumed that the local heat flows only longitudinally in a part of the coil where one pure-Al strip was attached, and the effective thermal conductivity is 279 W/(m·K) with the above assumption. When 1 W is applied locally in one part of the coil end, the maximum total temperature difference between coil ends is about 7.7 K, based on the thermal resistance circuit shown in Fig. 43 (b). The temperature difference is also about 7.7 K in the case the heat flows only in one pure-Al strip, because pure-Al strip is thin (0.21 mm), even though the thermal conductivity of the pure-Al strip is about 4000 W/(m·K) around 4 K. It can therefore be assumed that the heat flows not in the coil but only in the pure-Al strip.

In the above cooling design, it was supposed that the thermal path is only in one direction and the thermal conductivity of the conductor was not taken into consideration. This gave rise to the relatively large temperature difference for some situations. In reality, the heat flows in three directions and the thermal conductivity is moderately influenced by the conductor, so that it can be assumed that the temperature difference will be reduced compared to the results of this estimation.

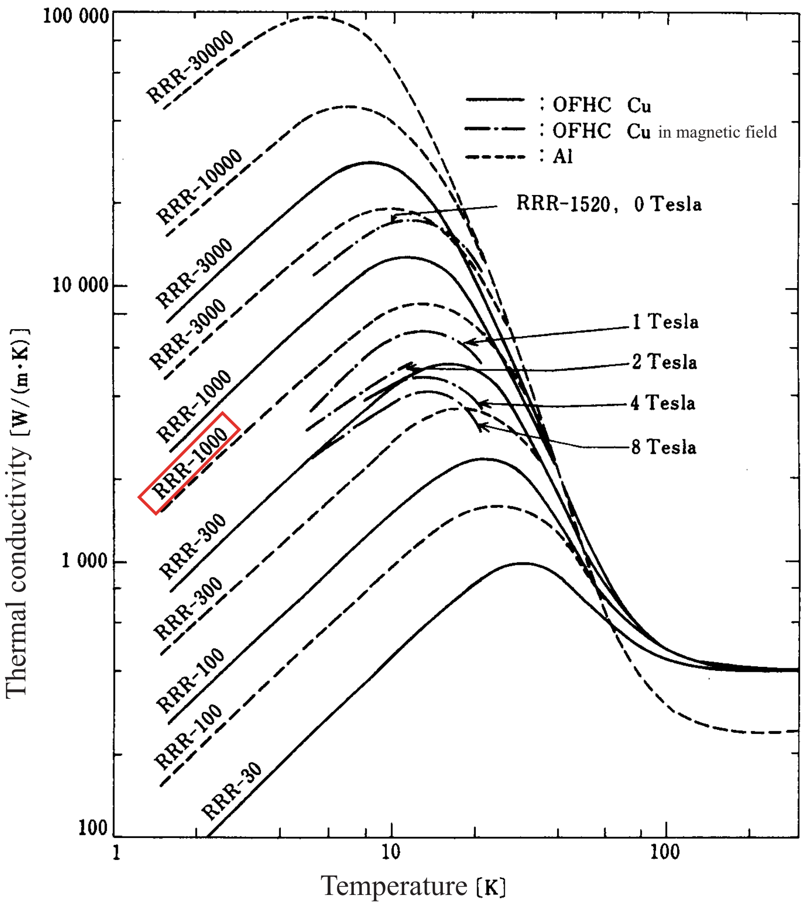

Figure 41: Thermal conductivity of pure aluminum

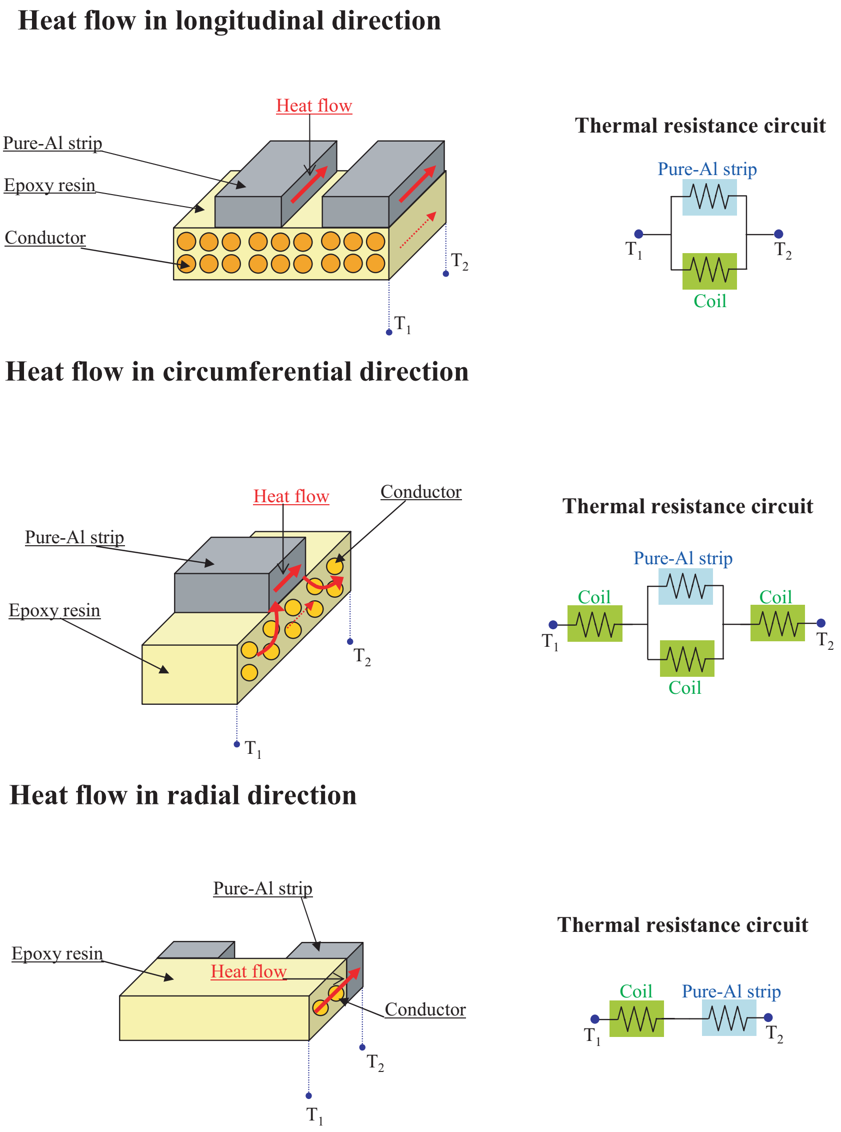

Figure 42: Thermal path of the prototype coil for each direction

Table 13: Pure-Al strips for conduction cooling

Material	Pure Al
Width	85 mm
Thickness	0.21 mm
Length	1400 mm
RRR	1000∼
Thermal conductivity	
	∼4000 W/(m·K) at 4 K
	∼6000 W/(m·K) at 6 K
	∼7000 W/(m·K) at 8 K
	∼8000 W/(m·K) at 10 K

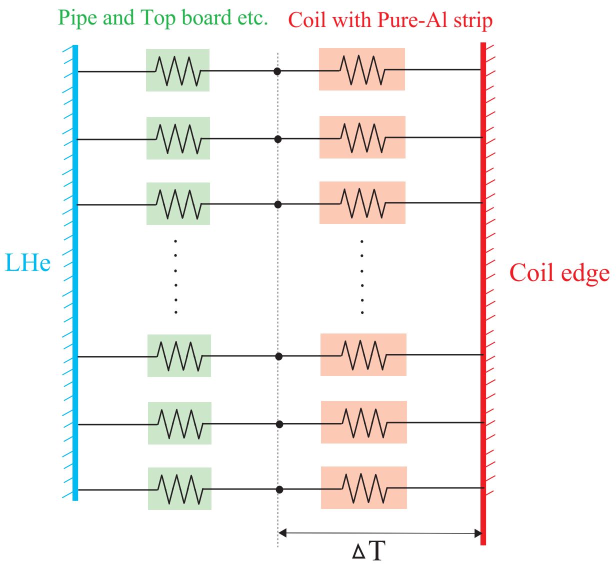

(a) Thermal resistance circuit for all pure-Al strips

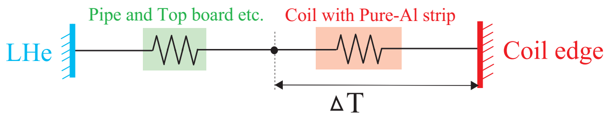

(b) Thermal resistance circuit for one pure-Al strip

Figure 43: Thermal resistance circuits

Table 14: Characteristics of the prototype coil

Resistance	17.63 Ω
Inductance	3.69 mH at 100Hz

3.3 Fabrication

The prototype coil was wound by using a CNC winding machine that was developed for this study in an academic research collaboration with TOSHIBA Co., Ltd.. This machine has 6 axes in order to make it possible to wind on cylinders of elliptic as well as circular cross-section. Figure 44 shows winding practice with an elliptic cylindrical winding frame. The CNC winding machine functions by accurately placing superconducting wire directly on an insulated mandrel with adhesive that is melted by using an ultrasonic heater as shown in Fig. 45. The adhesive is pre-painted on the insulation film and the wire. Hence, the coil can be wound precisely by using the winding machine. Figure 46 shows the fabrication process of the first layer. After the first layer of the coil was wound as shown in Fig. 47, the gaps between turns were filled with epoxy resin and were covered with an insulation sheet. The second layer was wound on the insulation sheet and the gaps between turns were also filled with epoxy resin. It was observed that coil surface was not smooth, the maximum asperity being about 1mm. After that, the second layer was covered with an insulation sheet. Twenty-eight pure-Al strips were glued on the insulation sheet in the longitudinal direction at regular intervals as shown in Fig. 48, and structural shells made of aluminium alloy were attached to the outer surface of the coil. Figure 49 shows a picture of the developed prototype coil. Some characteristics of the prototype are listed in Table 14.

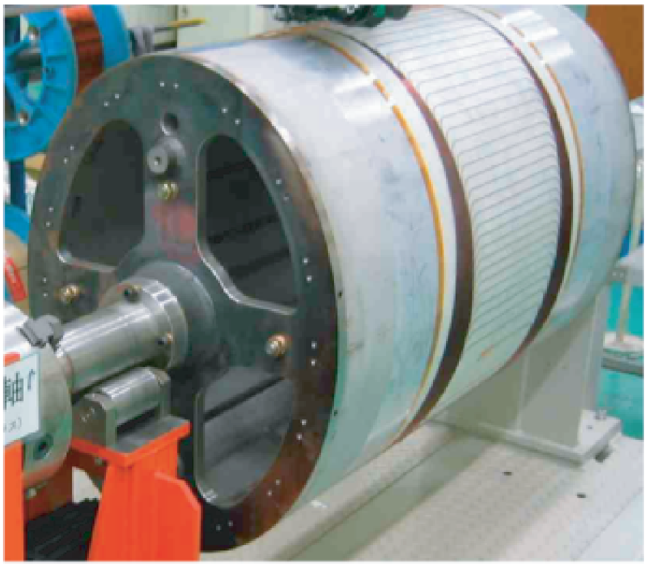

Figure 44: Winding practice with an elliptic cylindrical winding frame

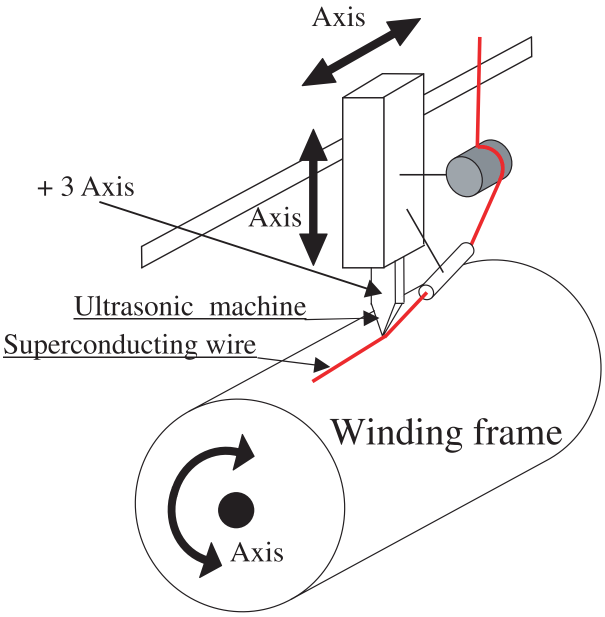

Figure 45: Schematic view of winding machine

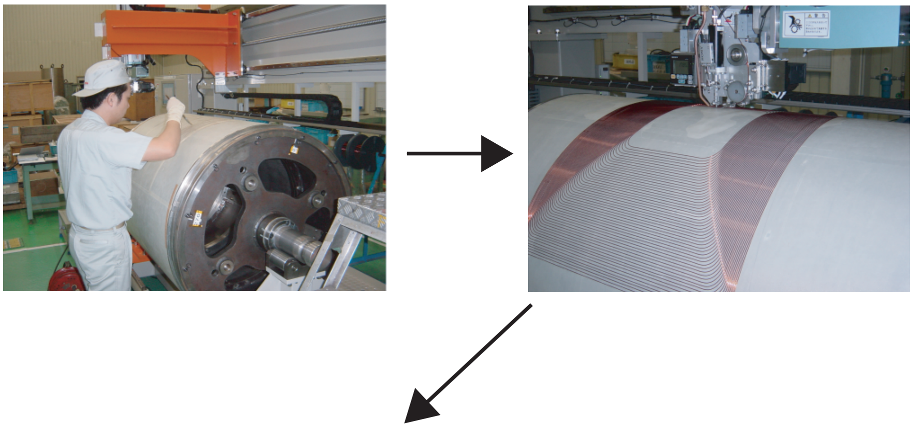

1. Apply thermoplastic adhesive on insulation

2. Wind a coil with the CNC winding machine

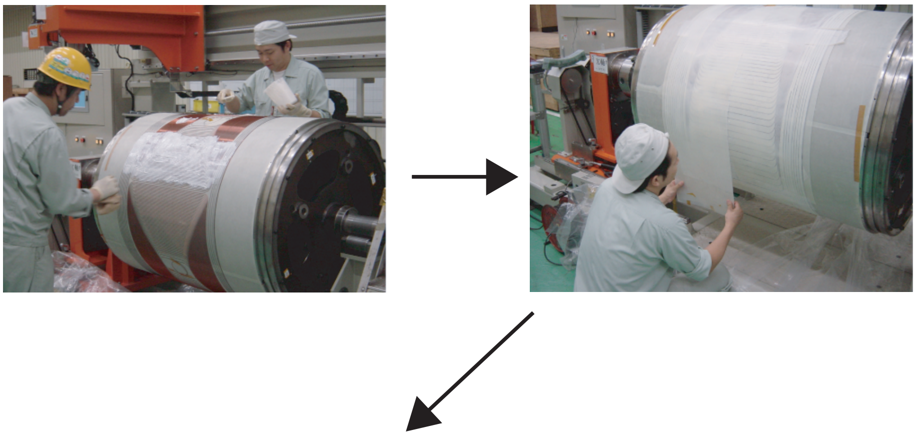

3. Fill up gaps between turns with epoxy resin

4. Cover a layer with an insulation sheet

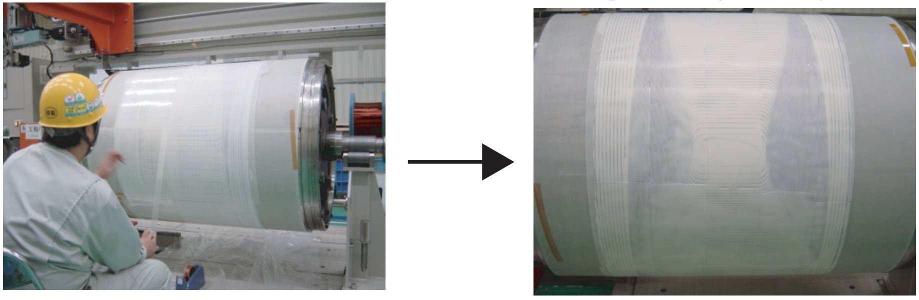

5. Reshape with heat-shrinking tape

6. Complete a single coil layer

Figure 46: Fabrication process

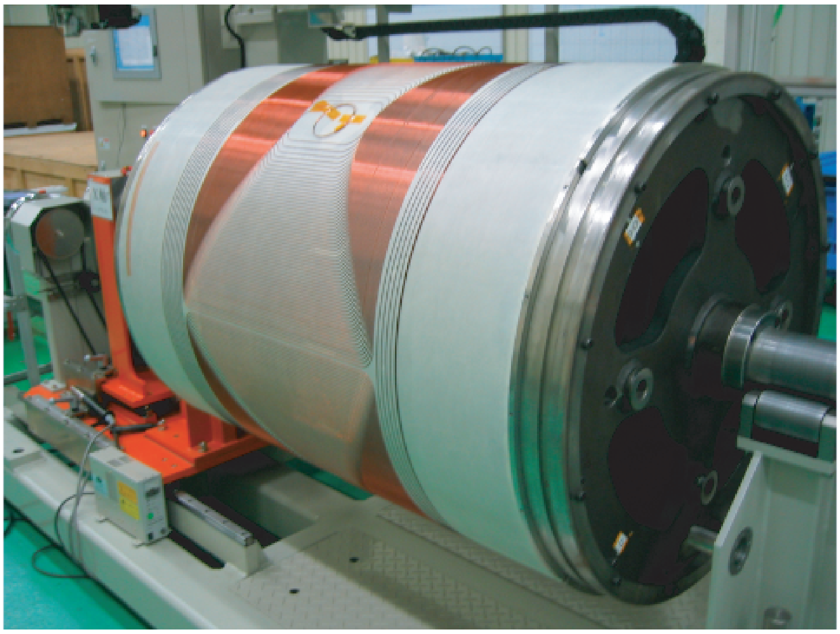

Figure 47: First layer of the prototype coil

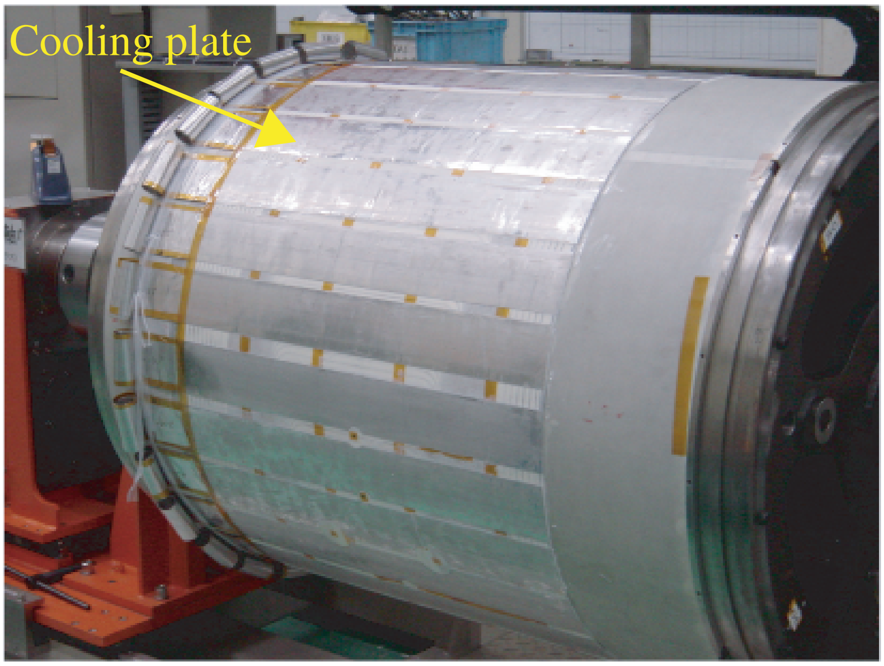

Figure 48: Cooling plates equipped on the coil

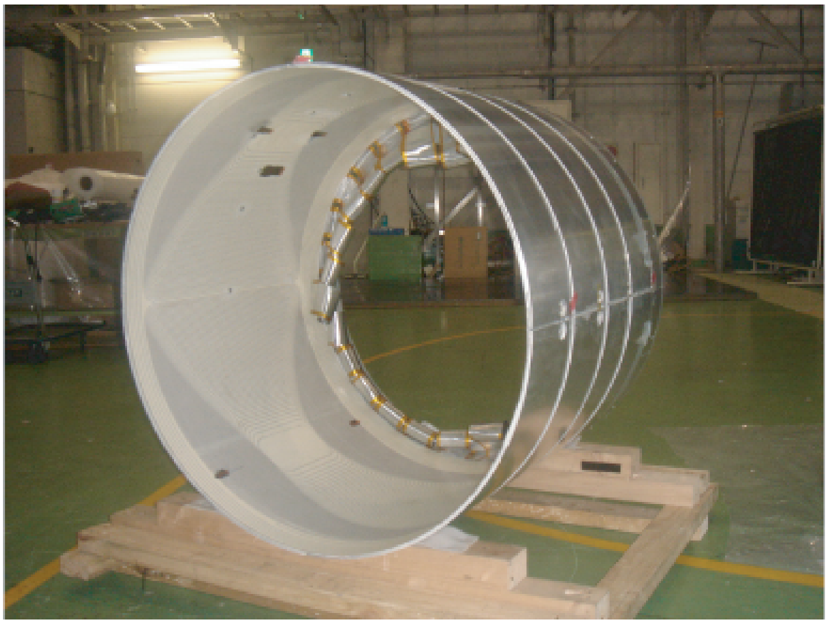

Figure 49: Developed prototype coil

3.4 Summary of Chapter 3

A prototype coil has been developed as the following step in the realization of the superconducting FFAG magnet. In the magnetic design, the prototype which consists of 2 layers with a cylindrical aperture was made so as to fulfill the design requirement on the integrated magnetic field. In the cooling design, conduction cooling via pure-Al strips attached in the longitudinal direction was adopted to cool the prototype coil. Based on the design, the prototype was fabricated by using a 6 axis CNC winding machine equipped with an ultrasonic transducer.

4 Experimental study with the prototype coil

4.1 Measurement of the magnetic field at room temperature

Magnetic field measurements were performed on the prototype coil at room temperature in order to verify that it can deliver the required magnetic field.

4.1.1 Apparatus for warm measurement

A schematic view of the apparatus for the field measurement is shown in Fig. 50. The magnetic field generated by the prototype coil was measured by using a Hall probe mounted on a triaxial stand. To prevent excessive temperature rise in the coil during excitation, air ventilation was made by using a fan. The characteristics of the instrumentation for the field measurement are listed in Table 15.

4.1.2 Measurement condition and method

The region over which the magnetic field was measured is given in Table 16. The measurement was carried out not only within the coil but also outside in order to examine the fringe field. A maximum excitation current of 2.4 A was used in this test.

The prototype coil can only generate a magnetic field of a few gauss on the mid-plane at room temperature, because of the limited excitation current and the large aperture. In order to measure the low magnetic field precisely, taking into account the effect of the ambient field, measurements were made for each current value as shown in Fig. 51, and the measurement was corrected with the method of least squares.

4.1.3 Results

The vertical magnetic fields generated by the prototype coil were measured at room temperature. The normalized vertical magnetic field distributions on the mid-plane along the z-axis for each position on the x-axis is shown in Fig. 52. Figure 53 shows the magnetic field distributions on the mid-plane along the x-axis for each position on the z-axis. The measured magnetic fields are normalized by the vertical magnetic field strength on the mid-plane at the coil center.

Table 15: Instrumentation for the field measurement

Triaxial stand	
resolution	1 mm
Accuracy	±0.3 mm
Gauss meter (F.W BELL SERIES 9900)	
resolution	1 mG
Accuracy	±0.05% of reading ±0.014 Gauss
Power supply (EPS BWS 40-15)	
Current	$0 \sim \pm$ 15 A
Voltage	$0 \sim \pm$ 40 V
Digital multimeter (KEITHLEY 2010 MULTIMETER)	
resolution	100 μV (Range 100 V)
Accuracy	±0.001 % of reading

Table 16: Region of the measurement

Axis	Range
x	-300 mm $\sim$ 300 mm
y	-10 mm $\sim$ 10 mm
z	-700 mm $\sim$ 700 mm

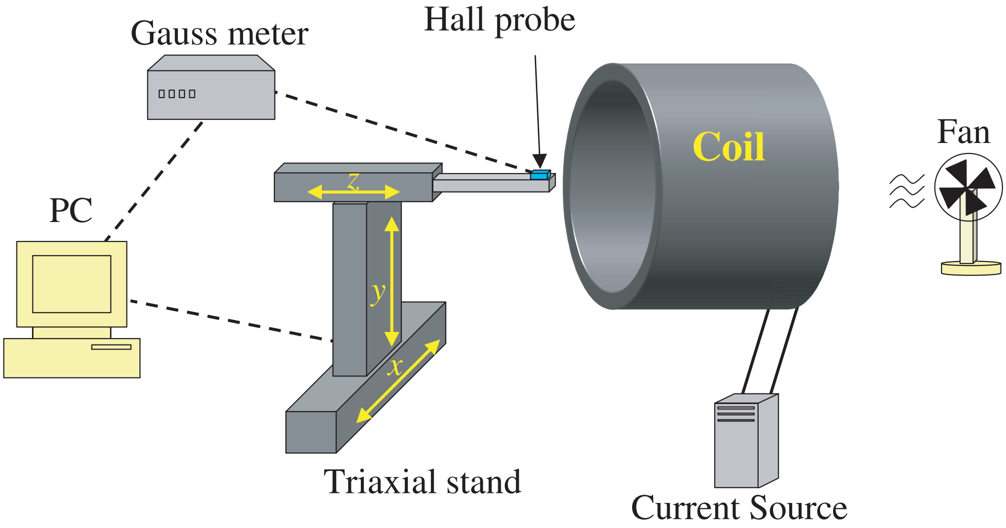

Figure 50: Schematic view of apparatus for warm field measurement

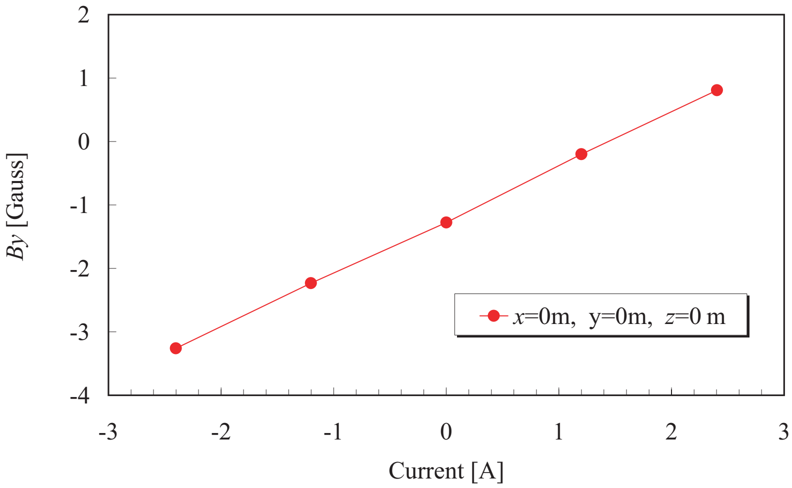

Figure 51: Magnetic field for each current at coil center on the mid-plane

From the results, it can be seen that the measurements are in general agreement with the calculations. Some difference between the measurement and the calculation was however observed. We discuss the results further in Chapter 5.

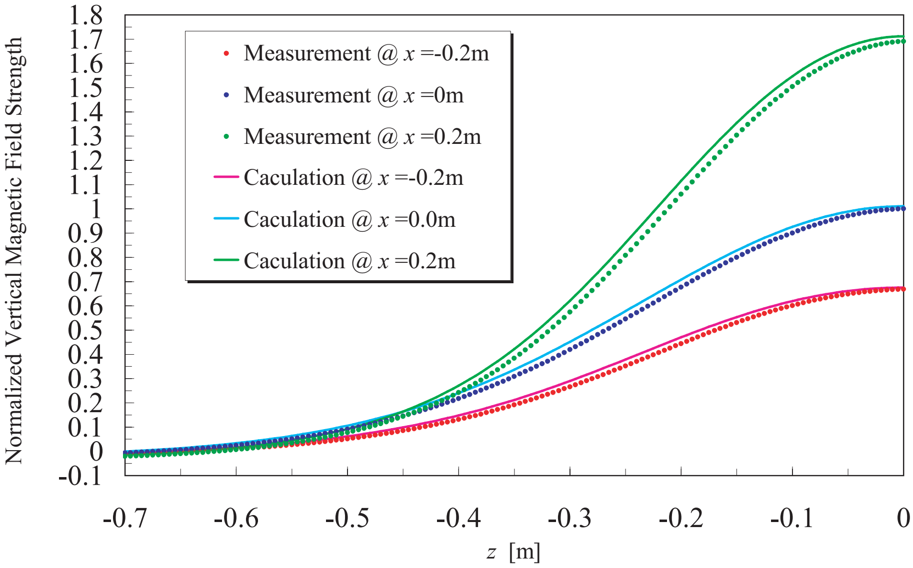

(a) Return end side

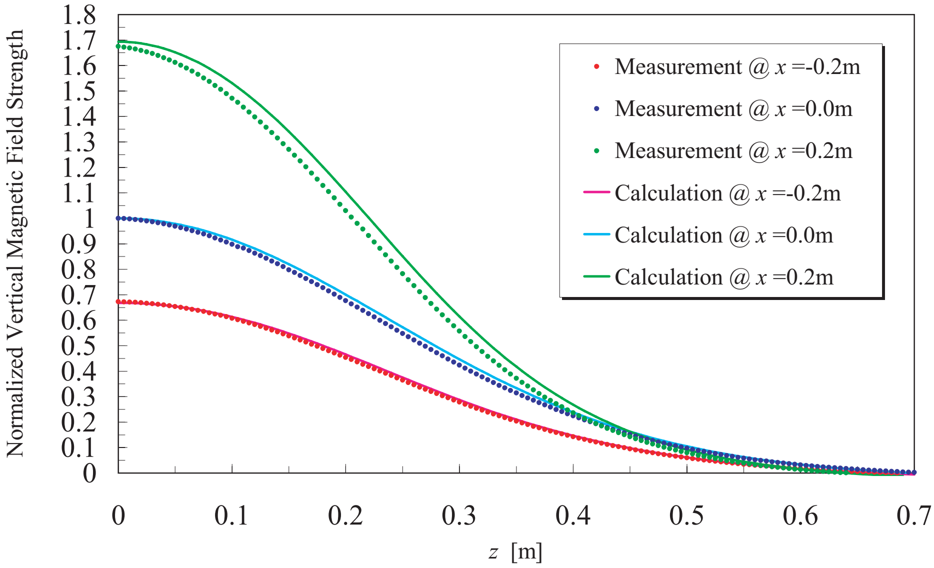

(b) Lead end side

Figure 52: Vertical magnetic field distributions on mid-plane along the z-axis for each position on the x-axis

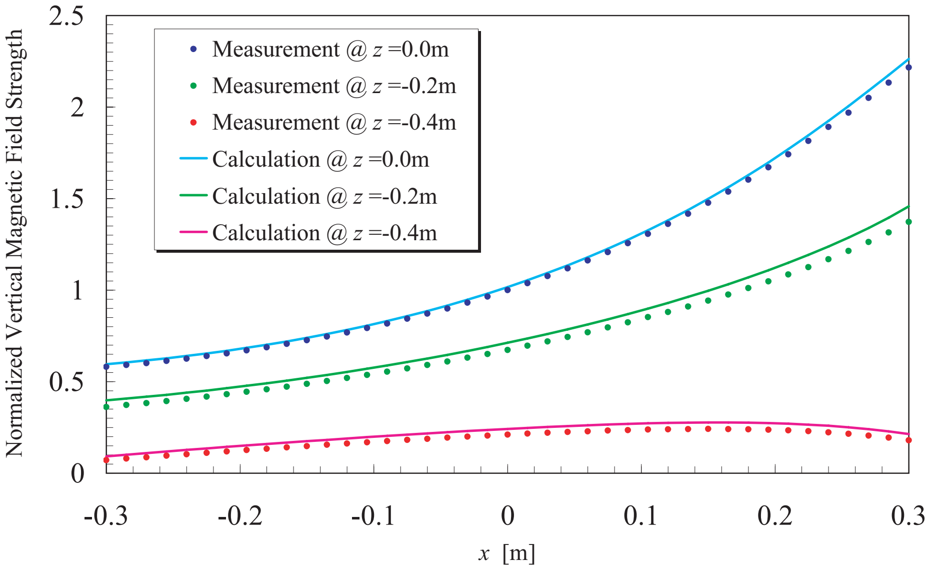

(a) Return end side

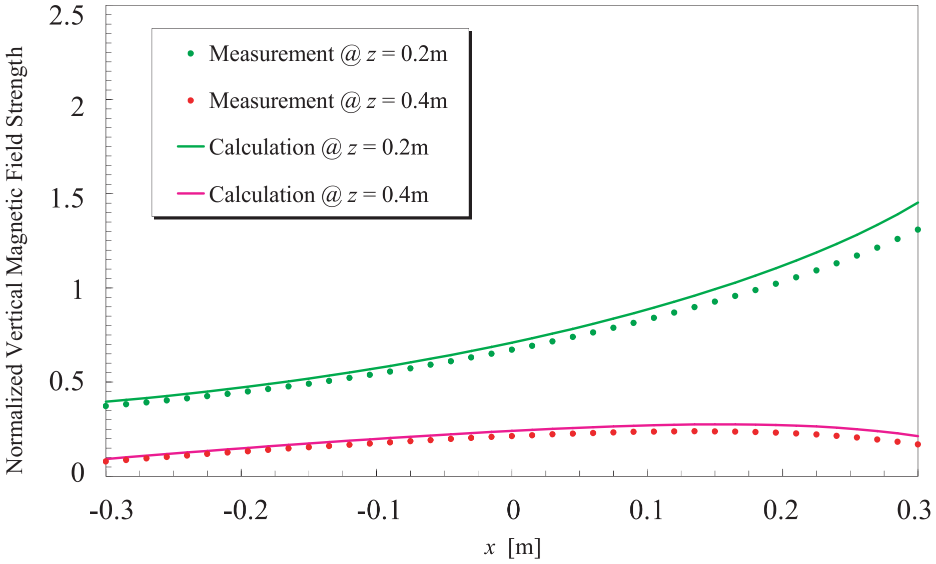

(b) Lead end side

Figure 53: Vertical magnetic field distributions on mid-plane along the x-axis for each position on the z-axis

4.2 Cooldown and Cold measurement

A conduction cooling system was proposed for the superconducting FFAG magnet. As pipes can be used for refrigerant with conduction cooling, such a system can be simple and compact. On the other hand, conduction cooling cannot absorb heat uniformly from a whole coil. As a result, a temperature gradient occurs when heat is generated in the coil, and the stability of the coil in operation is therefore a concern. The prototype coil with its conduction cooling was therefore cooled down and heat was applied in order to determine the cooling and the thermal characteristics of the saddle shaped coil with the left-right asymmetric cross-section cooled by conduction. This measurement result of the prototype coil provides fundamental input data for the design of a multilayer saddle shaped coil with conduction cooling.

4.2.1 Conduction cooling system

The cryostat in which the prototype coil was cooled consists of a vacuum vessel with thermal shields, multilayer insulation and pipes for refrigeration, a reservoir tank, etc. [22]. Figure 54 shows the schematic view of the conduction cooling system used for the cold measurements; the dimensions of the cryostat are given in Fig. 55. The prototype coil was suspended in the vertical position as shown in Fig. 56. Cryogen contained in a reservoir tank flows in the pipe to cool the coil, the top board and thermal shields etc. in the cryostat. The coil was cooled via cooling plates which were attached to the pipe in which the refrigerant flows as shown in Fig. 57. The refrigerant returns to the reservoir tank after cooling the coil: the liquid stays in the tank, gas which is produced during the cooling of the coil is used for cooling the thermal shields. The thermal shield for the prototype coil is shown in Fig. 58.

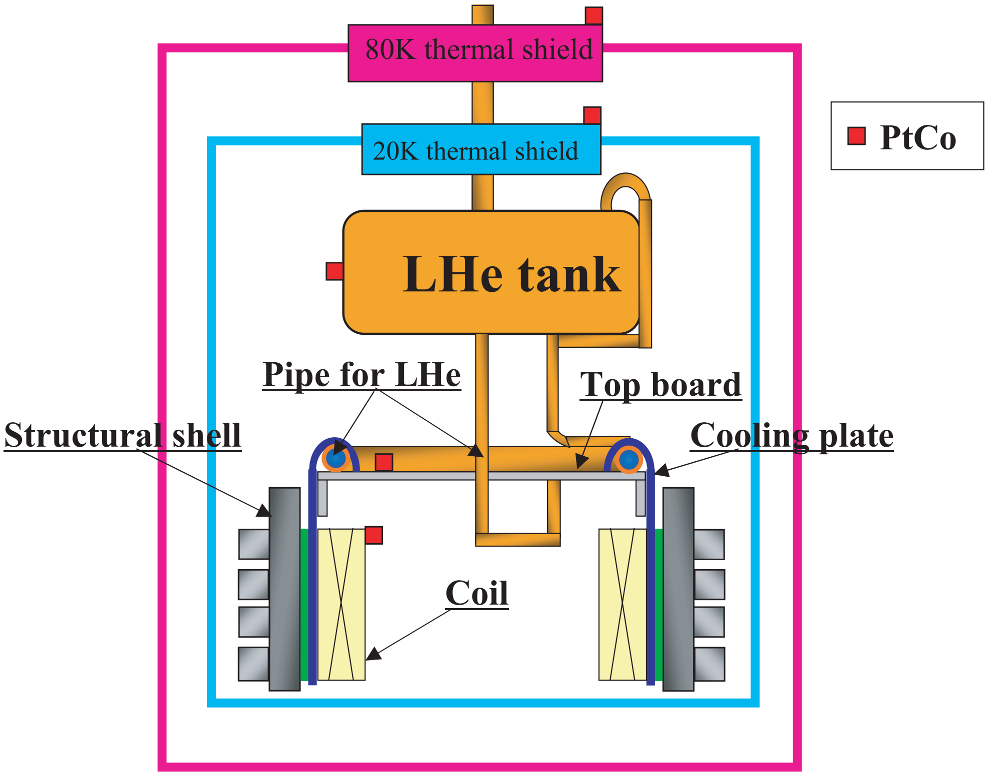

Figure 54: Schematic view of the cooling system

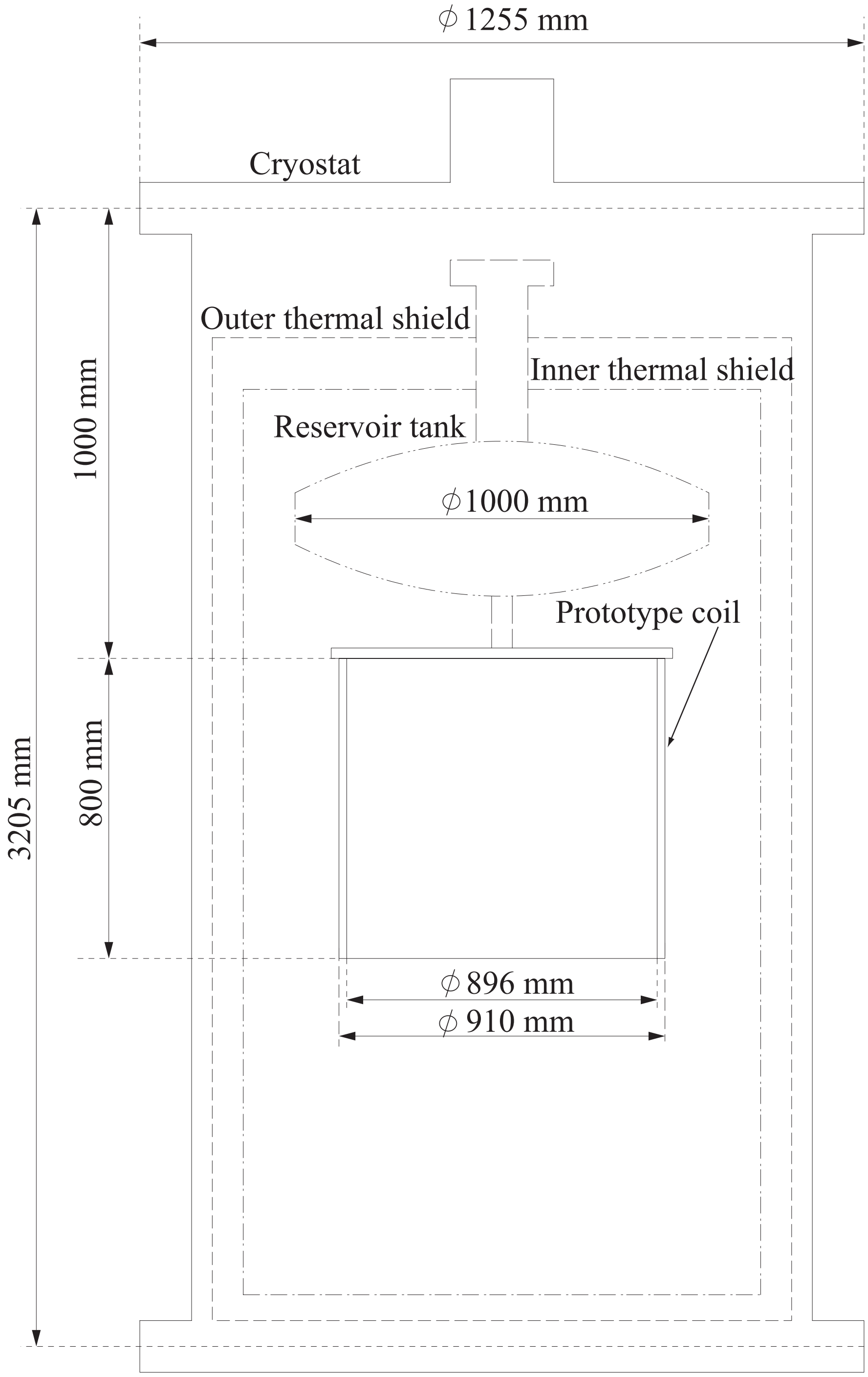

Figure 55: Dimensions of the cryostat

Figure 56: Prototype coil suspended in vertical position

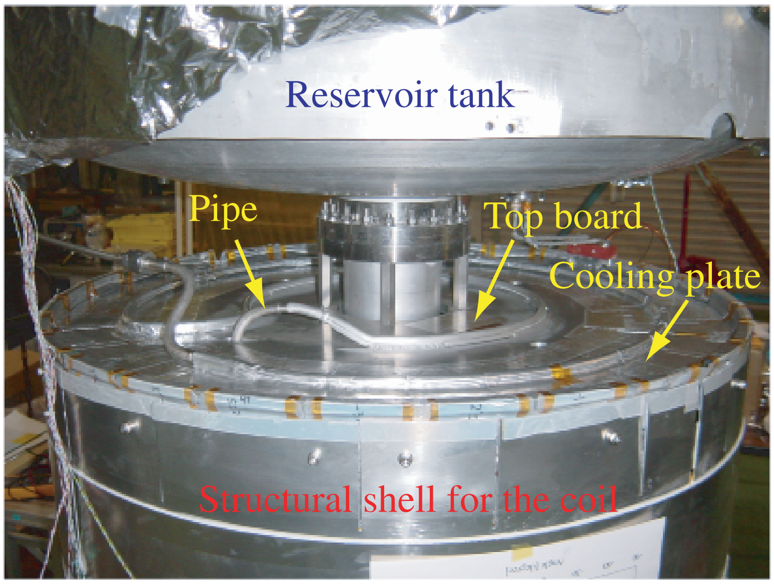

Figure 57: Cooling plates equipped on the pipe in which LHe flows

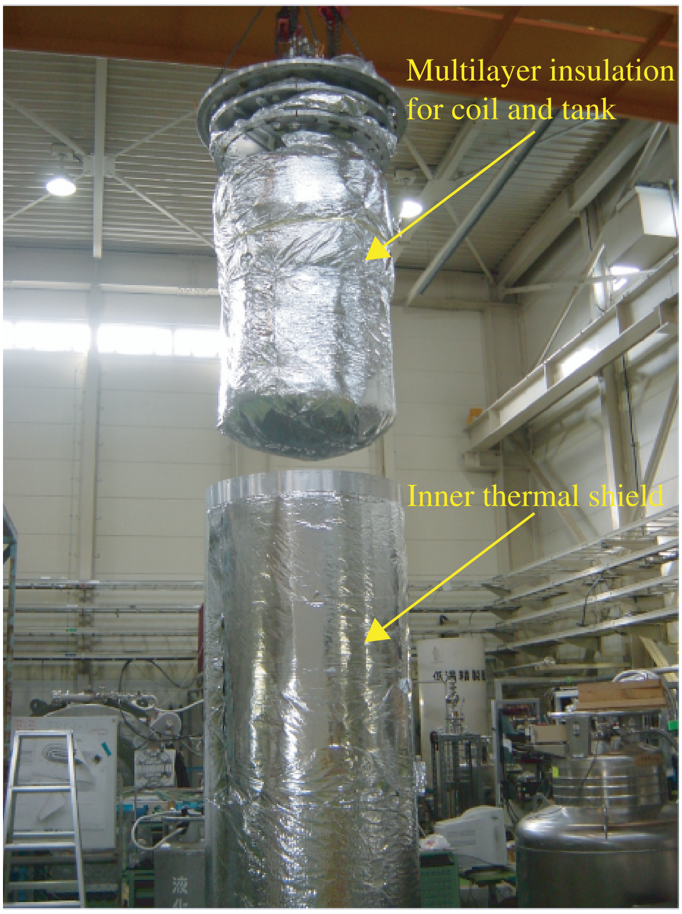

Figure 58: Thermal shield for prototype coil and reservoir tank

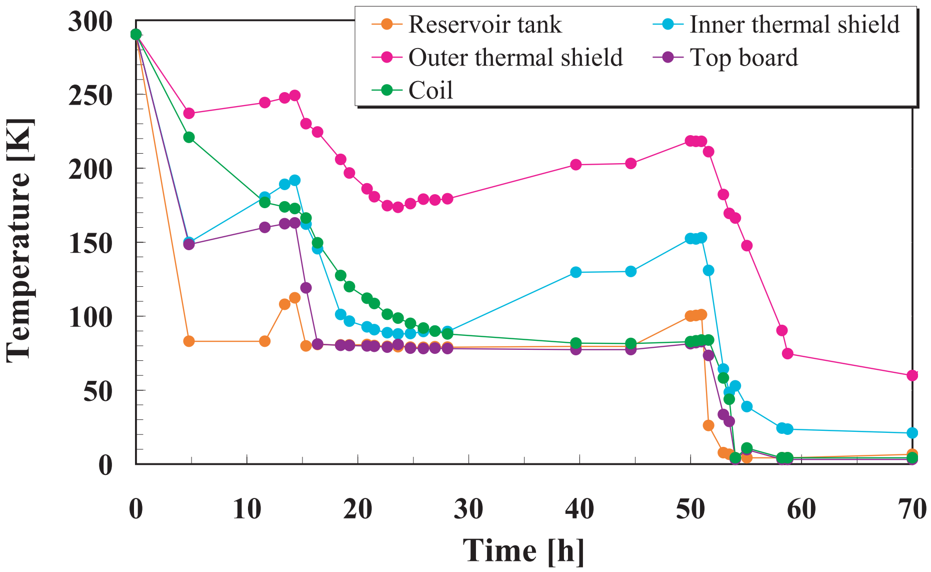

Figure 59: Temperature in the cryostat during cooldown

4.2.2 Cooling characteristics

Insulation vacuum in the cryostat was provided with a turbo-molecular pump. The pressure was reduced to about 1.0×10^{-3} torr before the prototype coil was cooled. After that, the reservoir tank and pipes were flushed with dry nitrogen gas to get rid of air. The initial cooling was made using LN_2 was used as refrigerant, until the temperature of the coil reached about 80 K. Because the latent heat of the LN_2 is greater than that of LHe, the coil can be cooled effectively by using LN_2 initially. Before the coil was cooled by using LHe, the reservoir tank and pipes were flushed with helium gas to get rid of nitrogen. Finally, the coil was cooled by using LHe, and the temperature of the coil reached about 4 K. The temperature of the inner and the outer thermal shield stabilized at about 20 K and 60 K, respectively. The vacuum pressure then went down to about 6.0×10^{-5} torr because of cryocooling.

Figure 59 shows the temperature at some positions in the cryostat during cooldown. The temperature rise at around 50 hours was due to the gas flushing procedure. The electrical resistance of the prototype coil when the coil was cooled from room temperature to about 4 K is shown in Fig. 60. The electrical resistance became zero after about 55 hours, with the coil reaching the superconducting state.

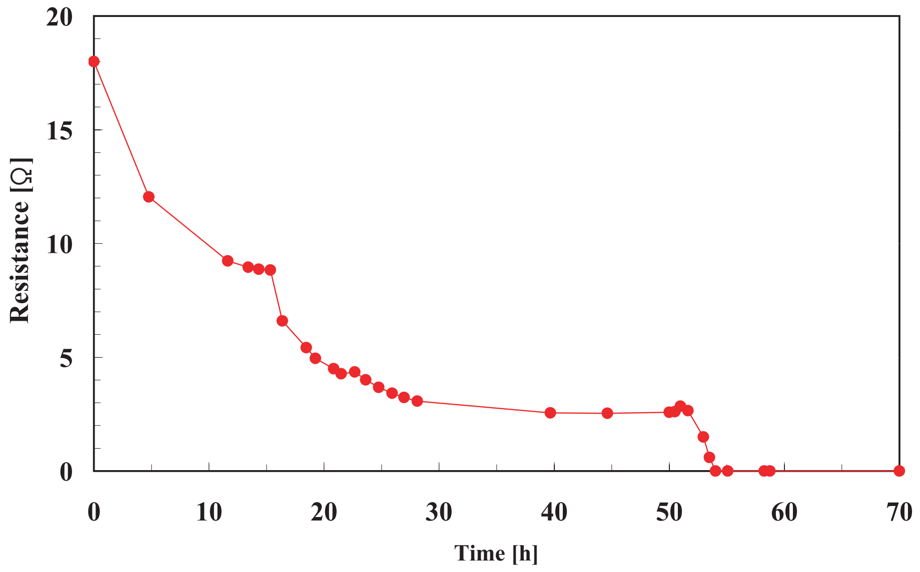

Figure 60: Electrical resistance of the coil during cooldown

4.2.3 Apparatus

Thermometers and heaters used in cooldown or measurement are listed in Table 17 and Table 18, and the photo of the thermometers is shown in Fig. 61. Pt-Co thermometers (PtCo) were used to monitor the temperature of some positions in the cryostat during cooldown, and a Cernox sensor was used to measure the temperature of the coil during heat input. The Cernox sensor and heaters used in the measurement were glued to the insulation sheet that forms the inner layer of the coil. Their positions on the coil are shown in Figs. 62 and 63. The Cernox sensor and heaters were located in the space between the cooling plates to eliminate the effect of the cooling plates on the measurement.

4.2.4 Thermal characteristics

In order to investigate the thermal characteristics of the conduction-cooled prototype coil, the temperature of the coil was measured when constant heat was applied locally by means of the heaters. The temperature of the coil was about 4.4 K before heat was applied. The conditions of the measurement were as follows:

(Condition 1) Heat input by using Heater-1

(Condition 2) Heat input by using Heater-2

Table 17: Lists of the thermometers

Position	Model number
Coil	Cernox X38995
Inner shield	PtCo 52-177L
Outer shield	PtCo 52-178L
Top board	PtCo 52-180L
Coil	PtCo 52-184L

Table 18: Lists of the heaters

Position	Model number	Resistance[Ω]	Size [mm]
Heater-1	MINCO HK913H	15	15× 48
Heater-2	MINCO HK913G	5.5	19× 48
Heater-3	MINCO HK913N	120	25× 76
Heater-4	MINCO HK913P	60	15× 76

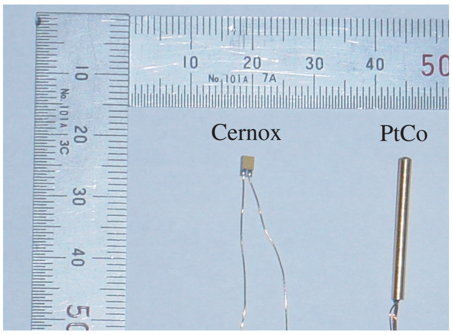

Figure 61: Photo of the thermometers

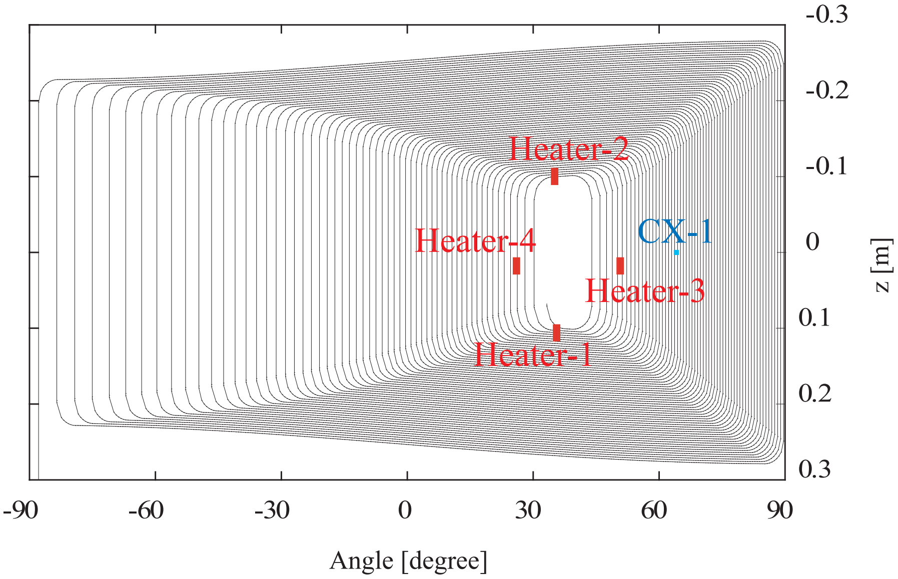

Figure 62: Positions of Cernox and PtCo on the coil

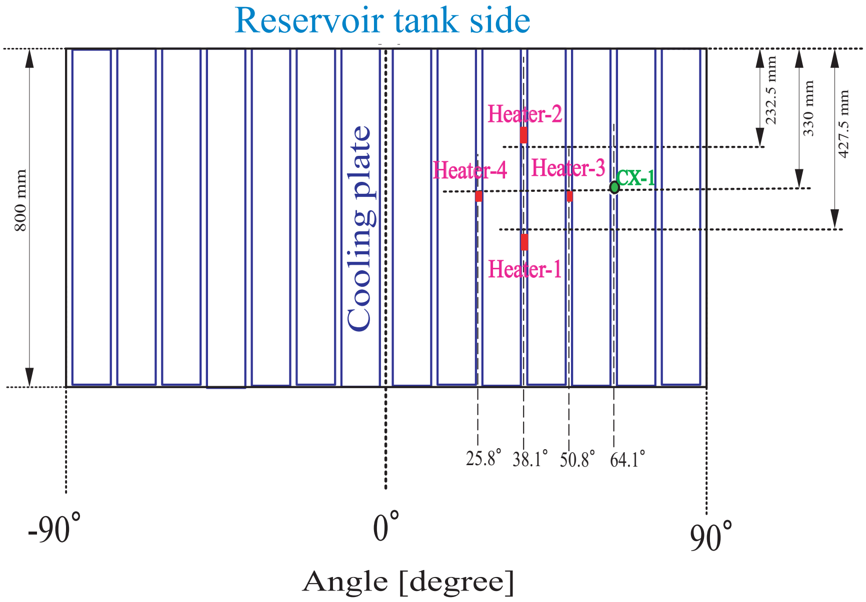

Figure 63: Positions of cooling plates, Cernox and heaters

(Condition 3) Heat input by using Heater-3
(Condition 4) Heat input by using Heater-4

The maximum heat input to the coil was about 0.5 W when the Heater-1 and the Heater-2 were used. When the Heater-3 and the Heater-4 were used, on the other hand, the maximum of the heat input was about 3 W. The maximum heat input was determined by the limit of the heater. Figure 64 shows the results of measurements using Heater-1 and Heater-2, and the measurements with Heater-3 and Heater-4 are shown in Fig. 65. From these measurements, the thermal characteristics of the conduction-cooled prototype were obtained in the longitudinal and circumferential direction. Figure 66 (b) shows change in temperature as a function of heat input in the longitudinal direction with the thermal resistance circuit illustrated in Fig. 66 (a). When heat was applied using Heater-1 and Heater-2, the temperature change of the coil for each heater is almost the same due to the effect of the Al strips attached in the longitudinal direction.

Change in temperature by heat input in the circumferential direction is given in Fig. 67 (a) with thermal resistance circuit as illustrated in Fig. 67 (b). The temperature change of the coil for each heater becomes large as heat input increases with Heater-3 and Heater-4, because there are some places where the Al strips are not attached in the circumferential direction. In Chapter 5, we discuss the measurements in relation to the cooling design.

In addition, from the measurement results with Heater-3 and Heater-4, it is observed that the temperature rise of the coil becomes more moderate with increasing heat input, i.e., the thermal characteristics of the coil appear to improve as the temperature rises. This is probably because the thermal conductivity of the pure-Al strip utilized as the cooling plate peaks between 10 K and 20 K, as shown in Fig. 41.

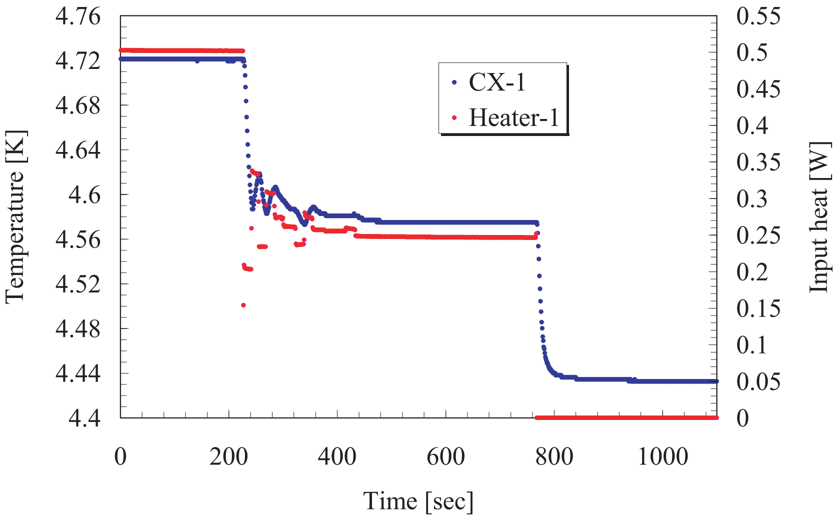

(a) Heat input by using Heater-1

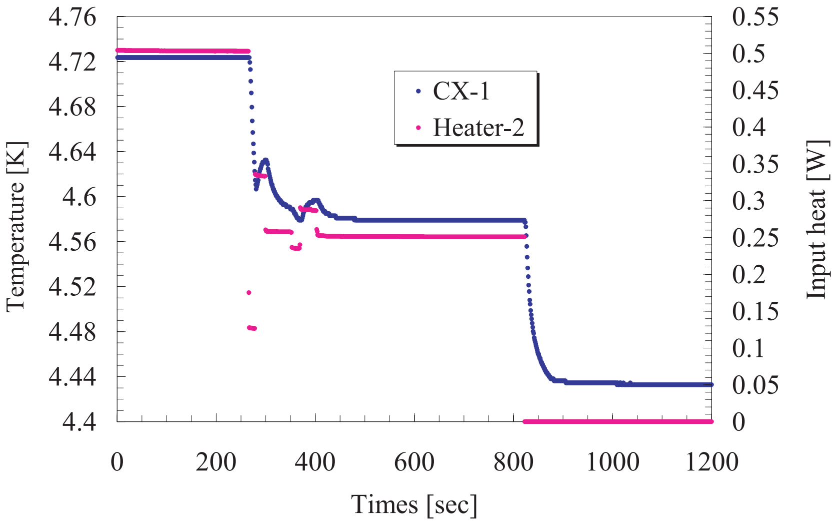

(b) Heat input by using Heater-2

Figure 64: Results of condition 1 and condition 2

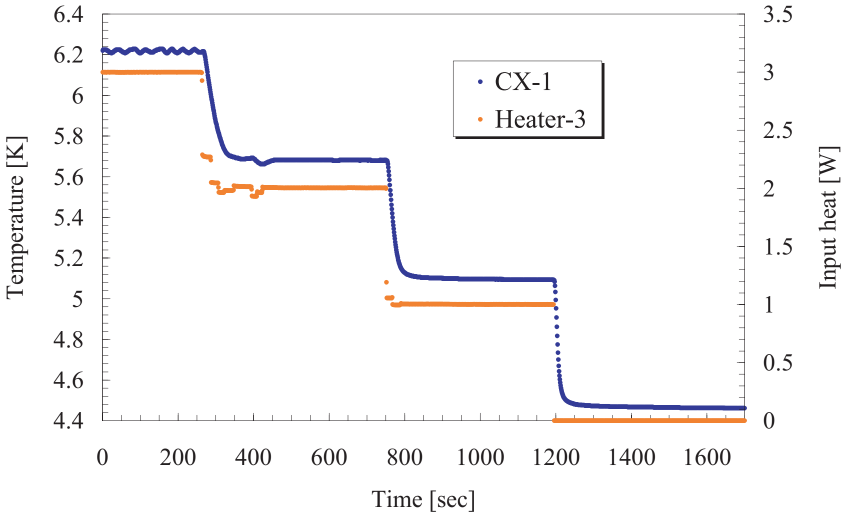

(a) Heat input by using Heater-3

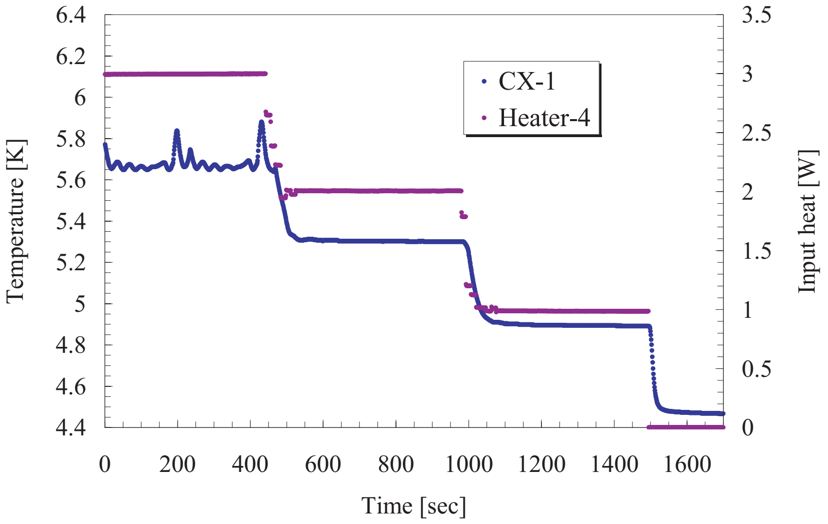

(b) Heat input by using Heater-4

Figure 65: Results of condition 3 and condition 4

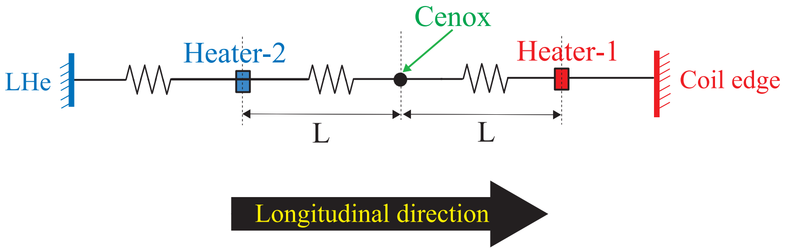

(a) Thermal resistance circuit

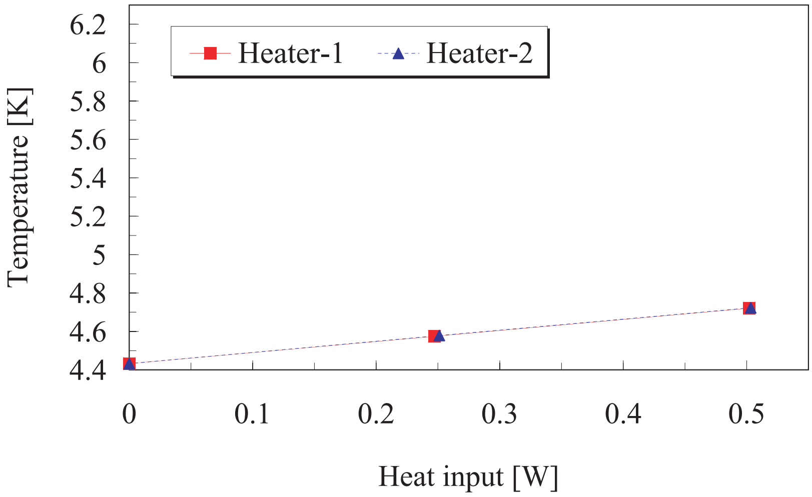

(b) Measurement result in longitudinal direction

Figure 66: Change in temperature by heat input in longitudinal direction

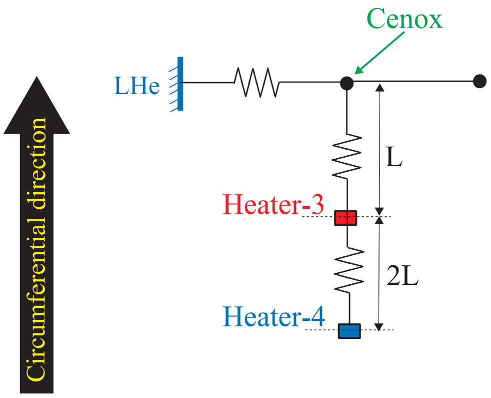

(a) Thermal resistance circuit

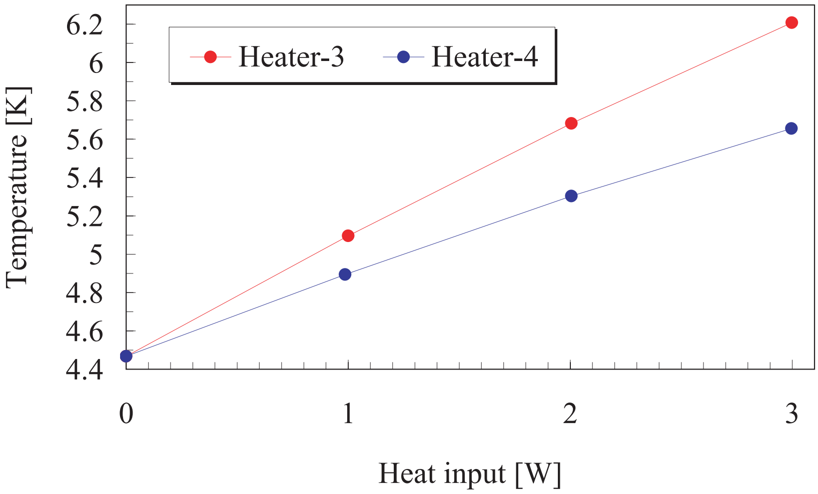

(b) Measurement result in circumferential direction

Figure 67: Change in temperature by heat input in circumferential direction

Table 19: List of the Hall sensors

Position	Model number	Maximum Absolute Error
Hall-1	BHT-921	0.236 % at 1 kGauss
Hall-2	BHT-921	-0.145 % at 1 kGauss
Hall-3	BHT-921	-0.236 % at 1 kGauss
Hall-4	BHT-921	-0.235 % at 1 kGauss
Hall-5	BHT-921	0.182 % at 1 kGauss
Hall-6	BHT-921	-0.045 % at 1 kGauss
Hall-7	BHT-921	0.191 % at 1 kGauss

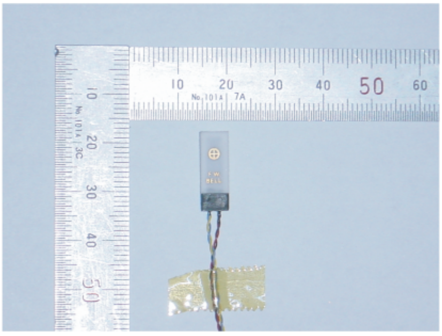

Figure 68: Hall sensor used in the cold measurement

4.3 Measurement of the magnetic field at LHe temperature

Magnetic field measurement was carried out with the prototype coil cooled down to LHe temperature.

4.3.1 Apparatus for cold measurement

Hall sensors were used to measure magnetic field. Lists of the Hall sensors are given in Table 19, and Fig. 68 shows the photo of the Hall sensors. The Hall sensors were set on a FRP board, which did not move in the measurement, as shown in Fig. 69.

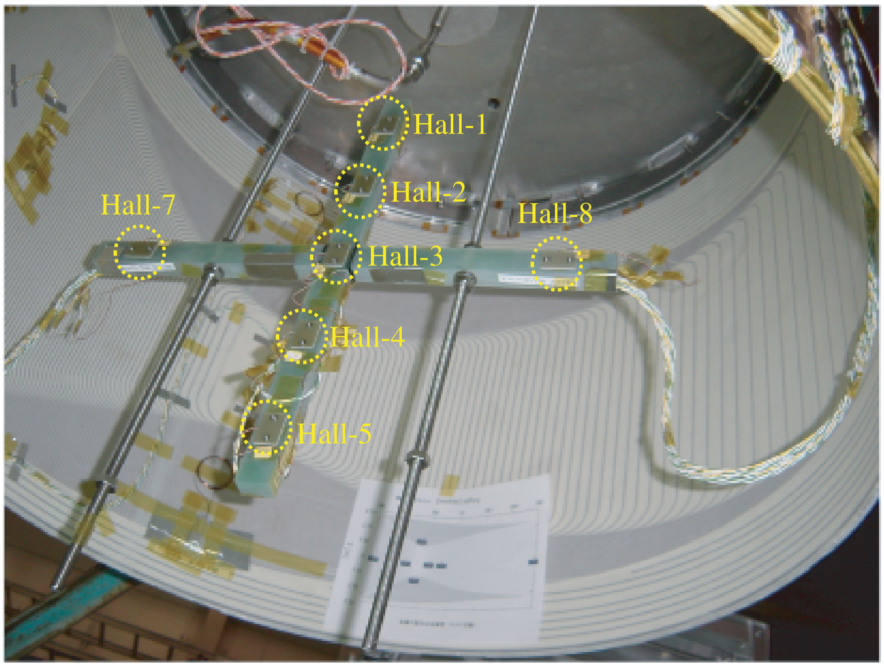

Figure 69: Hall sensors set on the FRP board inside the coil

Table 20: Region of the measurement

Axis	Range
x	-0.2 m $\sim$ 0.2 m
y	0.0 m
z	-0.4 m $\sim$ 0.0 m

4.3.2 Measurement condition

Figure 70 shows the position of the Hall sensors inside the coil to measure magnetic field on the mid-plane along x-axis and z-axis. The region of the measurement is listed in Table 20. In the measurement, the range of the current which was passed through the coil was from 8.0 A to -8.0 A. The magnetic field generated by the coil was therefore low. The measurement method described in Chapter 4 was used in the measurement.

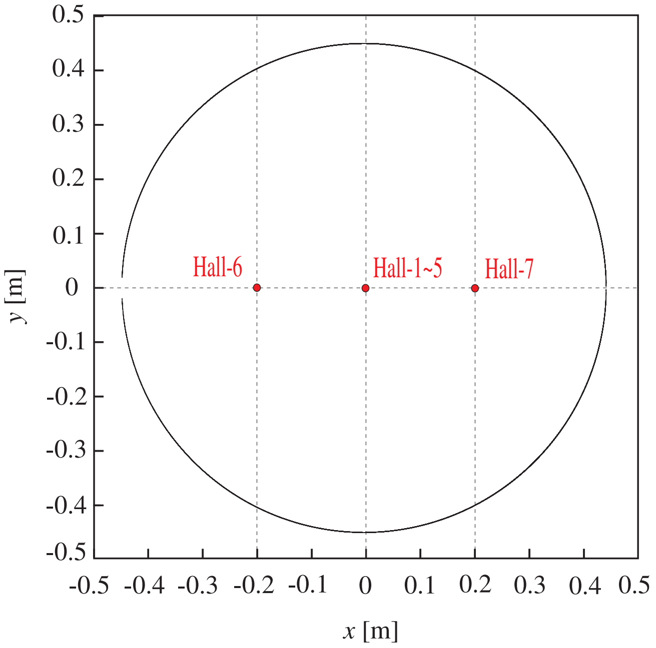

(a) Position of the Hall senser in *x*-*y*

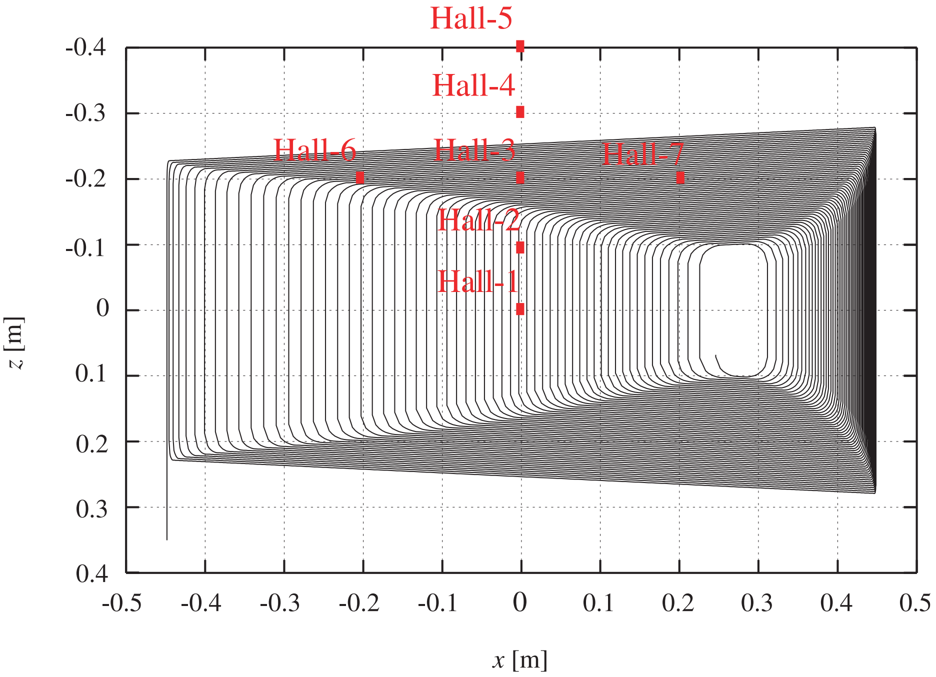

(b) Position of the Hall senser in *x*-*z*

Figure 70: Position of the Hall sensors in the measurement

4.3.3 Results

The measurement of the vertical magnetic field on the mid-plane was carried out at LHe temperature. Figure 71 (a) shows the normalized vertical magnetic field distribution on the mid-plane along z-axis at $x=$ 0.0 m, and the magnetic field distribution along x-axis at $z=$ -0.2 m is shown in Fig. 71 (b). The magnetic fields were normalized to the vertical magnetic field strength on the mid-plane at the coil center. The measured magnetic field distribution along z-axis is consistent with the calculation as shown in Fig. 71 (a). In the magnetic field along the x-axis, on the other hand, a small difference between the measurement and the calculation is observed. The cold measurement was not performed with as high accuracy as the warm measurement, because it was more difficult to set the Hall sensors precisely inside the coil. As a consequence, it is considered that the difference might be due to position errors.

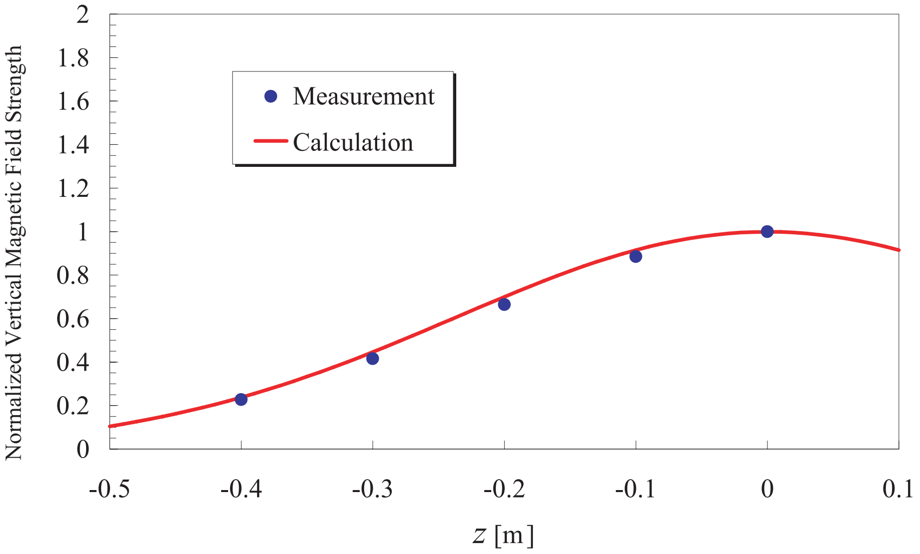

(a) Magnetic field distribution on mid-plane along z axis at $x = 0.0$ m

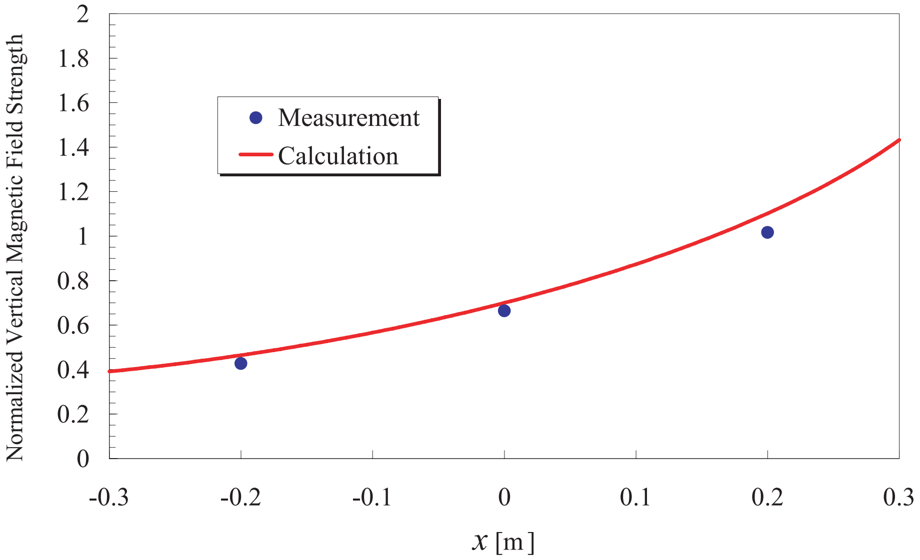

(b) Magnetic field distribution on mid-plane along x axis at $z = -0.2$ m

Figure 71: Magnetic field distributions on mid-plane at cold

4.4 Summary of Chapter 4

In order to verify that the required magnetic field for the FFAG magnet can be realized, the vertical magnetic field generated by the prototype coil has been measured at room temperature not only within the coil bore but also outside. It was found that the required magnetic field is generated with a maximum error of 10%. In addition, the magnetic field has been measured with the magnet cold and superconducting.

The thermal characteristics of the prototype with conduction cooling through pure-Al strips have been examined with the aim of building the superconducting FFAG magnet with conduction cooling. The prototype was cooled from room temperature to about LHe temperature by conduction cooling. The Al strips were attached in the longitudinal direction of the prototype, so that change in temperature was different in each direction when heat was applied. It has been confirmed that pure-Al strips dominate the thermal conductance of the prototype at around LHe temperature. The possibility of using conduction cooling for the superconducting FFAG magnet has been verified.

5 Discussion

As described in Chapter 4, the magnetic field measurement was performed with the prototype coil at room temperature and at about 4 K. In this Chapter, we first discuss the measurement and the calculation results of the magnetic field in this Chapter. Next, the relation between size of the coil aperture and the magnetic field distribution is discussed. Finally, further subjects to be studied for the realization of a superconducting FFAG accelerator magnet are proposed.

5.1 Evaluation of magnetic field generated by the prototype coil

The magnetic field generated by the prototype was measured in warm and cold conditions. Since there were many more precise measurement results in warm conditions, it was decided to use the warm measurement results to evaluate the field quality of the prototype.

As a cause of measurement errors, the alignment accuracy of the coil and the position accuracy of the probe, measurement accuracy of the probe etc. are considered. When the triaxial stand extends the arm on which the Hall probe is attached, a position error of the probe is caused as listed in Table 21. It is therefore supposed that the position accuracy of the probe has an influence on the warm measurement.

5.1.1 Correction on z-axis

The results shown in Fig. 52 were first corrected with respect to the measurement position in z-coordinate. In this correction, the peak positions in the magnetic field distributions of the measurement and the calculation, which are convex upward curves, were matched by shifting the z-coordinate. The shift of z-coordinate for each position on the x-axis are listed in Table 22. The corrected results obtained are as shown in Fig. 72. A similar correction was performed on the results in Fig. 53, which are the magnetic field distribution along the x-axis for each z position. A correction for the z-coordinate shift of 7 mm was made in the return end side, on the other hand, a correction of 10 mm was carried out on the lead end side. The corrected results are shown in Fig. 73. Compared to the non-corrected results, the corrected measurements match better the calculation. However, some difference between the measurement and the calculation is still visible.

5.1.2 Correction on x-axis

In order to understand better this observation, the effect of the position error of the probe was examined in more detail. Figure 74 shows the error of vertical magnetic field strength at the coil center in the conditions that the mid-plane of the coil is shifted by 0.6 mm in the direction of the y-axis or by 4 mm in the direction of the x-axis as listed in Table 21. The error caused by the mid-plane shift along the x-axis is much larger than that caused by the mid-plane shift along the y-axis. The correction of the results was therefore carried out taking into account the error of the mid-plane shift in the x-direction. As shown in Fig. 72, the difference between the measurement and the calculation of the magnetic field distribution along the z-axis at $x=$ 0.2 m is relatively larger than that of the magnetic field distribution at $x=$ 0.0 m and $x=$ -0.2 m. The correction of the results at x = 0.2 m was therefore performed considering the mid-plane of the coil to be shifted by 4 mm in the x-direction. Figure 75 shows the corrected results, where the difference between the measurement and the calculation is smaller than the difference shown in Fig. 72. The correction for the results along the x-axis shown in Fig. 73 was also carried out. After this correction, the measurement agrees better with the calculation, as shown in Fig. 76, as compared to the results shown in Fig. 73. The maximum error between the measurement results and the calculation then goes down to 4 %.

5.1.3 Evaluation of field quality

In order to examine in detail the difference between the measurement and the calculation after the above correction, the results along the x-axis were given with multipole expansion as listed in Tables 23, 24, 25, 26 and 27. Multipole coefficients of the results were obtained from the magnetic field distribution on the mid-plane in the beam excursion region which is between -0.2 m and 0.2 m on the x-axis. From the results, the difference between the measurement and the local calculation becomes large as the position moves away from the coil center. At the coil center which is $z = 0.0$ m, the maximum difference is about 60 units for each b_n. However, the maximum difference is about 160 units for z = -0.4 m (which is outside the coil).

The effect of the coil deformation for the magnetic field was also investigated. Because the coil configuration was only maintained with thin struc-

Table 21: Position error of the probe when the triaxial stand stretches the arm out along the z-axis

	Maximum error of the probe position
x-axis	4.0 mm
y-axis	0.6 mm

Table 22: Shift of z-coordinate for each position on the x-axis

	Return end side	Lead end side
x = -0.2 m	7 mm	7 mm
x = 0.0 m	7 mm	10 mm
x = 0.2 m	5 mm	12 mm

tural shells attached to the outside of the coil after the coil was removed from the winding frame, it is possible that the coil was deformed by mechanical stress. The surface of the coil also contains asperities of maximum size about 1 mm due to the fabrication. The condition that the minor axis of the coil is shrunk by 1 mm was used in the case. The difference between the multipole expansion for the coil and the deformed coil is listed in Table 28. The maximum difference is a few ten units for each b_n, so it can be assumed that the effect of the deformation by 1 mm is relatively small. Figure 77 shows the difference multipole coefficients between the coil and the deformed coil with each condition: it is confirmed that the difference increases with the deformation of the coil.

The above analysis is the best that can be done with the present constraints. Any further refinement would require measurements to be made at higher field levels, i.e. with the coil superconducting and carrying a higher current. The coil would have to be equipped with a rigid internal shell to prevent deformation, and an improved measurement stand would be required.

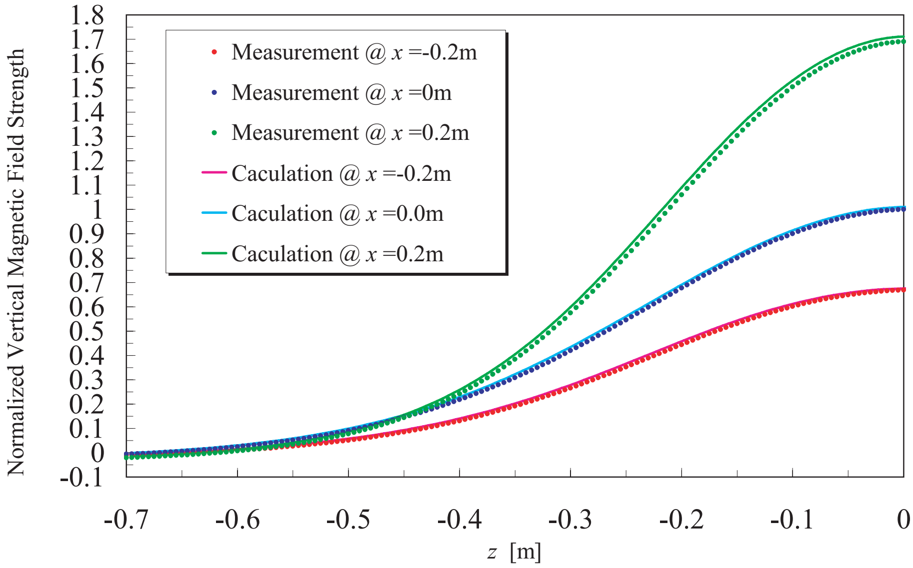

(a) Return end side

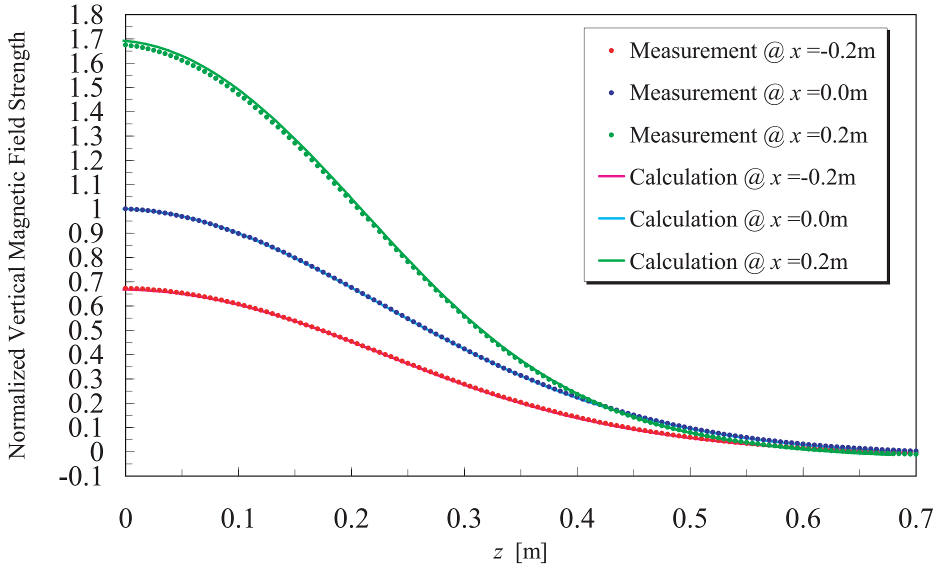

(b) Lead end side

Figure 72: Magnetic field distributions on mid-plane along z-axis for several values of x, after the correction in z-direction

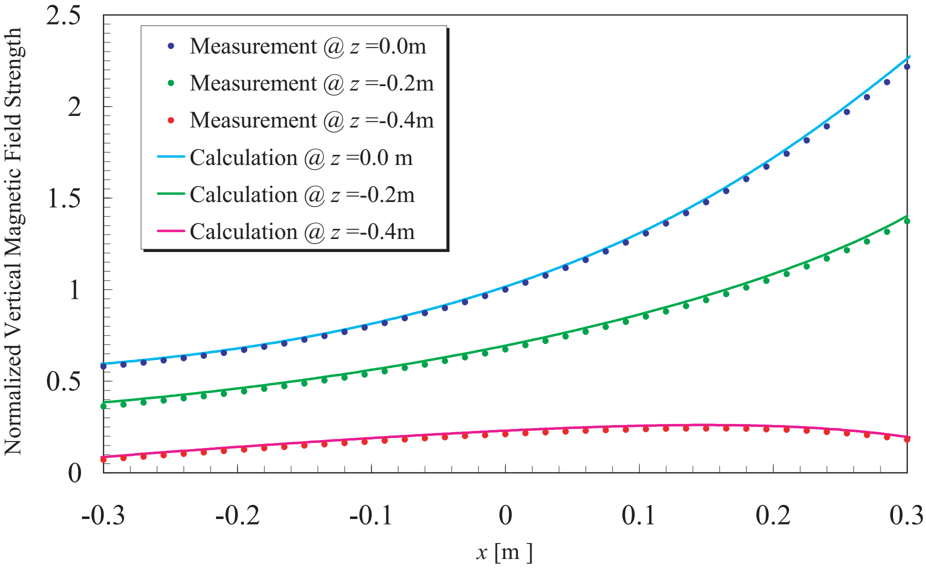

(a) Return end side

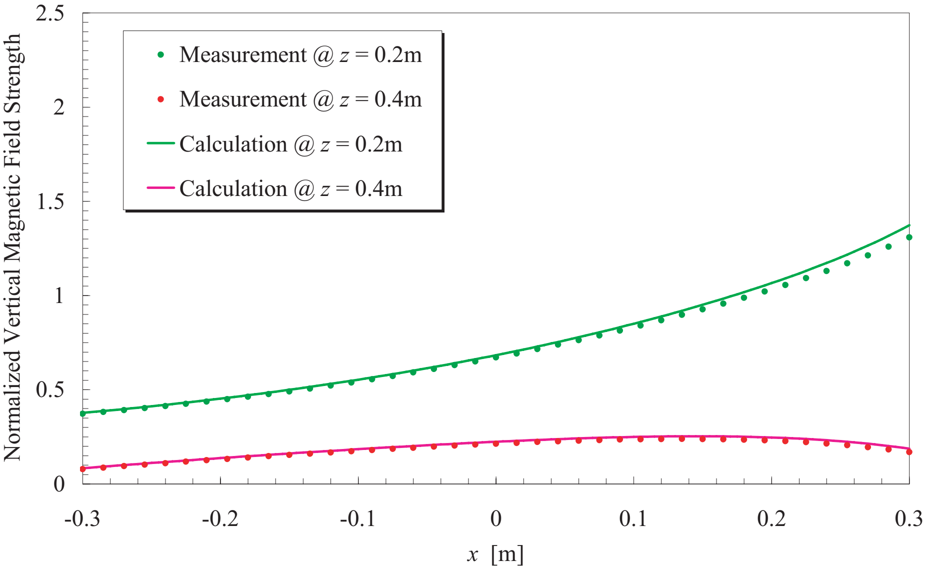

(b) Lead end side

Figure 73: Magnetic field distributions on mid-plane along x-axis for several values of z, after the correction in z-direction

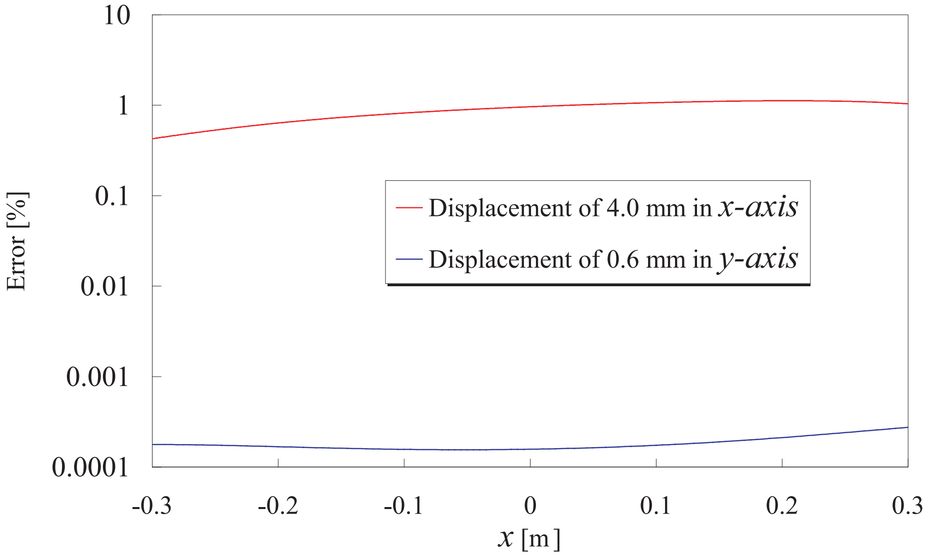

Figure 74: Error of the magnetic field on the mid-plane at the coil center in terms of the displacement

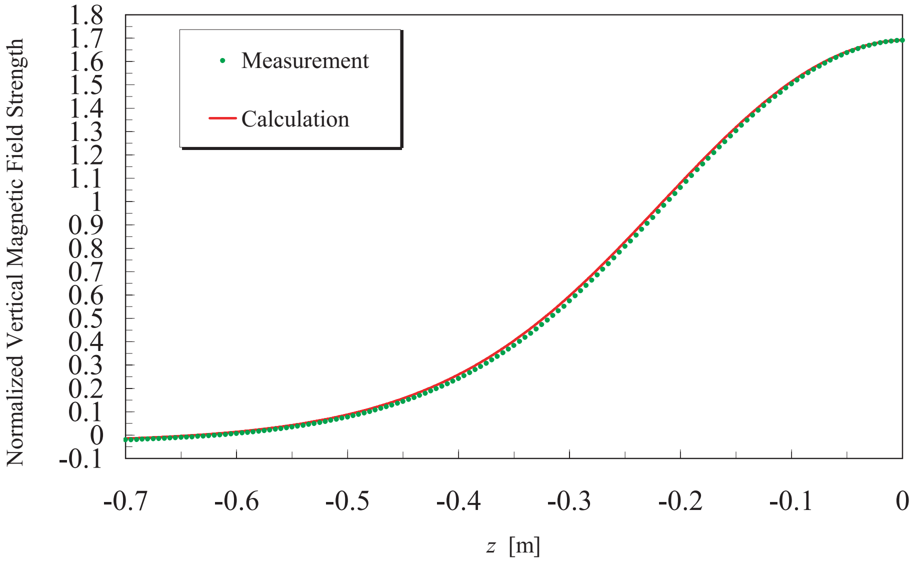

(a) Return end side

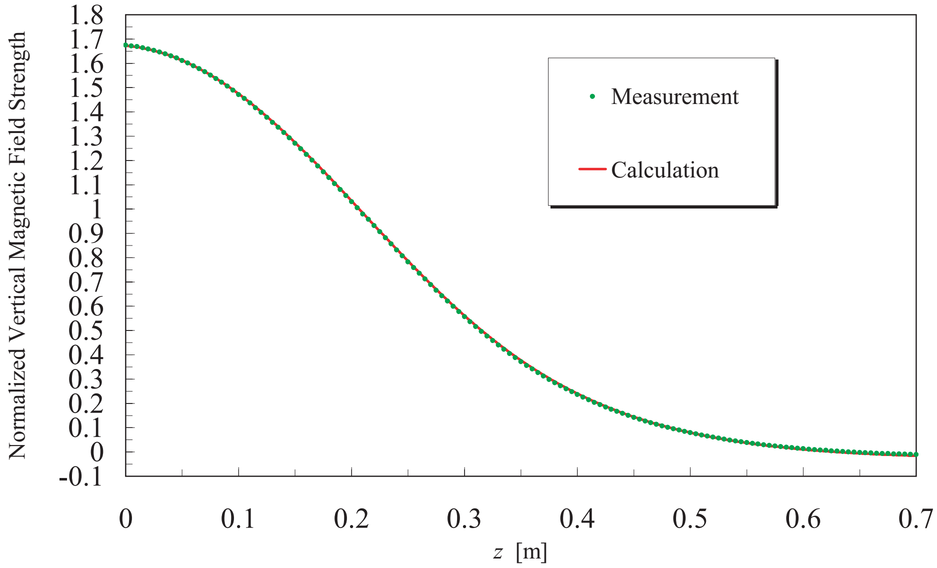

(b) Lead end side

Figure 75: Magnetic field distributions on mid-plane along z-axis at $x = 0.2$ m after the correction of an error of 4 mm in the x-direction

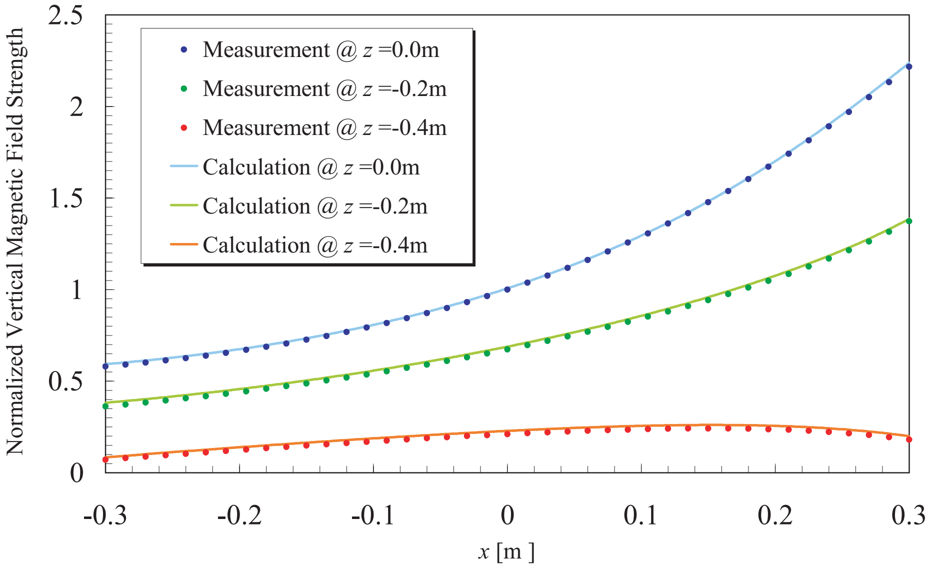

(a) Return end side

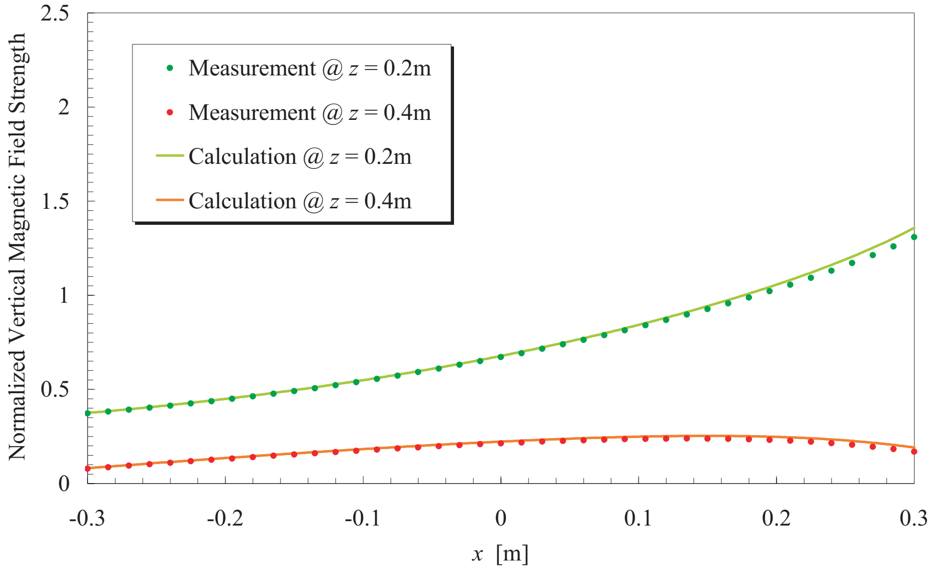

(b) Lead end side

Figure 76: Magnetic field distributions on mid-plane along x-axis after the correction of an error of 4 mm in the x-direction

Table 23: Normal multipole coefficients at z= 0.0 m, reference radius is 0.2 m.

	Measurement	Calculation	Difference
b_1	10000	10000	0
b_2	4803	4743	60
b_3	1777	1747	30
b_4	386	392	-6
b_5	33	80	-47
b_6	-43	-34	-9
b_7	-16	-24	8
B_0	1.00	1.01	-0.01

Table 24: Normal multipole coefficients at z= 0.2 m, reference radius is 0.2 m.

	Measurement	Calculation	Difference
b_1	10000	10000	0
b_2	4273	4307	-34
b_3	976	1077	-101
b_4	52	114	-62
b_5	3	1	2
b_6	50	52	-2
b_7	27	32	-5
B_0	0.67	0.68	-0.01

Table 25: Normal multipole coefficients at z= 0.4 m, reference radius is 0.2 m.

	Measurement	Calculation	Difference
b_1	10000	10000	0
b_2	2990	3104	-114
b_3	1304	1159	145
b_4	608	525	83
b_5	245	230	15
b_6	42	55	-13
b_7	-4	-9	5
B_0	0.21	0.22	-0.01

Table 26: Normal multipole coefficients at z= -0.2 m, reference radius is 0.2 m.

	Measurement	Calculation	Difference
b_1	10000	10000	0
b_2	4423	4320	103
b_3	1082	1099	-17
b_4	112	122	-10
b_5	15	2	13
b_6	64	52	12
b_7	32	32	0
B_0	0.67	0.69	-0.02

Table 27: Normal multipole coefficients at z= -0.4 m, reference radius is 0.2 m.

	Measurement	Calculation	Difference
b_1	10000	10000	0
b_2	3283	3125	158
b_3	1217	1119	98
b_4	535	512	23
b_5	220	228	-8
b_6	69	57	12
b_7	-18	-11	-7
B_0	0.21	0.23	-0.02

Table 28: Difference between the prototype coil and the deformed coil, reference radius is 0.2 m.

	Prototype coil	Deformed coil (Minor axis - 1 mm)	Difference
b_1	10000.0	10016.7	16.7
b_2	4768.2	4773.2	5.0
b_3	1752.6	1752.9	0.3
b_4	395.0	394.6	-0.4
b_5	78.3	78.3	0.0
b_6	-37.3	-37.1	0.2
b_7	-24.9	-24.9	0.0

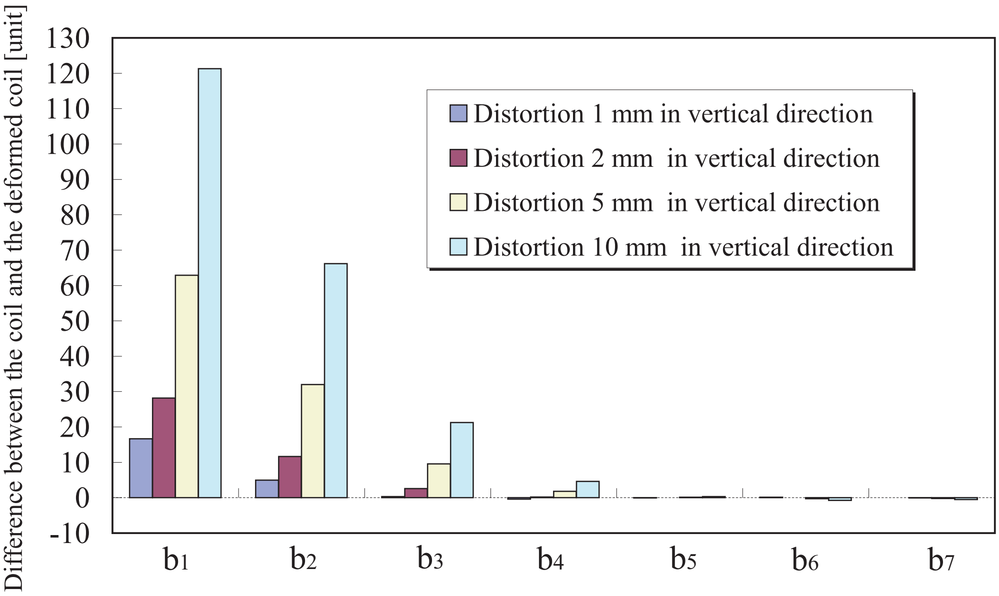

Figure 77: Difference between multipole coefficients for the deformed coil and non-deformed coil for several values of distortion in the vertical direction

5.1.4 Evaluation of error

Based on the measurements at the coil center where the position in z-axis is 0.0 m, the evaluation on the error of the magnetic field was carried out in order to understand whether the field quality of the prototype coil is suitable for the FFAG magnet. As mentioned in Chapter 2, the field quality of the magnet is required in the region of the *local* $k + 1 \pm 0.2$ from the particle tracking simulation. The difference 0.2 in the *local* $k+1$ corresponds to a maximum difference of 80 units in the multipole coefficients given in Appendix F. The maximum difference between the measurement and the calculation is 60 units in b_2 as described above, and a few or a few tens of units of error occur in the higher harmonics. Although the effect of the error on the beam is a concern, the beam should circulate stably with the field quality generated by the prototype coil.

Additionally, the influence of the error on the tune was examined so as to understand the effect on the beam caused by the error. From the results in the Appendix F, a difference about 0.1 in horizontal tune and a difference about 0.02 in vertical tune could occur with the above field error. As a result, the tune should not cross the resonance lines due to the error. It is therefore considered that the observed error level is acceptable problem for the beam.

5.2 Relation between coil aperture and magnetic field distribution

The design of the coil cross-section for the FFAG magnet was performed with the developed computer code described in Chapter 2. As shown in Fig. 6, the required magnetic field can be practically realized in the range of the beam excursion which is between x= -0.2 m and x= 0.2 m on the mid-plane by using the designed cross-section. A difference between the target and the calculation is, however, observed outside this range. The reason for the difference between the target and the calculation has been investigated.

5.2.1 Optimization threshold dependence

In the design of the cross-section described in Chapter 2, a threshold, which is difference between the target and the calculation for each b_n, was set at 5 units so as to satisfy the design requirement effectively, but only within the excursion. The relation between the threshold and the magnetic field distribution was therefore examined. Figure 78 shows the field distributions with the thresholds which are 5 units, 1 unit and 0.1 unit. The calculated result approached the target slightly better when the threshold was changed from 5 units to 1 unit. As the threshold is reduced from 1 unit, however, the calculated result is not improved. Consequently, the region where the calculated results meet the target could not be expanded by simply changing the threshold of the optimization routine.

5.2.2 Matrix condition dependence

Higher order harmonics have an increasing influence on the magnetic field distribution as one moves away from the coil center. An eighth-order determinant given by Eq. 6 was used to design the cross-section in Chapter 2. The cross-sectional design was thus made with determinants of various order to study the relation between the magnetic field distribution and the order of the determinant. In the design, the rigid threshold for the multipole coefficient b_n was defined as 1.0×10^{-3} unit. The magnetic field distributions for each determinant are shown in Fig. 79. Compared to the results with the eighth-order determinant shown in Fig. 78, the required magnetic field can be generated more widely in the coil by using the cross-section designed with a higher-order determinant than eighth. As a consequence, in order to extend the good field region, the design must be done using a higher-order determinant. The improvement of the field is especially noticeable on the low field side, where the range is from x = 0.0 m to x = -0.4 m. There are relatively large spaces between the conductors on the low field side compared to the high field side as shown in Fig. 5, so that the conductors could be easily located at suitable positions.

5.2.3 Coil aperture aspect ratio dependence

A coil design in which the magnet can be downsized with a reduction in the leakage field, is essential for a practical superconducting FFAG magnet. This can be done by varying the aspect ratio of the coil aperture, but it is a concern that the aspect ratio may have an influence on the magnetic field in the coil. The effect of the aspect ratio on the magnetic field was therefore examined. The conditions were used in this study as follows:

(Condition 1) The aspect ratio of the coil aperture is 0.6 : 0.8
(Condition 2) The aspect ratio of the coil aperture is 0.5 : 0.8
(Condition 3) The aspect ratio of the coil aperture is 0.4 : 0.8
(Condition 4) The aspect ratio of the coil aperture is 0.3 : 0.8

When the cross-section for each aspect ratio was designed, the threshold was defined as 1.0×10^{-3} unit, and a tenth-order determinant was used. The magnetic field distributions for each aspect ratio were obtained, as shown in Fig. 80. From these results, it can be seen that the region in which the calculated result matches the target decreases as the aspect ratio increases. It is thus difficult to maintain the field quality in the coil when decreasing the vertical aperture, based on the design concept described in Chapter 2. However, it can be expected that the good field region which fulfills the target could be expanded moderately by modifying the optimum threshold, the number conductors, and by taking into account the smoothing or averaging effect of multiple layers.

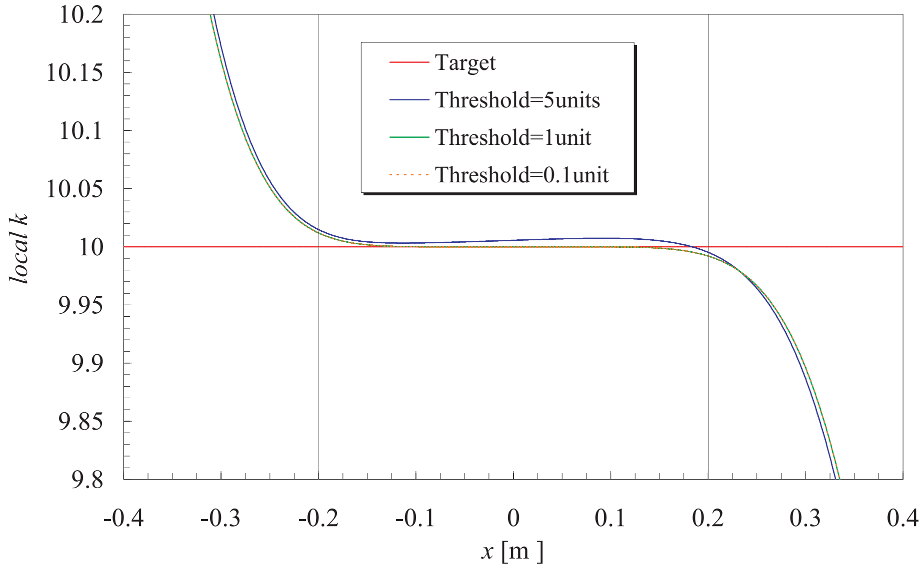

Figure 78: Magnetic field distributions for each threshold

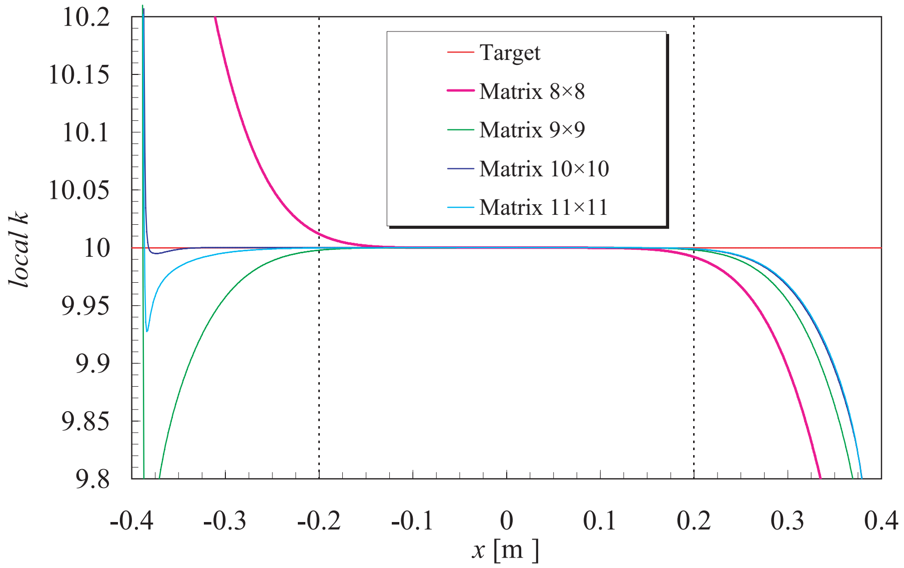

Figure 79: Magnetic field distributions for each matrix condition

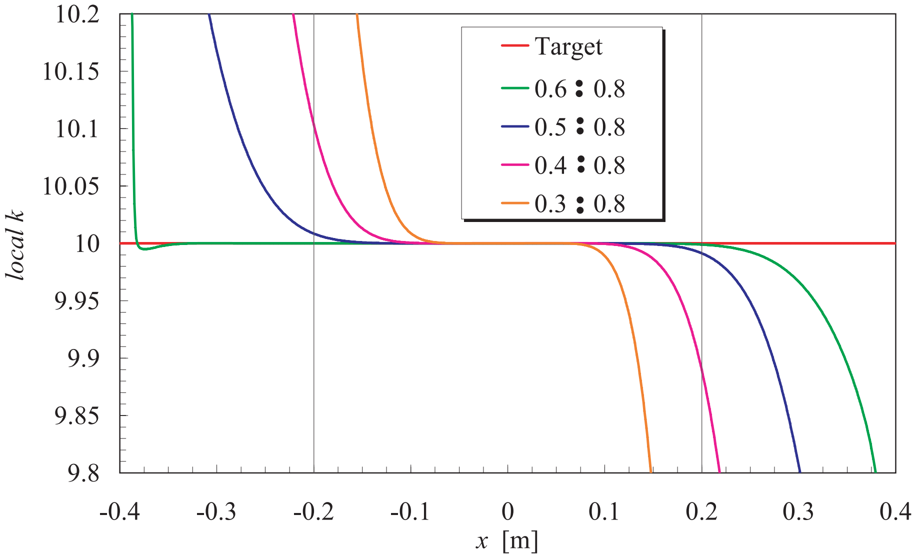

Figure 80: Magnetic field distributions for each aspect ratio of the coil aperture

5.3 Evaluation of thermal characteristics with the conduction cooling

The comparison between the result of measurements and the cooling design was carried out in order to evaluate the thermal characteristics of the prototype coil described in Chapter 4. Based on the assumptions given in Chapter 3, the temperature of the prototype was estimated in the longitudinal direction when heat was applied to the winding. In the cooling design, it was supposed that heat flows in the part of the prototype with the pure-Al strips, and the initial temperature of the coil is that of the LHe, measured before heat input. The thermal conductivities used in the design are listed in Table 29, and the thermal resistance circuit of the design is illustrated in Fig. 81 (a). Figure 81 (b) shows the result of the cooling design and the measurement, in which the dotted-lines show the design value with the aggregate thermal conductivity of the prototype at 5 K and 6 K, and the plots show the measurement result obtained by using the Heater-3 as described in Chapter 4. The difference between the measured temperature and the design value is relatively large, because the design was performed in one dimension. However, it was confirmed that the measurement approaches the design when using reasonable thermal conductivities. The pure-Al strips dominate the

Table 29: Thermal conductivity used in the cooling design

Pure-Al strip at 5 K	5000 W/(m·K)
Pure-Al strip at 6 K	6000 W/(m·K)
Epoxy resign	0.03 W/(m·K)
Effective thermal conductivity of the coil at 5 K	350 W/(m·K)
Effective thermal conductivity of the coil at 6 K	420 W/(m·K)

thermal conductance of the prototype, so that the one dimensional cooling design can be utilized to estimate the thermal characteristics of the prototype taking into account the temperature dependence of the thermal conductivity of the pure-Al strip.

In order to confirm that the pure-Al strip glued on the coil actually has reasonable thermal characteristics, the thermal conductivity of the pure-Al strip was examined by measurements obtained by using the Heater-3. Assuming that heat flows only in the circumferential direction of the pure-Al strips, it is estimated that the thermal conductivity is 4233 W/(m·K) at around 5 K. This thermal conductivity corresponds to that of pure-Al, the RRR of which is about 1000.

Based on the above measurement results, the conduction cooling design of the saddle shaped coil with the left-right asymmetric cross-section must be performed taking into account the following considerations. In the case that the coil is cooled by the pure-Al strips attached in the longitudinal direction of the coil, the thermal conductivity of the coil is low in the circumferential direction, especially at the coil straight section. This is because epoxy resin between conductors has a low thermal conductivity. A temperature gradient is generated in the circumferential direction of the coil as shown in Fig. 67 when heat is applied. In addition, there are relatively large spaces between conductors on the low field side, so there is a concern that a large temperature gradient in the coil may occur in the circumferential direction on that side. In order to minimize the temperature gradient in the circumferential direction, it is necessary to improve the thermal conductance by the reduction of spaces between pure-Al strips as much as possible, taking into account eddy current loss. It would be interesting to examine the possibility of introducing pure-Al strips in the large space between conductors.

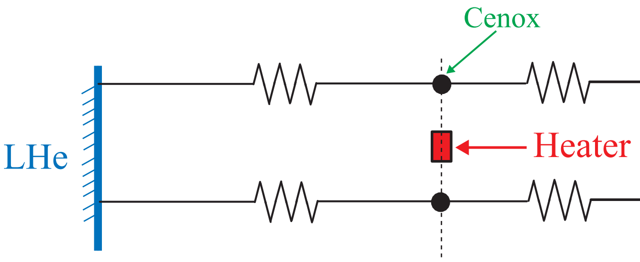

(a) Thermal resistance circuit for the cooling design

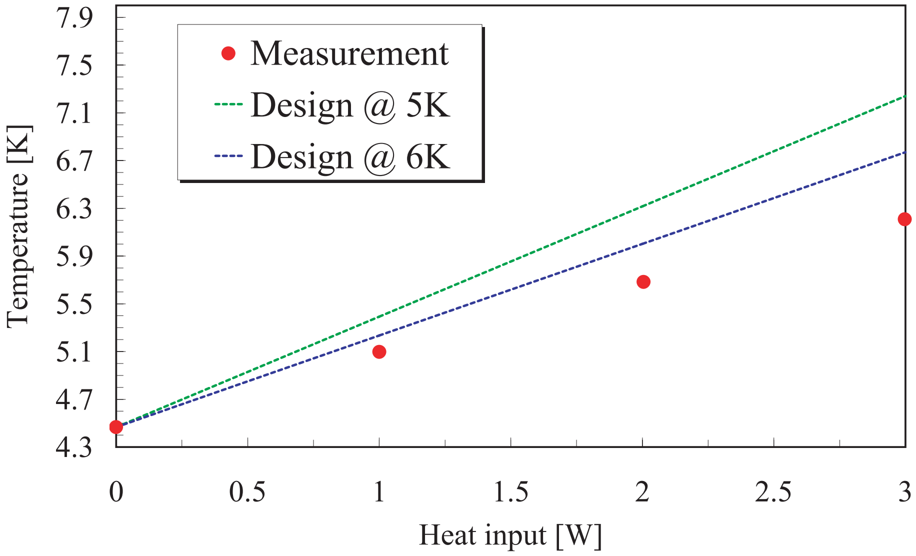

(b) Results of the cooling design and the measurement

Figure 81: One dimensional cooling design and measurement result

5.4 Further subjects for the realization of the superconducting FFAG accelerator magnet

For the realization of the superconducting FFAG accelerator magnet, there are many future issues, which include its design, fabrication, cooling system, the quench protection. Based on the obtained results, some possible answers for the issues are discussed.

5.4.1 General magnet design

First of all, let us consider the general design of the magnet. For this application, it is required to minimize the overall size of the magnet. In order to reduce the space required for the accelerator, and also to limit the stored magnetic energy, the magnet should be as compact as possible. As a suitable solution for the compact magnet, it is proposed to increase the aspect ratio of the coil aperture, i.e., the magnet aperture is reduced vertically, provided that a good field region can be maintained despite the difficulty discussed in the previous section. It is also necessary to take into account the leakage field from the magnet in the design. The leakage field has a great influence on equipment such as RF cavity etc. which is placed between magnets, and must be reduced wherever possible. In the 150 MeV FFAG, the leakage field is reduced to a few hundred Gauss in the RF cavity located between magnets [23]. The leakage field problem can be addressed by reducing the magnet aperture vertically and adjusting the shape of an iron yoke, especially at the edge. In addition, it is suggested that the accelerator parameters such as number of sectors and F/D ratio etc. are modified to provide more space.

Attention must also be paid to the peak field in the magnet in order to keep sufficient stability margin. This means that the configuration of the coil end must be optimized by adjusting the distance between turns at the coil end for each coil layer, as described in Chapter 2.

The higher magnetic field generated by the magnet, the greater above problems become. For the realization of a practical high field superconducting FFAG magnet, therefore, it is essential to address the above problems.

This report concerns the application of a combined-function, high-field superconducting magnet to an FFAG of the "scaling" type, i.e. one based on a DFD lattice cell. This is the type of FFAG for which the first 1 MeV Proof-of-Principle proton machine was shown to work at KEK in 2000, and for which a 150 MeV machine is already operating. More recently there has been a lot of theoretical interest in the so-called "non-scaling" FFAG based on the use of an FDF lattice cell [24]. The tune will be not intrinsically constant in such a machine, but methods are being proposed to alleviate this problem. If it can be demonstrated to work, the FDF scheme could lead to an FFAG with smaller aperture and having a smaller machine radius for a given energy [25], and be one for which the magnet design presented here may be very well suited. In particular, the method of treating the field computation could easily be adapted to take into account the shaping of the edge fields that it would be necessary to address. In order to converge on the most advantageous overall design of the FFAG accelerator it will be important to harmonize the accelerator physics studies with those on advanced superconducting magnets, and take into account developments that may occur in each of these fast-evolving fields.

5.4.2 Iron yoke and magnetic force

From the results in Chapter 2, it was confirmed that the magnetic forces cause a distortion of the magnet. As shown in Fig.36 (b), the maximum distortion is about 0.5 mm when the magnetic field strength is about 1 T at the magnet center. The influence of the distortion on the field quality increases with the excitation of the magnet. A difference in *local k* of about 0.06 over the beam excursion is generated by the distortion in the above case. Based on the results described in Appendix F, the maximum difference in multipole coefficient would be some tens of units with the above difference in *local k*. In addition, the distortion of the magnet would give rise to a tune difference of a few 10^{-2}. It is therefore necessary to take into account the influence of the distortion on the field quality when designing the magnet.

Besides causing errors in the field, the movement due to the magnetic forces can give rise to quenching of the coil. When a conductor moves a distance δ per unit volume due to the magnetic force produced by the excitation, heat, given by Eq. 19, is generated in the magnet [26]:

$$e = I \cdot S_{con}^{-1} \cdot B \cdot \delta \qquad (19)$$

where e is heat quantity, I is current, S_{con} is cross-sectional area of a conductor and B is magnetic field strength. For example, 0.7 MJ/m^3 of heat is produced by the 0.5 mm movement in the case that I is 278 A, S is $0.45^2\pi$ mm^2, and B is 3.4 T as described in Chapter 2. As the heat produced is proportional to both field and displacement, it is essential to minimize the distortion.

The magnetic and mechanical effect of an iron yoke should be taken into consideration when a solution for the distortion is studied. There are two types of yoke: warm iron or cold iron. With the warm iron yoke, the decentering magnetic force on the coil can be canceled out in horizontal direction by optimizing its position in the yoke. In the cold iron yoke, the magnetic bursting force is transferred fully to the cold iron structure. The warm iron yoke does not need to be cooled; the cooling system for the magnet can therefore be simple and efficient compared to that required for the cold iron yoke, the inner diameter of the warn iron yoke is large, and the leakage field is a serious concern. The cold iron with its relatively small inner diameter has an advantage with respect to the leakage field, and mechanical support of the winding.

Based on the above characteristics for each iron yoke, a practical proposal on structural design is advanced as follows. In the magnet with the warm iron yoke, a nonmagnetic metal such as SUS is used as an inner shell attached inside the coil and an outer shell surrounding the coil. In order to reduce the total weight of the magnet, the coil with shells is suspended from mounting rods attached to the iron yoke in the space between the coil and the iron yoke after the position of the iron yoke is optimized.

In the magnet with the cold iron yoke, the inner shell consists of the nonmagnetic metal as is the case with the warm iron yoke. The iron yoke is utilized as the outer shell, for which it is well-suitable, being relatively thick to carry the magnetic flux.

5.4.3 Coil fabrication

In order to develop the practical magnet, we call on experience gained from making the prototype coil. In the process of coil winding, the developed CNC winding machine works with high accuracy according to input data. However, the surface on which a conductor is glued became irregular after epoxy resin was filled into gaps between turns, so that errors occured in the fabrication. When a multilayer coil is made, the error would build up with the influence of each coil layer. In the case of the prototype coil, filling gaps between turns was carried out manually with a trowel as shown in Fig. 46. New fabrication methods should hus be established to make the surface flat. It is also important to use suitable conductor in the fabrication. In the fabrication of the prototype coil, flexible conductor, the diameter of which is about 1 mm, was adopted to wind the coil easily. A moderately large conductor would be suited for the practical magnet which consists of a multilayer coil. A thicker conductor would enable the number of turns and layers, and with that the production time of the coil, to be reduced.

5.4.4 Cooling system

The cooling system for the magnet must be optimized for initial cost, energy consumption and the occupied space. Furthermore, ease of operation is required of the system is required. As a candidate, conduction cooling by using cryocoolers can be considered. Space saving and easy of operation can be realized by choosing a small cryocooler, although energy efficiency of the small cryocooler is low. Therefore, the adoption or not of a cryocooler will depend on the accelerator parameters. As a cooling method, conduction cooling with the pure-Al strip is proposed as described in Chapter 4. Pipes for refrigerant can be reduced in the case of conduction cooling, so that the cryostat would be compact and the system would be simple. However, coil stability may be a concern with conduction cooling, due to the temperature distribution in the coil. Especially in the case of the multilayer coil in which heat is not removed easily, optimization of the cooling design is essential. A study of the stability of the multilayer coil should be carried out.

As one feature of the study, it is suggested to measure the temperature difference between coil layers as a function of heat input in order to determine thermal conductance between coil layers. In the cooling design of a multilayer coil, thermal conductance of a few coil layers must be understood not only in the longitudinal and circumferential directions, which have been examined in Chapter 4, but also in the radial direction. This will provide fundamental data. In addition, it is suggested to examine the relation between the coil conductance and the layout of cooling plates. From the measurement result in Chapter 4, it has been verified that the coil which has 28 pure-Al strips attached on every two layers can be cooled down to LHe temperature. Although the stability of the multilayer coil can be improved by using many cooling plates, the cooling plates make the magnet heavy and large. Consequently, optimization of the number and the shape of the cooling plates is necessary in order to determine effective cooling of the magnet.

5.4.5 Quench protection

Suitable quench protection for the magnet is very important to prevent the magnet from damage caused by quench. The quench protection has to be designed taking into account the characteristics of the magnet. In order to estimate the temperature rise in terms of the characteristics of the magnet in which a quench is generated, the following equation [27] is used:

$$\int_0^\infty \left(\frac{I(t)}{S_{con}}\right)^2 dt = \left(\frac{I_0}{S_{con}}\right)^2 t_d = \int_{T_0}^{T_m} \frac{\gamma C(T)}{\rho(T)} dT = U(T_m) \qquad (20)$$

where I_0 is initial current, t_d is characteristic time for the current decay following a quench, $\rho(T)$ is resistivity of the stabilizer, T_0 is initial temperature, T_m is maximum temperature; density γ and specific heat $C(T)$ are averaged over the winding cross-section, and the function $U(T)$, which is the so-called "number of MIITs", is a parameter of a quench.

The maximum temperature T_m and the function $U(T)$ were calculated in the case of a quench generated with initial current 278 A, as described in Chapter 2, in adiabatic conditions, by using Eq. 20 and the parameters of the superconducting wire given in Table 12. Figure 82 (a) shows the relation between the temperature and time after quench, whereas the relation between the temperature and the number of MIITs is shown in Fig 82 (b). As a result, it was confirmed that the temperature increases to over 300 K within 0.4 sec, and the number of MIITs is 14. Hence, rapid current decay, within at most 0.4 sec, is necessary to avoid damage to the magnet.

As a candidate, a circuit was proposed to protect the magnet from the damage caused by a quench. Figure 83 illustrates a simple protection circuit which consists of a switch and an external dump resistor. In the circuit, the switch opens when the start of a quench is detected, and the current decays via the external dump resistor. The current decay for each external dump resister is shown in Fig. 84, when the operating current is 278 A and the inductance is 27 H as given in chapter 2. From the results, it was confirmed that the higher the resistance of the external dump resistor, the lower the temperature rise for time. However, the voltage generated across the terminals of the magnet becomes a concern. At the moment of a quench, the voltage achieves a maximum value given by

$$V_0 = R_{ex} \cdot I_0 \tag{21}$$

The voltage V_0 has to be limited to be less than the withstand voltage of the magnet normally limited to be 1000 V, so the maximum resistance R_{ex} of the external dump resistor is limited. As a consequence, it would be difficult to protect the magnet from the damage by means of only external dump resistor.

Based on the above result, a practical quench protection is considered as follows. First of all, in order to decrease the time constant, the design of the magnet should be such as to reduce the inductance as much as possible. It is also necessary to improve the withstand voltage of the magnet. Furthermore, the magnet will need to be equipped with quench heaters to reduce the temperature of the hot spot where a quench originates, as quench heaters enable the stored energy to be absorbed in the whole magnet winding [28]. As the magnetic field becomes higher, the stored energy becomes larger, and quench heaters would be essential to achieve stable quench protection for a high field superconducting FFAG magnet.

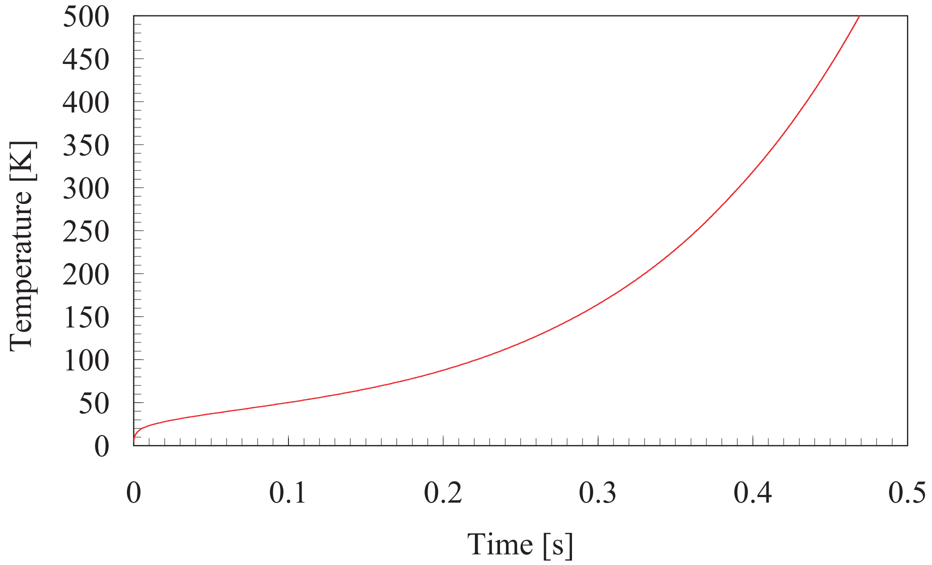

(a) Relation between time and temperature

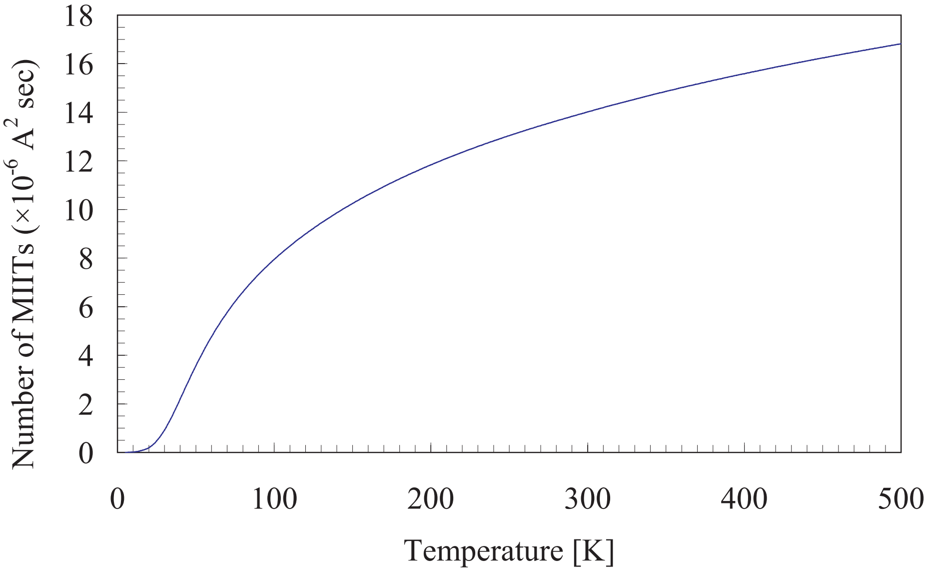

(b) Relation between temperature and number of MIITs

Figure 82: Temperature rise for time and MIITs

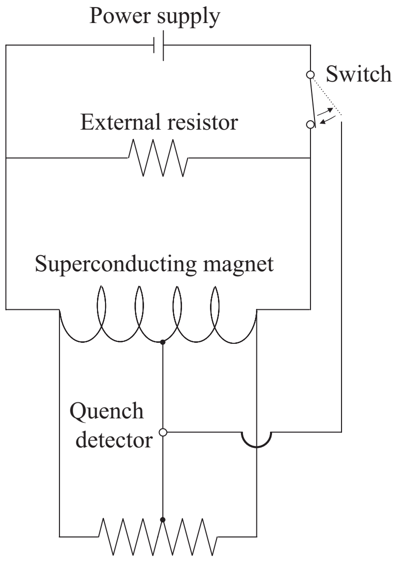

Figure 83: Quench protection circuit by means of a switched external dump resistor

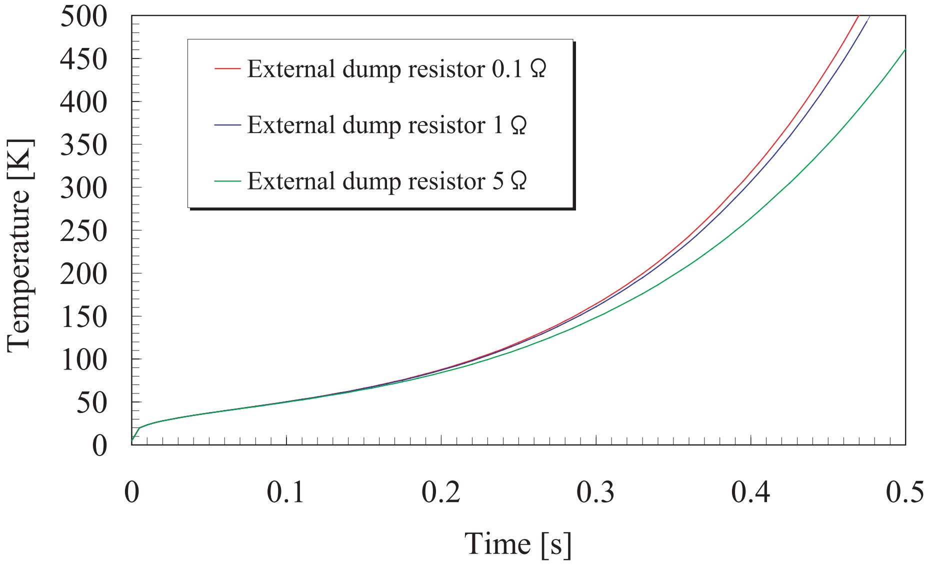

Figure 84: Relation between temperature rise and time for each external dump resistor

6 Conclusion

A study of superconducting combined function magnets containing higher order harmonics has been carried out, aiming at an application for the FFAG accelerator. The required non-linear magnetic field has been investigated by using a computer code originally developed and optimized for large combined function coils of elliptic cross-section and with a pair of saddle shaped coils. It has been understood that the integrated magnetic field along the beam path is the important parameter to be optimized. The field quality was evaluated with a particle trajectory simulation in which the beam could circulate successfully from about 40 MeV to about 210 MeV with stable tune.

A prototype coil has been successfully developed by using a novel coil winding technique which can be applicable for an elliptical coil winding in the future. The magnetic field and cryogenic characteristics of the prototype have been verified in warm and cold measurements, respectively. As a further study for the practical application, it will be necessary to investigate and optimize iron yoke design with respect to the magnetic field and the mechanical stress.

In conclusion, the design study of a superconducting combined function magnet has been made with a view to future application in the FFAG accelerator, and technical feasibility has been verified with prototype magnet development and field measurement. This technology could enable the FFAG accelerator to be smaller in radius for a given beam energy, or to reach a higher beam energy. The stability of this type of high field superconducting magnet for application in a practical FFAG will depend on the specific constraints of the machine regarding occupancy of space and control of stray fields. The superconducting alternative would be to use a superferric magnet. The application of superconductivity will lead to substantial savings in the cost of operation. Future FFAG accelerators can therefore benefit from the use of superconducting magnet technology.

Acknowledgement

The author is most grateful to Prof. A. Yamamoto of KEK for his continuous encouragement and guidance.

The author is most grateful to Dr. T. Ogitsu of KEK for his continuous guidance and a lot of advice.

The author wishes to acknowledge valuable discussions with Dr. M. Yoshimoto of KEK(presently at JAEA).

The author would like to thank Dr. Makida, Dr. N. Kimura, Dr. T. Nakamoto, Dr. T. Tomaru, Dr. K. Sasaki, Dr. C. Mitsuda and Mr. K. Tanaka of KEK for their support and a lot of advice.

The author wishes to acknowledge the members of KEK cryogenics science center for their support.

The author would like to thank Mr. T. Orikasa, Mr. T. Fujii, and Mr. M. Iwasa of TOSHIBA for their support in the fabrication and the field measurement of the prototype coil.

The author wishes to acknowledge TOSHIBA Co., Ltd. for their support in the development of the prototype coil.

The author thanks Dr. M. Aiba of KEK for many discussions.

The author would like to thank Dr. T. Taylor of CERN for his comments on the manuscript.

Appendix

(A)Principle of the FFAG accelerator

The Fixed Field Alternating Gradient(FFAG) means alternating gradient focusing with static magnetic field. The FFAG principle can be applied to various acceleration schemes, such as the synchrotron, betatron, and isochronous cyclotron [15].

In the FFAG synchrotron, the orbit radius increases with acceleration, but the isochronism is not satisfied. It is therefore necessary that the RF frequency is synchronous with the orbital period which changes with beam energy. Consequently, the FFAG synchrotron has strong focusing which is alternating gradient focusing in the transverse direction and phase focusing with RF acceleration in the longitudinal direction.

A unique feature of the scaling FFAG synchrotron is that closed orbits scale for different momenta. Another feature is zero chromaticity, that is the focusing force for different momenta remains constant. These features are derived mathematically. The field gradient n is defined as follows:

$$n\left(s\right) = -\frac{\rho\left(s\right)}{B_0}\frac{\partial B_z}{\partial r} \tag{22}$$

where B_0 is the magnetic field strength at point s, and ρ is the radius of curvature. Here, the betatron oscillation equation is given by

$$\frac{d^2y}{ds^2} + K\left(s\right)y = 0 \tag{23}$$

$K\left(s\right)$ is given for each direction of motion as follows:
In the horizontal direction,

$$K\left(s\right) = \frac{\left(1 - n\left(s\right)\right)}{\rho\left(s\right)^2} \tag{24}$$

In the vertical direction,

$$K\left(s\right) = \frac{n\left(s\right)}{\rho\left(s\right)^2} \tag{25}$$

Here, C and s, which are independent variables, are defined as follows:

$$C = 2\pi \cdot R \tag{26}$$

$$s = R\Theta \tag{27}$$

where C is the length of the orbit, s is the distance along the orbit from some reference point (say at azimuthal angle θ_0), and R is the equilibrium radius. The origin of the angular variable Θ is the point that a line drawn from the accelerator center crosses the equilibrium orbit at right angles as shown in Fig. 85. The trajectory of the intersecting point is defined as the reference curve, the trajectory of the point that is Θ = const. from the origin on each orbit is called the spiral, and the angle that is formed between the spiral and the direction of the radius is called the spiral angle, ζ. With R and Θ so-defined, the betatron oscillation equation can be written as follows:

In the horizontal direction,

$$\frac{d^2x}{d\Theta^2} + (1-n)\left(\frac{R}{\rho}\right)^2 x = 0 \tag{28}$$

In the vertical direction,

$$\frac{d^2z}{d\Theta^2} + n\left(\frac{R}{\rho}\right)^2 z = 0 \tag{29}$$

To ensure constant horizontal and vertical betatron tunes,

$$\nu_x \;=\; const \;,\; \nu_z \;=\; const \tag{30}$$

the following conditions must be satisfied :

$$\left.\frac{\partial}{\partial p}\left(\frac{R}{\rho}\right)^2\right|_{\Theta=const} = 0 \tag{31}$$

$$\left.\frac{\partial n}{\partial p}\right|_{\Theta=const} = 0 \tag{32}$$

Equation 31 means that the ratio of equilibrium radius to radius of the curvature is always equivalent in two points at which two different equilibrium orbits cross an arbitrary spiral, which indicates geometrical scaling of the orbits. Equation 32 imposes n to be the same in two points at which two different equilibrium orbits cross arbitrary spirals, which implies that the focusing force is always the same.

In polar coordinates(r,θ), the following relation holds:

$$(\Delta s)^2 = (r\Delta\theta)^2 + (\Delta r)^2 \tag{33}$$

$$\frac{\Delta s}{\Delta r} = \sqrt{1 + r^2 \left(\frac{\Delta\theta}{\Delta r}\right)^2} \tag{34}$$

Due to the similarity of the orbits, Eq. 34 can be rewritten as

$$\left(\frac{\partial s}{\partial r}\right)_\Theta = \sqrt{1 + r^2 \left(\frac{\partial\theta}{\partial r}\right)_\Theta^2} \tag{35}$$

In this case, Eq. 35 is derived as

$$r\left(\frac{\partial\theta}{\partial r}\right)_\Theta \equiv h = const \tag{36}$$

Eq. 36 can also be written as:

$$h = \left(\frac{r \cdot \partial\theta}{\partial r}\right)_\Theta = \tan\zeta \tag{37}$$

Consequently, in order to realize the similarity of the orbits, it is necessary to satisfy Eq. 37, giving

$$\theta \propto h \ln r \tag{38}$$

on an arbitrary spiral that is Θ = const. The k value is defined as the geometrical field index, which is given by

$$k \equiv \frac{s}{B}\left(\frac{\partial B}{\partial s}\right)_\Theta \tag{39}$$

From Eq. 39, it can be derived that:

$$k = \frac{s}{r}\left(\frac{\partial r}{\partial s}\right)_\Theta \frac{r}{B}\frac{\partial B}{\partial r}_\Theta \tag{40}$$

$$\frac{s}{r}\left(\frac{\partial r}{\partial s}\right)_\Theta = const. \tag{41}$$

Due to the similarity of the orbits given by Eq. 41, Eq. 40 can be rewritten as

$$k = \frac{r}{B}\left(\frac{\partial B}{\partial r}\right)_\Theta \tag{42}$$

Hence, the magnetic field on an arbitrary spiral is given by

$$B(r) \propto r^k \tag{43}$$

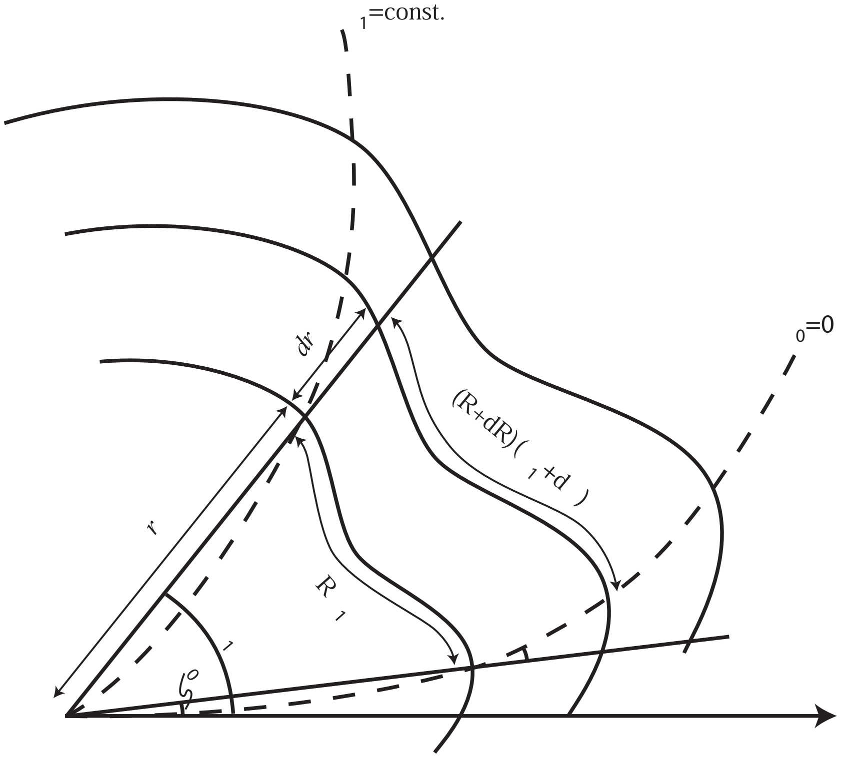

Figure 85: Definition of equilibrium orbit in the FFAG accelerator

where Θ is constant.

When the periodicity of the magnetic field is N, Θ is $2\pi/N$, and θ is also $2\pi/N$. If the periodic function $F(\Theta)$ of $2\pi/N$ is defined, the required magnetic field in the FFAG accelerator can be written in its most general form as:

$$B(r,\theta) = B_0 \left(\frac{r}{r_0}\right)^k F(\theta - h \ln \frac{r}{r_0}) \tag{44}$$

(B)Magnetic field for the radial sector type of the FFAG accelerator

In the radial sector type of a scaling FFAG accelerator, the focusing and the defocusing magnets are arranged alternately with the edge of the magnets falling on the radial line from the accelerator center as shown in Fig. 86 [15]. The direction of the magnetic field gradient is different between the focusing magnet and the defocusing magnet. The edge of the magnets is not perpendicular to the orbits so that the beam undergoes edge focusing there. The spiral follows the radius from the accelerator center in the radial sector type of FFAG, and

$$\zeta = h = 0 \tag{45}$$

Equation 44 can be therefore rewritten as

$$B(r,\theta) = B_0 \left(\frac{r}{r_0}\right)^k F(\theta) \tag{46}$$

where F(θ) is constant and the sign of F(θ) is different between the focusing and the defocusing magnetic field.

In the case that F(θ) is 1 for the focusing field and F(θ) is -1 for the defocusing field, the magnetic field distributions are written as

$$B(r) = B_0 \left(\frac{r}{r_0}\right)^k \tag{47}$$

$$B(r) = -B_0 \left(\frac{r}{r_0}\right)^k \tag{48}$$

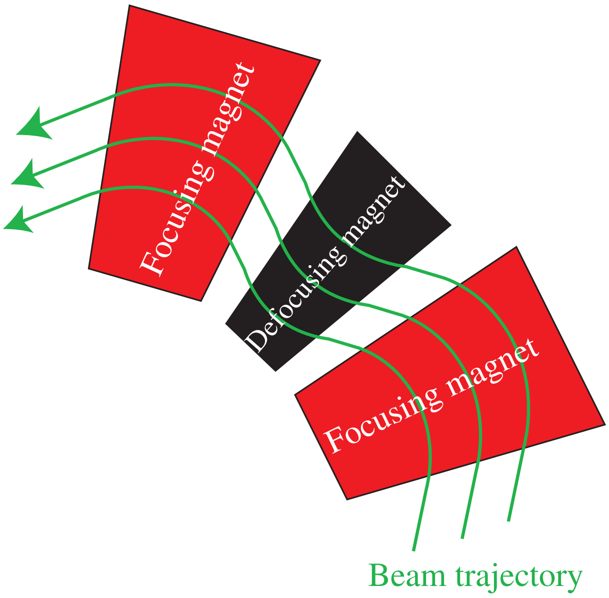

Figure 86: Alignment of radial sector FFAG magnets with beam trajectory

(C)Definition of magnetic field

When magnetic field quality is evaluated, the coordinate system is defined as in Fig. 87 in the cross-sectional view and as in Fig. 88 in three dimensions, respectively. The field generated by magnets is generally expressed in terms of multipole expansion in a beam tube [29]. In the beam tube without currents and magnetized materials, the Maxwell equations hold and are given by

$$\nabla \cdot \boldsymbol{B} = 0 \tag{49}$$

$$\nabla \times \boldsymbol{B} = 0 \tag{50}$$

Conventional superconducting accelerator magnets have the feature that the straight section is relatively long. The magnetic field can be therefore evaluated in the cross-section of the magnet. When currents flow along the z-axis, magnetic field components are produced in the x-y plane. Equation 49 and 50 are consistent with the Cauchy-Riemann conditions. The equations can be given in a multipole expansion as follows:

$$\boldsymbol{B} = B_y + iB_x = \sum_{n=1}^{\infty} (B_n + iA_n) \left(\frac{x + iy}{r_0} \right)^{n-1} \tag{51}$$

where r_0 is reference radius in the beam pipe, B_n is the normal $2n$-pole component, and A_n is the skew $2n$-pole component. The multipole field is

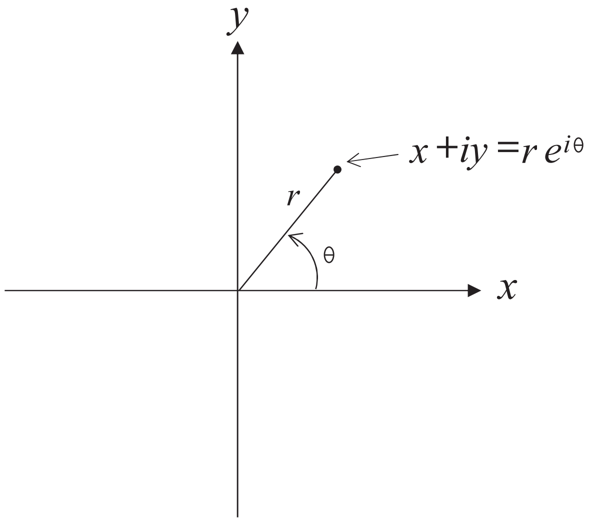

Figure 87: Schematic view of the coordinate system in cross-section

usually evaluated in comparison with the main field of a magnet as follows:

$$\boldsymbol{B} = B_{main} \sum_{n=1}^{\infty} (b_n + i a_n) \left(\frac{x + iy}{r_0} \right)^{n-1} \times 10^{-4} \tag{52}$$

where B_{main} is a main field of the magnet, b_n and a_n are normal and skew multipole coefficients that are normalized by $B_{main} \times 10^{-4}$.

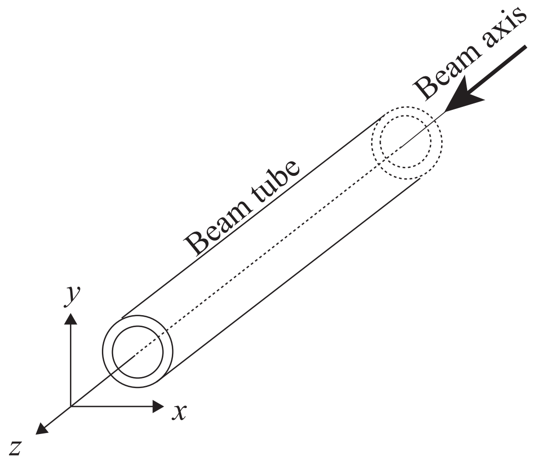

Figure 88: Schematic view of the coordinate system in three dimensions

(D)Multipole expansion for a line current

The multipole magnetic field generated by a line current at a reference radius is considered. According to the Biot-Savart law, the magnetic field that a line current generates at a point which is at distance r from the line current is given by

$$B = \frac{\mu_0 I}{2\pi r} \tag{53}$$

Magnetic field generated by a line current I, which is located at the point $p(r_x, r_y)$, is obtained at the point $q(x, y)$ in two dimensions as shown in Fig. 89 [30]. B_x ans B_y which are the x component and the y component of magnetic field at the point P are given by

$$B_x = B\cos\theta \tag{54}$$

$$B_x = B\sin\theta \tag{55}$$

where $\cos\theta$ and $\sin\theta$ are given by

$$\cos\theta = -\frac{y - r_y}{\sqrt{(x - r_x)^2 + (y - r_y)^2}} \tag{56}$$

$$\sin\theta = \frac{x - r_x}{\sqrt{(x - r_x)^2 + (y - r_y)^2}} \tag{57}$$

Equation 53 can also rewritten as

$$B = \frac{\mu_0 I}{2\pi\sqrt{\left(x - r_x\right)^2 + \left(y - r_y\right)^2}} \tag{58}$$

Consequently, Eq. 54 and Eq. 55 become:

$$B_x = -\frac{\mu_0 I}{2\pi}\frac{y - r_y}{\left(x - r_x\right)^2 + \left(y - ry\right)^2} \tag{59}$$

$$B_y = \frac{\mu_0 I}{2\pi}\frac{x - r_x}{\left(x - r_x\right)^2 + \left(y - ry\right)^2} \tag{60}$$

Here the magnetic field is expressed with the complex expression as follows:

$$\boldsymbol{B} = B_x + iB_y \tag{61}$$

$$\boldsymbol{B} = \frac{\mu_0 I}{2\pi}\frac{1}{\left(x - r_x\right)^2 + \left(y - r_y\right)^2}\left((x - iy) - (r_x - ir_y)\right) \tag{62}$$

$$\boldsymbol{B} = -\frac{\mu_0 I}{2\pi \boldsymbol{r}}\frac{1}{1 - \frac{\boldsymbol{z}}{\boldsymbol{r}}} \tag{63}$$

Equation 63 can be expanded in the Taylor series, giving:

$$for\left|\frac{\boldsymbol{z}}{\boldsymbol{r}}\right| < 1 \tag{64}$$

$$\boldsymbol{B} = -\frac{\mu_0 I}{2\pi \boldsymbol{r}}\sum_{n=1}^{\infty}\left(\frac{\boldsymbol{z}}{\boldsymbol{r}}\right)^{n-1} \tag{65}$$

$$\boldsymbol{B} = -\frac{\mu_0 I}{2\pi}\sum_{n=1}^{\infty}(x + iy)^{n-1}\left(ae^{i\theta}\right)^{-n} \tag{66}$$

$$\boldsymbol{B} = -\frac{\mu_0 I}{2\pi}\sum_{n=1}^{\infty}\frac{(x + iy)^{n-1}}{r_0^{n-1}}\frac{r_0^{n-1}}{a^n}\left(\cos(-n\theta) + i\sin(-n\theta)\right) \tag{67}$$

$$\boldsymbol{B} = -\frac{\mu_0 I}{2\pi}\sum_{n=1}^{\infty}\left(\frac{r_0}{a}\right)^n\left(\cos(-n\theta) + i\sin(-n\theta)\right)\left(\frac{x + iy}{r_0}\right)^{n-1} \tag{68}$$

The normal component of the magnetic field generated by a line current at the reference radius is given by

$$B_n = -\frac{\mu_0 I}{2\pi r_0}\left(\frac{r_0}{a}\right)^n\cos(-n\theta) \tag{69}$$

In addition, Eq. 70 indicates the normal component of the magnetic field generated by line currents, which are located on a circle with radius a, at the reference radius.

$$B_n = \sum_q -\frac{\mu_0 I}{2\pi r_0}\left(\frac{r_0}{a}\right)^n \cos(-n\theta_q) \tag{70}$$

On the other hand, the normal component of the magnetic field generated by line currents as shown in Fig. 90, located on an ellipse with distance r_{θ_k} from the original point, at the reference radius, is written:

$$B_n = \sum_q -\frac{\mu_0 I}{2\pi r_0}\left(\frac{r_0}{r_{\theta_q}}\right)^n \cos(-n\theta_q) \tag{71}$$

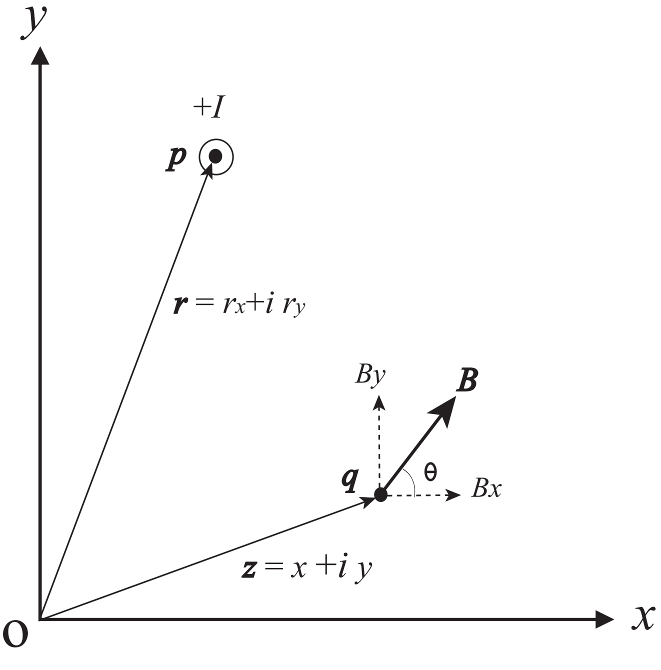

Figure 89: Magnetic field calculation for a line current

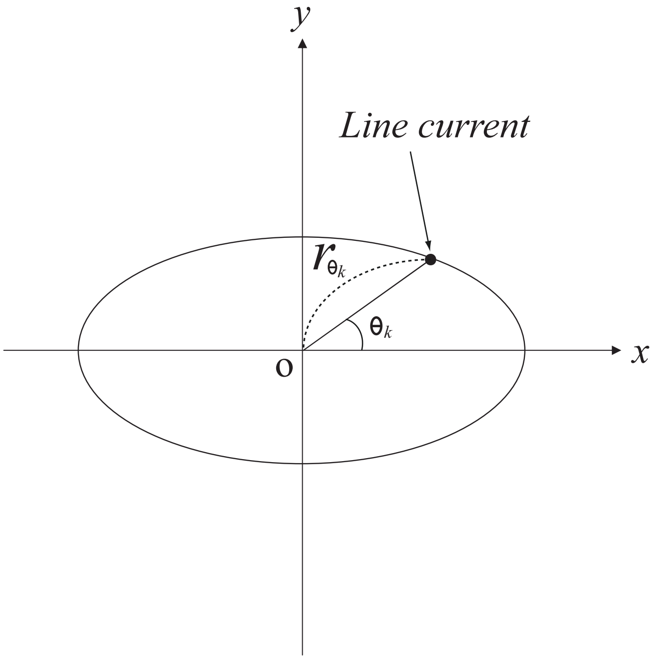

Figure 90: Position of a line current on the ellipse

(E)Computer code for design of coil cross-section

A computer code has been developed in order to design a coil cross-section which can generate nonlinear magnetic field containing higher harmonics with high accuracy by using a single coil layer. In the computer code, the following actions are carried out:

1. Obtain each multipole coefficient b_n to realize the magnetic field required for FFAG magnet.

2. Determine $\cos(\theta)$ current distributions for each multipole coefficient b_n

3. Combine the $\cos(\theta)$ current distributions

4. Arrange conductors on a circle or an ellipse to make the combined current distribution

Table 30: Multipole coefficient b_n for each k at reference radius = 0.2 m

k	10	10.01	10.1
b_1	10000.0	10000.0	10000.0
b_2	4000.0	4004.0	4040.0
b_3	720.0	721.5	735.3
b_4	76.8	77.1	79.4
b_5	5.4	5.4	5.6
b_6	0.3	0.3	0.3
b_7	0.0	0.0	0.0

Table 31: Horizontal and vertical tunes for each k in terms of linear approximation

k	10	10.01	10.1
Horizontal tune	4.976	4.982	5.045
Vertical tune	1.164	1.163	1.155

(F)Multipole coefficient b_n & horizontal and vertical tunes for each field index k

In order to understand the relation between the multipole coefficient b_n and the field index k, the multipole coefficient b_n for each k was calculated, as listed in Table 30. The effect of the field index k on the multipole coefficient b_n was confirmed, and the absolute value of b_n for each k becomes smaller as the harmonic is higher.

Furthermore, the relation between the tunes and the field index k was examined by using the SAD (Strategic Accelerator Design [31]) program which can simulate a particle trajectory with linear approximation. As given in Table 31, the field index k has a greater influence on the horizontal tune than on the vertical tune.

(G)Beam emittance for each coil configuration

In order to examine beam size associated with each coil type, horizontal and vertical emittances were obtained with the tracking simulation. The emittances of the saddle shaped coil and the single winding coil for each beam orbit are illustrated in Fig. 91 and Fig. 92, respectively. From the results, the shape of the horizontal emittance has a tendency to be triangular due to the third order resonance [23]. The horizontal emittance of the single winding coil is much larger than that of the saddle shaped coil; it reaches about forty times as large at r = 5.3 m. Compared to the horizontal emittance, on the other hand, the vertical emittance is relatively small. In the results of the vertical emittance, that of the saddle shaped coil is slightly larger than that of the single winding coil in contrast to the tendency for the horizontal emittance.

The tune has a large influence of the emittance. Hence, the emittance can be improved by adjusting the tune.

(H)Effect of iron yoke

Superconducting accelerator magnets are generally equipped with an iron yoke surrounding the coil. The iron yoke acts as a return path for some of magnetic flux. In addition, the iron yoke shields the effect of magnetic material and fields located outside the magnet from the magnetic field generated inside the magnet. It also enhances the magnetic field. The influence of the iron yoke on the magnetic field can be calculated analytically, providing that the iron is not saturated, that the permeability μ is uniform, and that the inner boundary of the iron is a cylinder. The magnetic field contributed by the iron can be calculated by using the image current based on the above conditions [32]. Consider a current I at a radius an inside a hollow iron yoke, the inner surface of which is a cylinder of radius R_{yoke}. The effect of the iron on the inner field is equivalent to that of an image current I_{image} which is located at the image radius $r_{image} = R_{yoke}/r_I$

$$I_{image} = \frac{\mu - 1}{\mu + 1} I \tag{72}$$

The image current I_{image} runs parallel to the real current I and enhances the inner field. Figure 93 shows the image of a single line current. Moreover, when the origin of the iron yoke is shifted by distance L which is shown in Fig. 94, the image current I_{image} is also given by Eq. 72 [13].

$r = 4.9$ m

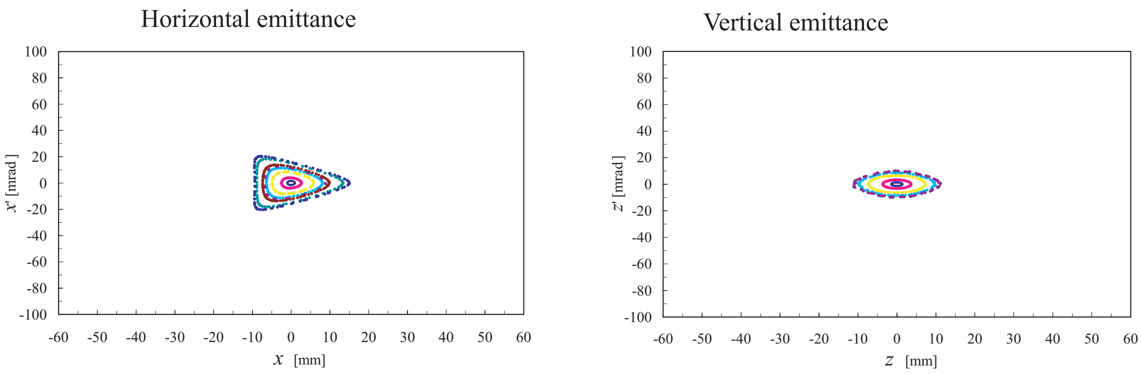

$r = 5.1$ m

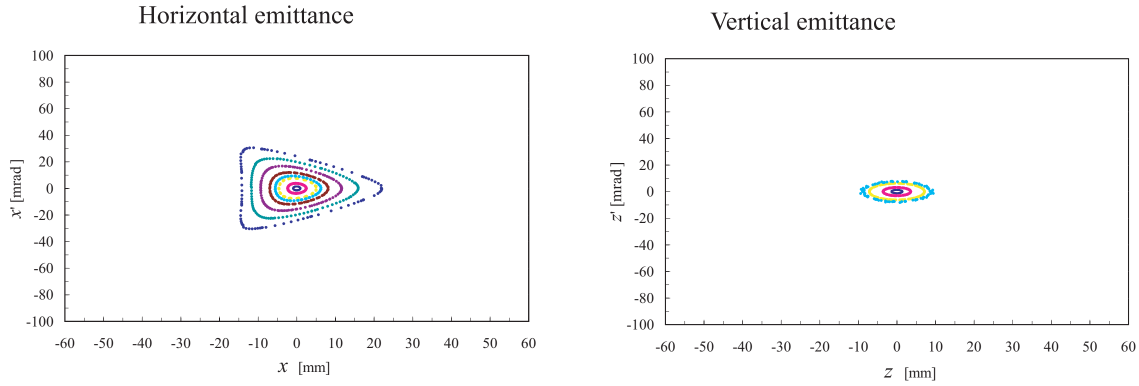

$r = 5.3$ m

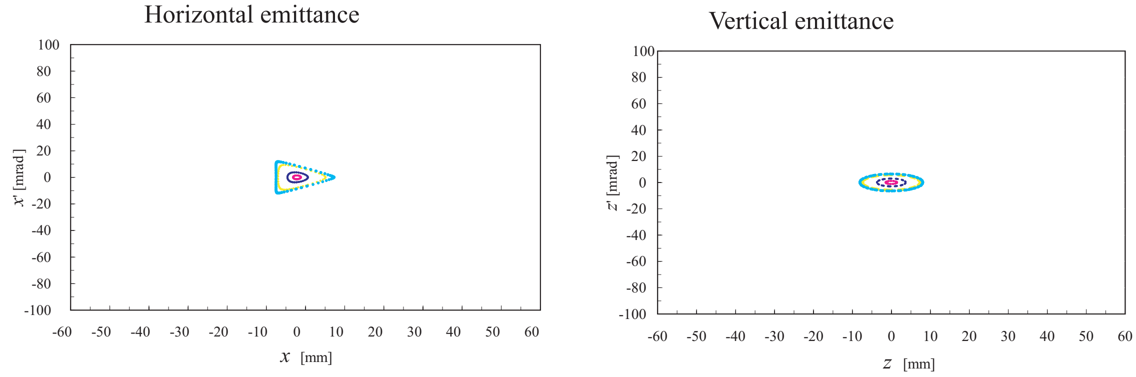

Figure 91: Emittance of the saddle shaped coil

r = 4.9 m

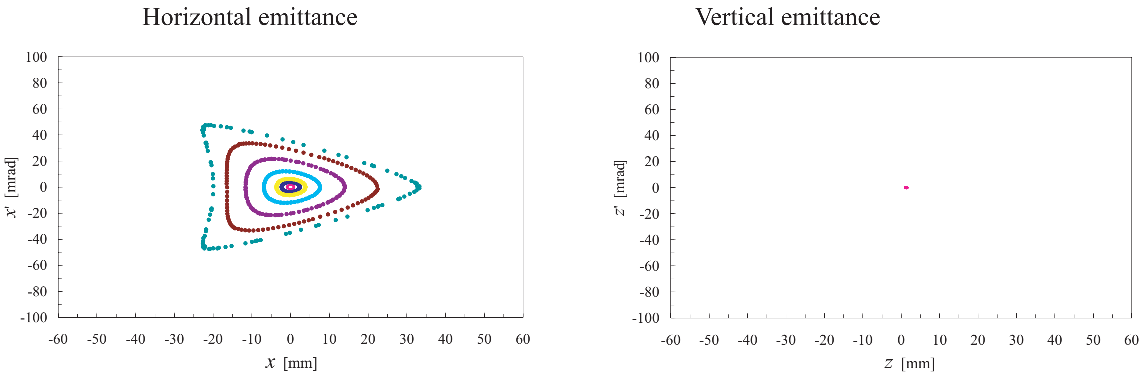

r = 5.1 m

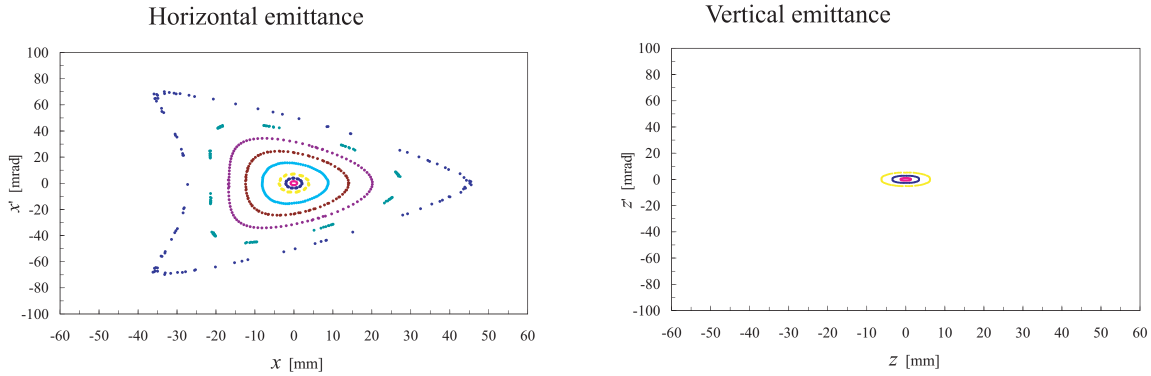

r = 5.3 m

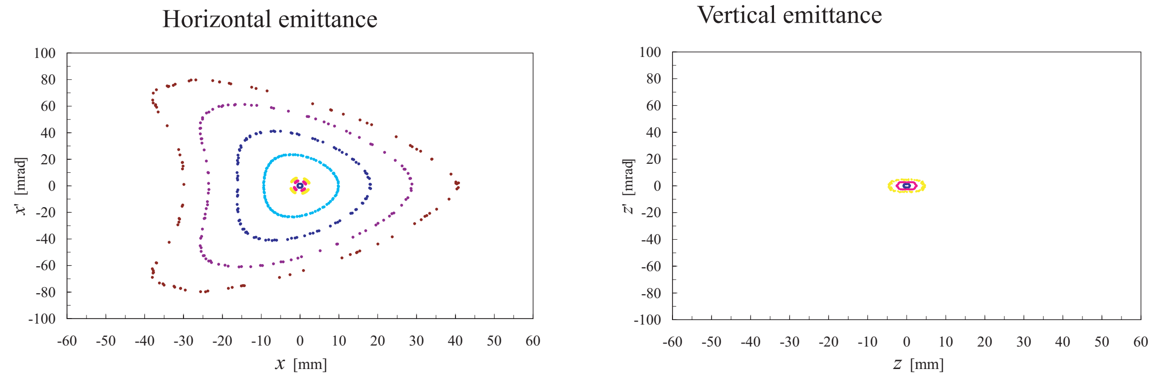

Figure 92: Emittance of the single winding coil

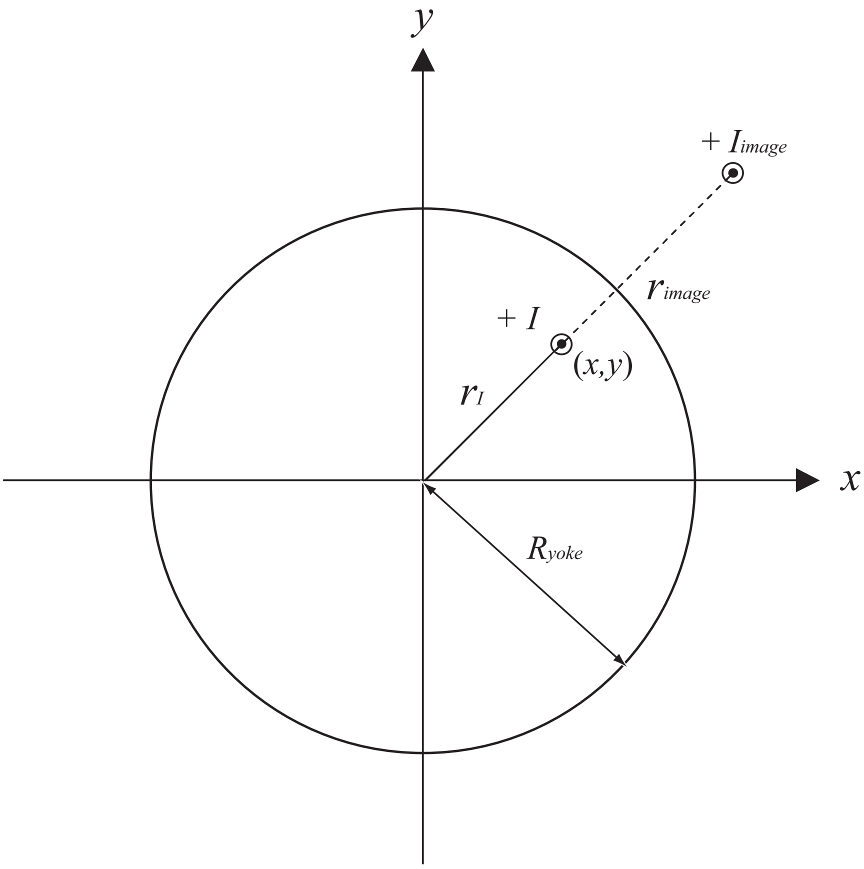

Figure 93: Image of a line current inside an iron yoke

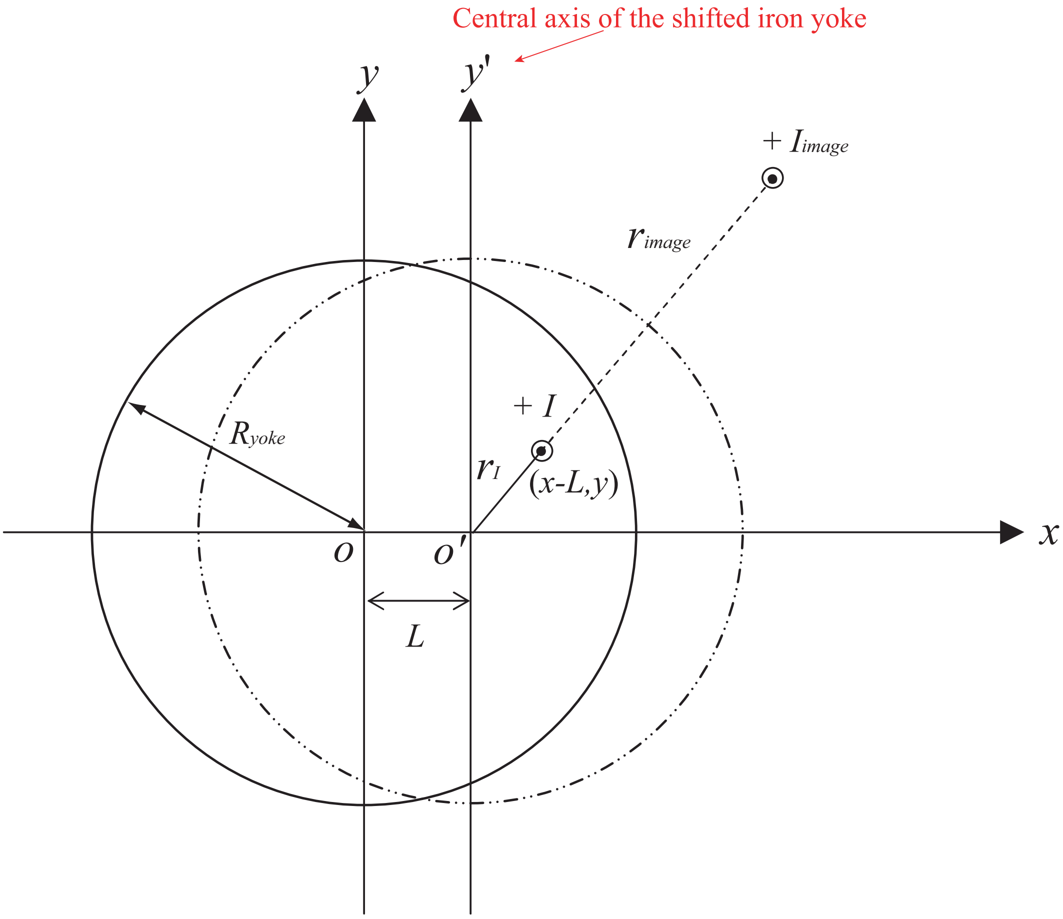

Figure 94: Image of a line current inside an iron yoke, the center of which is shifted.

(I)Basic design of superconducting FFAG magnets with FEM

The design studies of the FFAG superconducting magnet were performed with FEM(TOSCA) as follows.

(a)Effect of the saturation of the iron yoke

Iron has the feature that its permeability saturates in high magnetic field. The design of magnets has to be carried out taking the influence of iron saturation into account. Magnetic field calculations were performed by means of FEM(TOSCA) to verify the extent to which the saturation of the iron yoke affects the magnetic field. The details of the coil and the iron yoke used in the calculation with FEM are listed Table 32 and Table 33, respectively. The 30 coil layers are approximated by 1 layer because of the limitation of TOSCA. Figure 95 illustrates the coil configuration used in the calculation, and the iron yoke which surrounds the coil. The position of the iron yoke is illustrated in Fig. 96. Figure 97 shows B-H curve of the iron. The results of the calculation are shown in Fig. 98. The blue line indicates the $local\, k + 1$ that vertical magnetic field is 1.0 T at the center of the coil. On the other hand, the red line means the $local\, k + 1$ of minute vertical magnetic field which is 1.0×10^{-10} T at the center of the coil. As a result, the saturation of the iron yoke has hardly any influence on the magnetic field when the vertical magnetic field is 1.0 T at the center of the coil, and the yoke is positioned to minimize the magnetic force on the coil.

Table 32: Parameters of the coil in FEM(TOSCA)

Major axis of the coil aperture	0.8 m
Minor axis of the coil aperture	0.6 m
Field index, k	10
Type	Saddle shaped coil
Number of coil layer	1
Number of turn	180
Coil length	1.05 m

Table 33: Parameters of the iron yoke in FEM(TOSCA)

Inside diameter	1.6 m
Outside diameter	2.0 m
Length	1.1 m
Distance shifted from the center axis of the coil	0.155 m

(b)Magnetic shield

Equipment such as RF cavities etc. is placed between magnets. It is therefore necessary to reduce the magnetic field leaking from the magnet as much as possible. The stray magnetic field from the magnet was investigated for two types of iron yoke. The first one is of pure cylindrical form, and the second is a cylinder that has a smaller inner diameter at both ends. Details of the iron yokes are listed in Table 34 and Table 35. Figures 99 and 100 show the schematic view of the position for each iron yoke, respectively. The vertical magnetic field for each position on y-axis along an arc at radius 5.155 m from the accelerator center was calculated using FEM(TOSCA). The coil configuration listed in Table 32 was used with each iron yoke in the calculation. Figure 101 shows the calculated result with the straight cylindrical yoke, and Fig. 102 shows the result with the cylindrical iron yoke with small inner diameter at both ends. It was confirmed that some magnetic field leaks out from the magnet, the maximum being about 0.3 T at the edge of the magnet. There is little difference between the two yoke geometries.

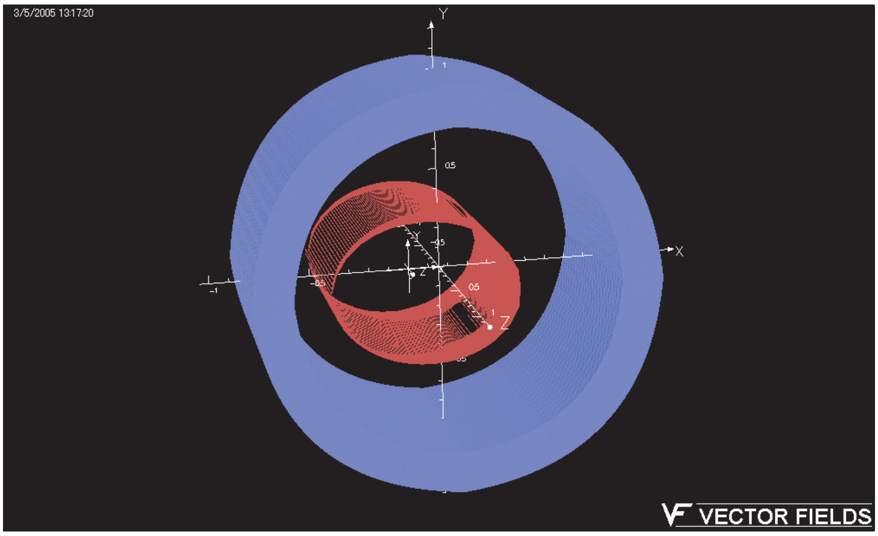

Figure 95: FEM model

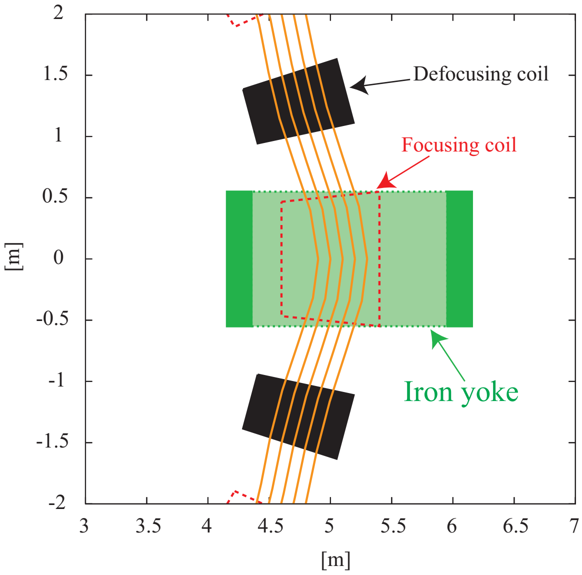

Figure 96: Schematic view of the position of the iron yoke

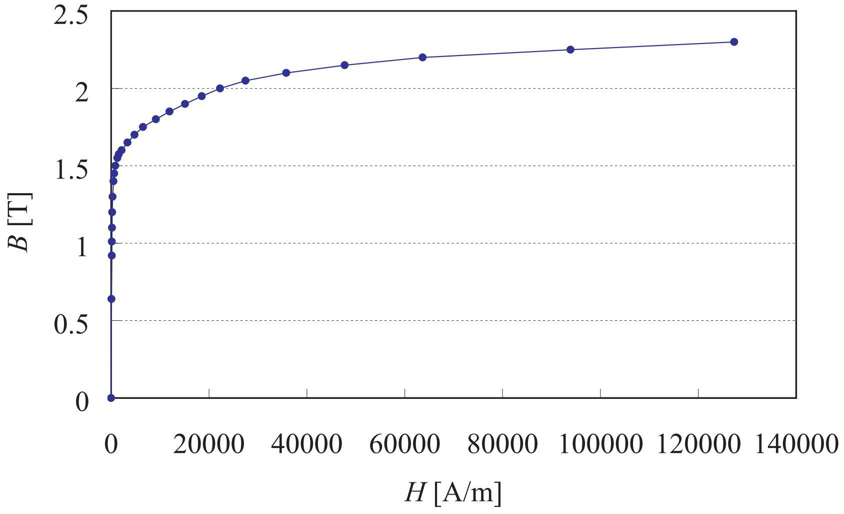

Figure 97: B-H curve of the iron yoke

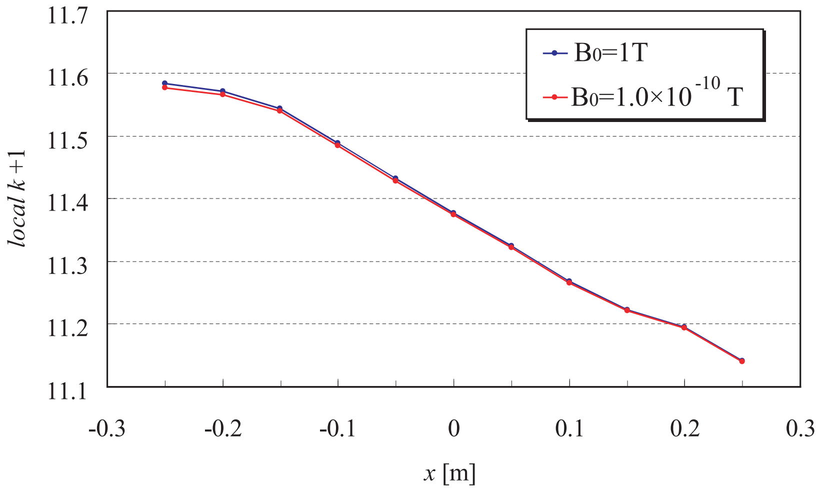

Figure 98: Magnetic fields with the iron yoke

Table 34: Parameters of the cylindrical iron yoke

Inside diameter	1.6 m
Outside diameter	2.0 m
Length	1.2 m
Distance shifted from the center axis of the coil	0.155 m

Table 35: Parameters of the cylindrical iron yoke with small inner diameter at both ends

Inside diameter	1.6 m
Inside diameter at either end of distance 0.05 m	0.9 m
Outside diameter	2.0 m
Length	1.2 m
Distance shifted from the center axis of the coil	0.155 m

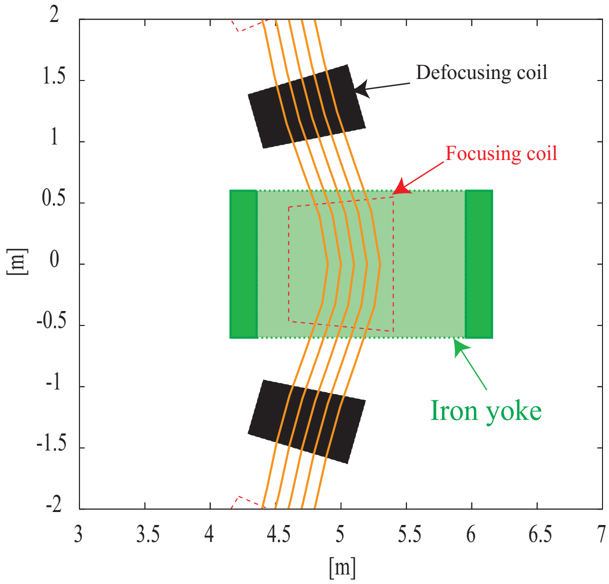

Figure 99: Position of the cylindrical iron yoke

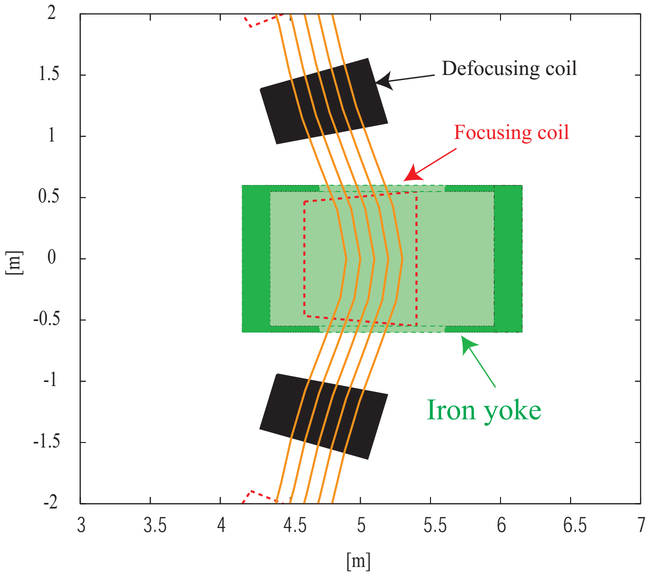

Figure 100: Position of the cylindrical iron yoke with small inner diameter at both ends

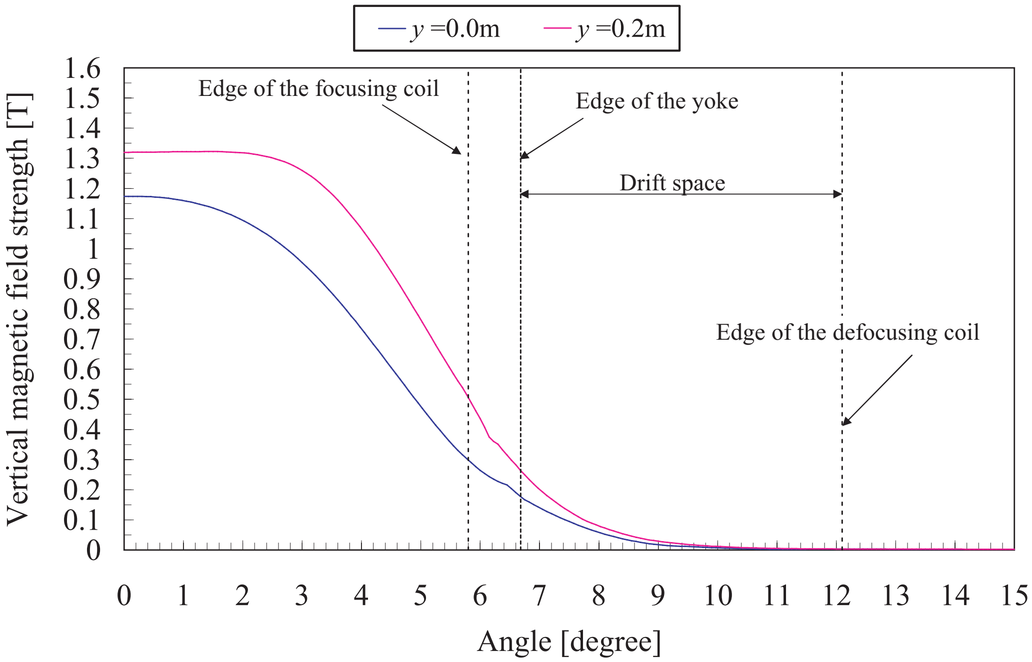

Figure 101: Vertical magnetic field distribution along arc at radius 5.155 m in the case of the straight cylindrical iron yoke

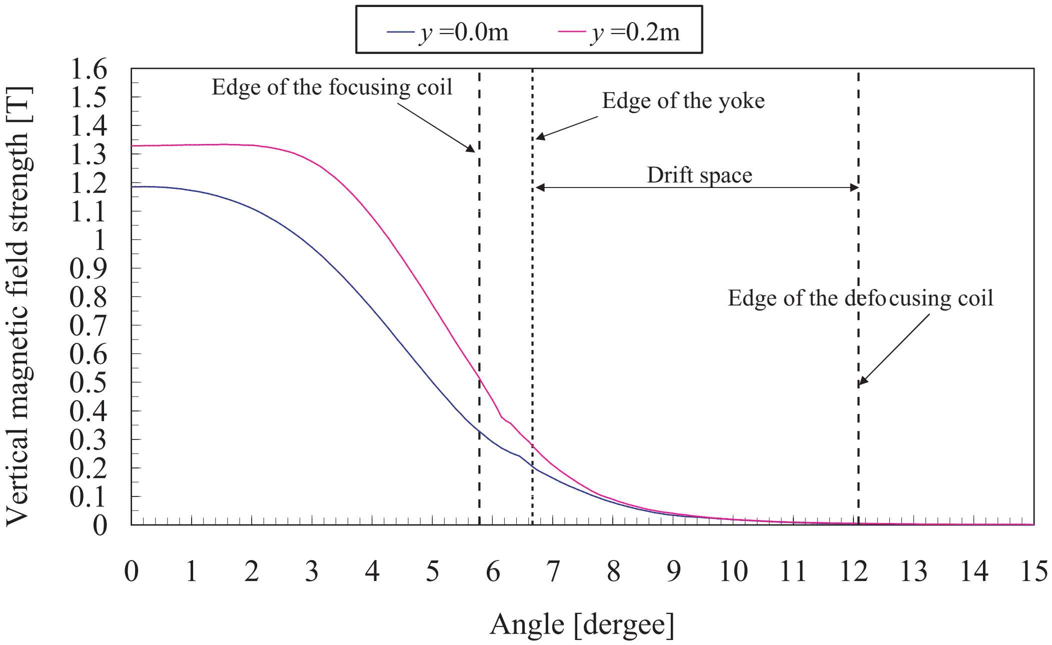

Figure 102: Vertical magnetic field distribution along arc at radius 5.155 m in the case of the cylindrical iron yoke with small inner diameter at both ends

Nomenclature

B	Vertical magnetic field [T]
B_0	Vertical magnetic field at the magnet center [T]
r	Radius from the accelerator center [m]
r_0	Reference radius [m]
k	Geometrical field index
B_n	Normal component of n-th multipole field [T]
μ_0	Permeability of the vacuum [H/m]
I_m	Current on the mid-plane for m-th multipole field [A]
θ_q	Angle at the position q [radian]
a	Radius of a circle [m]
n	Order of the multipole
$\boldsymbol{A}$	Matrix of coefficient for each I_m
$a_{n,m}$	Component of matrix $\boldsymbol{A}$
x	Distance from the magnet center [m]
R_0	Length between the magnet center and the accelerator center [m]
b_n	Normal component of n-th multipole coefficient
θ	Azimuthal angle [radian]
I_0	Current at mid-plane [A]
$local\,k$	Local field index
BL	Integrated magnetic field strength [T $\cdot$ m]

s	Orbit length [m]
$local\,k+1$	Local index of BL
BL_0	BL on the magnet center $[\mathrm{T}\cdot\mathrm{m}]$
c_n	Normal component of n-th multipole coefficient for BL
λ	Effective thermal conductivity of the coil $[\mathrm{W}/(\mathrm{K}\cdot\mathrm{m})]$
λ_{Al}	Thermal conductivity of the pure-Al $[\mathrm{W}/(\mathrm{K}\cdot\mathrm{m})]$
λ_{coil}	Thermal conductivity of the coil $[\mathrm{W}/(\mathrm{K}\cdot\mathrm{m})]$
S_{total}	Cross-section area of the coil in longitudinal direction $[\mathrm{m}^2]$
S_{Al}	Cross-section area of the pure-Al in longitudinal direction $[\mathrm{m}^2]$
S_{coil}	Cross-section area of the coil without the strips in longitudinal direction $[\mathrm{m}^2]$
e	Heat quantity [J]
I	Current [A]
S_{con}	Cross-section area of a conductor $[\mathrm{m}^2]$
δ	Moved distance of a conductor [m]
I_0	Initial current [A]
t_d	Characteristic time for the current decay [s]
T_m	Maximum temperature [K]
T_0	Initial temperature [K]
γ	Density $[\mathrm{kg}/\mathrm{m}^3]$
C	Specific heat $[\mathrm{J}/(\mathrm{g}\cdot\mathrm{K})]$

U	Number of MIITs
V_0	Voltage generated in the magnet [V]
R_{ex}	Resistance of external dump resistor [Ω]
n	Field gradient
ρ	Radius of curvature [m]
B_0	Vertical magnetic field strength at point s [T]
B_z	Vertical magnetic field strength [T]
y	Canonical variable [m]
K	Canonical variable [m^{-2}]
C	Length of the orbit [m]
s	Distance along the orbit from some reference point [m]
R	Equilibrium radius [m]
Θ	Origin of the angular variable [radian]
x	Position in horizontal direction [m]
z	Position in vertical direction [m]
ν_x	Horizontal tune
ν_z	Vertical tune
p	Momentum [$\mathrm{g} \cdot \mathrm{m/s}$]
h	Constant number [radian]
ζ	Spiral angle [radian]

F	Periodic function
$\boldsymbol{B}$	Magnetic field [T]
B_x	x component of $\boldsymbol{B}$ [T]
B_y	y component of $\boldsymbol{B}$ [T]
A_n	Skew component of $2n$-pole component [T]
x	Position in x-axis [m]
y	Position in y-axis [m]
B_{main}	Main magnetic field of the magnet [T]
a_n	Skew component of n-th multipole coefficient
r_x	x component of $\boldsymbol{r}$ [m]
r_y	y component of $\boldsymbol{r}$ [m]
x	x component of $\boldsymbol{z}$ [m]
y	y component of $\boldsymbol{z}$ [m]
$\boldsymbol{r}$	Position of current [m]
$\boldsymbol{z}$	Postion in x-y plane [m]
θ_q	Angle at the position of a line current [radian]
r_{θ_q}	Radius at the position of a line current [m]
I_{image}	Image current [A]
r_{image}	Position of an image line current [m]
r_I	Position of a line current [m]
R_{yoke}	Inner radius of iron yoke [m]

μ	Permeability of an iron [H/m]
L	Shifted distance from the central axis [m]

List of Figures

List of Tables

References

[1] T. Ohkawa, Symposium on Nuclear Physics of the Physics Society of Japan, 1953.

[2] F. T. Cole et al, ”Electron Model Fixed Field Alternating Gradient Accelerator”, Rev. Sci. Instrum., Vol.28, No.6, p403 (1957)

[3] M. Yoshimoto et al, ”The Magnet Design Study for the FFAG Accelerator ”, IEEE Transactions on Applied Superconductivity, No.2, Vol.14, p397-p401 (2004)

[4] M.Aiba et al, ”DEVLOPMENT OF A FFAG PROTON SYNCHROTRON”, Proceeding of European Particle Accelerator Conference, p581 (2000)

[5] M. Aiba, ”Study of Resonance Crossing in Strong Focusing Accelerators”, Ph. D Thesis submitted to Tokyo University (2005)

[6] M. Yoshimoto et al, ”Research and development for 150 MeV FFAG Accelerator ”, Proceeding of The 14th Symposium on Accelerator Science and Technology (2003) (in Japanese)

[7] T. Misu et al, ”Study of Medical FFAG Accelerator ”, Proceeding of The 14th Symposium on Accelerator Science and Technology (2003) (in Japanese)

[8] M. Abdelsalam et al, ”Superconducting Magnet Design for Fixed-Field Alternating-Gradient(FFAG) accelerator”, IEEE Transactions on Magnetics, No.4, Vol.30, p2602-p263 (1994)

[9] T. Obana et al, ”Magnetic Field Design of a Superconducting Magnet for a FFAG Accelerator ”, IEEE Transactions on Applied Superconductivity, No.2, Vol.15, p1185-p1188 (2005)

[10] M. A. Green, ”A Design for a Combined Function Superconducting Dipole for a Muon Collider FFAG accelerator”, Proceeding of Fourth European Conference on Applied Superconductivity (1999)

[11] N. Miyahara et al, ”Superconducting FFAG magnet ”, Proceeding of The 14th Symposium on Accelerator Science and Technology (2003) (in Japanese)

[12] M. Yoshimoto, private communication

[13] T. Ogitsu, private communication

[14] T. Obana et al, "Development of a prototype superconducting magnet for the FFAG accelerator ", IEEE Transactions on Applied Superconductivity (2006) (to be published)

[15] M. Yohismoto, "Study of Beam Dynamics in Fixed Field Alternating Gradient Accelerator", Ph. D Thesis submitted to Doshisya University (in Japanese) (2003)

[16] TOSCA is a trademark of Vector fields Ltd.

[17] ROXIE is described in http://at-mel-em.web.cern.ch/at-mel-em/roxie/documentation/usersdocumentation/firstpage.html

[18] S. Russenschuck, "Numerical Field Calculation and Optimization Methods for the Design of Accelerator Magnets", CERN (2001)

[19] ANSYS is a trademark of Cybernet Systems Co.,Ltd.

[20] Cryogenics Academy, "Handbook of Superconductivity and Cryogenics", Ohm Publishing (in Japanese) (1993)

[21] T. Orikasa, private communication

[22] T. Kumazawa, "Performance Evaluation of Cryostat for Superconducting Magnet in BESS", Master Thesis submitted to Tokyo University of Science (in Japanese) (2005)

[23] M. Aiba, private communication

[24] M. Craddock, "The rebirth of the FFAG," CERN Courier, Vol. 44, No. 6, 2004

[25] C. Johnstone, "Performance criteria and optimization of FFAG lattices," FFAG Workshop, TRIUMF, April 15-21, 2004

[26] K. Takahata, "Superconducting Coils for Fusion", Journal of Plasma and Fusion Research, No.4, Vol.81, p273-p279 (2005)

[27] M. N. Wilson, "Superconducting Magnets", Clarendon Press, Oxford (1983)

[28] F. Sumiyoshi et al, "Multifilament wire and conductor", Sangyou Publishing (in Japanese) (1995)

[29] K. Sugita, "Time-varying Field Quality of Superconducting Accelerator Magnets Induced by Current Redistribution in Cables", Ph. D Thesis submitted to The Graduate University for Advanced Studies (2005)

[30] T. Ogitsu, "Influence of cable eddy currents on the magnetic field of superconducting particle accelerator magnets", Ph. D Thesis submitted to Tsukuba University (1990)

[31] SAD is described in http://acc-physics.kek.jp/SAD/sad.html

[32] K. H. Mess et al, "Superconducting accelerator magnets", World Scientific Publishing Co. Pte. Ltd. (1996)